TAMPEREEN TEKNILLINEN YLIOPISTO
TAMPERE UNIVERSITY OF TECHNOLOGY

OLLI AHLSTEDT

DENSITY FUNCTIONAL STUDY OF HYDROGEN ADSORPTION ON PT-NI NANOCLUSTERS

Master of Science thesis

Examiner: Prof. Jaakko Akola
Examiner and topic approved by the
Faculty Council of the Faculty of
Natural Sciences
on 28th February 2018

ABSTRACT

OLLI AHLSTEDT: Density functional study of hydrogen adsorption on Pt-Ni nanoclusters
Tampere University of Technology
Master of Science thesis, 118 pages, 5 Appendix pages
April 2018
Master's Degree Programme in Science and Engineering
Major: Advanced Engineering Physics
Examiner: Prof. Jaakko Akola
Keywords: electrocatalysis, hydrogen evolution reaction, bimetallic nanoclusters, density functional theory

The development of affordable and earth-abundant electrocatalysts for the hydrogen evolution reaction (HER) has attracted great attention in recent years. The effective production of molecular hydrogen is of crucial importance, because it could provide a practical solution to the energy storage problem of renewable energy. The platinum group metals (PGMs) are the best HER catalysts, but their large-scale applicability is limited by their high cost, scarcity, and high supply risk. Therefore, finding alternative HER catalysts or reducing the amount of PGMs in catalysts is essential.

In the present work, density functional theory calculations were performed on small 55-atom Pt-Ni nanoclusters to study their activity towards HER. Two Pt_nNi_{55-n} compositions, $Pt_{12}Ni_{43}$ and $Pt_{20}Ni_{35}$, were studied in the gas phase and on a γ-Al_2O_3 support. The critical hydrogen coverages were determined using the method based on the differential free energy of hydrogen adsorption. The free energy of hydrogen adsorption, ΔG_{H^*}, was used as a descriptor of the HER activity. This descriptor has been successful in predicting the HER activity of various non-noble materials, such as molybdenum disulfide (MoS_2) edges and transition metal phosphides.

The $Pt_{12}Ni_{43}$ and $Pt_{20}Ni_{35}$ clusters are icosahedral in the gas phase and they were observed to retain their shape when adsorbed on the alumina support. The calculated excess energies indicate that the formation of the bimetallic clusters is energetically favorable. Bader charge analysis revealed that the support donates electron density to the clusters. Ni_3 hollow sites were discovered to be strongly binding sites for hydrogen. The clusters adsorb approximately four H atoms per facet before the adsorption becomes endergonic, therefore the critical hydrogen coverages on the clusters are high. The obtained ΔG_{H^*} values are smaller than 0.1 eV in the gas phase and on the support, suggesting that the clusters are catalytically active towards HER.

TIIVISTELMÄ

OLLI AHLSTEDT: Elektronirakenteen tiheysfunktionaaliteoriaan perustuvat simulaatiot vedyn adsorptiolle Pt-Ni nanoklustereiden pinnoilla
Tampereen teknillinen yliopisto
Diplomityö, 118 sivua, 5 liitesivua
Huhtikuu 2018
Teknis-luonnontieteellinen koulutusohjelma
Pääaine: Teknillinen fysiikka
Tarkastaja: Prof. Jaakko Akola
Avainsanat: sähkökatalyysi, vedyn evoluutioreaktio, bimetalliset nanoklusterit, tiheysfunktionaaliteoria

Edullisten ja maankuoressa yleisten katalyyttimateriaalien kehittäminen vedyn evoluutioreaktioon (HER) on saanut viime vuosina paljon huomiota. Molekulaarisen vedyn tuottaminen tehokkaasti on erittäin tärkeää, koska se tarjoaisi käytännön ratkaisun uusiutuvan energian varastointiin. Platinaryhmän metallit ovat parhaita HER-katalyyttejä, mutta niiden laajamittaista käyttöä rajoittavat korkea hinta, rajalliset varannot ja tuottavien maiden epävakaus. Täten on tärkeää etsiä vaihtoehtoisia katalyyttimateriaaleja ja vähentää platinaryhmän metallien käyttöä HER-katalyyteissä.

Tässä työssä mallinnettiin pieniä 55-atomisia platinasta ja nikkelistä koostuvia nanoklustereita tiheysfunktionaaliteorian avulla. Kahden Pt_nNi_{55-n} seoksen, $Pt_{12}Ni_{43}$ ja $Pt_{20}Ni_{35}$, aktiivisuutta HER-katalyytteinä tutkittiin vapaina ja γ-Al_2O_3 pinnalla. Kriittiset vetypeitot määritettiin menetelmällä, joka perustuu vedyn adsorption differentiaaliseen Gibbsin vapaaenergiaan. Vedyn adsorption vapaaenergiaa, ΔG_{H^*}, käytettiin HER-aktiivisuuden deskriptorina. Useiden epäjalojen HER-katalyyttien, kuten molybdeenidisulfidin (MoS_2) reunojen ja siirtymämetallifosfidien, aktiivisuus on aiemmin ennustettu ΔG_{H^*}-deskriptorin avulla.

Vapaat $Pt_{12}Ni_{43}$ and $Pt_{20}Ni_{35}$ klusterit ovat ikosaedrin muotoisia ja ne säilyttävät muotonsa pinnalle adsorboituneina. Bader-varausanalyysin mukaan sähkövarausta siirtyy pinnalta klustereihin. Kolmen nikkeliatomin muodostamat aukot klustereiden pinnalla sitovat vetyä voimakkaasti. Klustereiden jokaiselle tahkolle adsorboituu noin neljä vetyatomia ennen kuin adsorptio muuttuu endotermiseksi, joten kriittiset vetypeitot ovat suuria. Lasketut ΔG_{H^*}-deskriptorin arvot ovat pienempiä kuin 0,1 eV sekä vapaille että pinnalle adsorboituneille klustereille. Tämän perusteella tutkitut klusterit ovat aktiivisia HER-katalyyttejä.

PREFACE

This Master of Science thesis was carried out at the Materials and Molecular Modeling (M&MM) research group at Tampere University of Technology during autumn 2017 and spring 2018. The research was done for the CritCat project (2016–2019), which is a part of European Union's Horizon 2020 research and innovation programme. The computational resources were provided by Finnish IT Center for Science (CSC).

I thank my supervisor and examiner Prof. Jaakko Akola for this great opportunity to work on this interesting and important topic. I am grateful for being employed as a long-term member of the M&MM group. Working alongside my studies has provided me plenty of insight into scientific research and computing. Sincere thanks to my past and present colleagues at TUT and the collaborators at Aalto University. Thank you for all the help, guidance, and interesting discussions.

To all of my friends, thank you for the all the time we have spent together practising different sports, hobbies, or simply hanging out. I had the best time with you. Finally, I would like to acknowledge special thanks to my family members. Thank you for all the support and encouragement, without you this would have been impossible. Thanks for pushing me forward to face new challenges.

Tampere, April 2018

Olli Ahlstedt

CONTENTS

LIST OF FIGURES

LIST OF TABLES

LIST OF ABBREVIATIONS AND SYMBOLS

Abbreviations:

BEP	Brønsted–Evans–Polanyi relation
BFGS	Broyden–Fletcher–Goldfarb–Shanno algorithm
CDD	Charge density difference
CNT	Carbon nanotube
CPU	Central processing unit
CP2K	Quantum chemistry and solid state physics software package
CSC	IT Center for Science (*Tieteen tietotekniikan keskus* in Finnish)
CV	Cyclic voltammetry
DFT	Density functional theory
DRC	Disordered reduced-core structure
DZVP	Double-ζ valence plus polarization basis set
ECSA	Electrochemically active surface area
FFT	Fast Fourier Transform
GGA	Generalized gradient approximation
GPW	Gaussian and plane waves method
GTH	Goedecker–Teter–Hutter type pseudopotential
GTO	Gaussian-type orbital
HER	Hydrogen evolution reaction
HF	Hartree–Fock
HOMO	The highest occupied molecular orbital
ICO	Icosahedron structure
KS	Kohn–Sham
LDA	Local density approximation
LSDA	Local spin density approximation
LSV	Linear sweep voltammetry
M&MM	Materials and Molecular Modeling research group
NEB	Nudged elastic band method
NHE	Normal hydrogen electrode
NP	Nanoparticle
OER	Oxygen evolution reaction
ORR	Oxygen reduction reaction
OT	Orbital transformation method
PBE	Perdew–Burke–Ernzerhof functional
PDOS	Projected density of states
PEC	Photoelectrochemical cell

PES	Potential energy surface
PGM	Platinum group metal
RDF	Radial distribution function
RGO	Reduced graphene oxide
RHE	Reversible hydrogen electrode
SE	Schrödinger equation
SHE	Standard hydrogen electrode
TM	Transition metal
TMD	Transition metal dichalcogenide
TMP	Transition metal phosphide
TOF	Turnover frequency (turnover rate)
TPES	Total primary energy supply
TST	Transition state theory
TUT	Tampere University of Technology
UHV	Ultra-high vacuum
VH	Volmer–Heyrovsky mechanism
VT	Volmer–Tafel mechanism
XRD	X-ray diffraction
ZPE	Zero point energy

Physical constants:

a_0	Bohr radius, $a_0 = \frac{4\pi\varepsilon_0\hbar^2}{m_e e^2}$
e, q_e	Elementary charge
F	Faraday constant
$\hbar$	Planck constant
k_B	Boltzmann constant
m_e	Electron rest mass
N_A	Avogadro's number
R	Universal gas constant
ε_0	Vacuum permittivity
μ_B	Bohr magneton, $\mu_B = \frac{e\hbar}{2m_e}$

Electrocatalysis:

a	Empirical constant in Tafel equation
A	Area (*e.g.* the cross sectional area of an electrode)
b	Empirical constant in Tafel equation (the Tafel slope)
C_O	Concentration of the oxidant
C_R	Concentration of the reductant
C_O^*	Bulk concentration of the oxidant

C_{R}^{*}	Bulk concentration of the reductant
E	Applied potential
E_{a}	Activation energy
E_{eq}	Equilibrium potential of an electrochemical cell
$E^{0'}$	Formal potential of an electrode couple
f	$F/(RT)$
G	Gibbs free energy
i	Electric current
i_{a}	Anodic current component
i_{c}	Cathodic current component
i_0	Exchange current
j	Current density
j_0	Exchange current density, i_0/A
k	Reaction rate constant
k_{b}	Backward reaction rate constant
k_{f}	Forward reaction rate constant
k_0	Standard rate constant
K	Prefactor in Arrhenius equation
n	Stoichiometric number of electrons involved in an electrochemical reaction
n_{H}	Number of adsorbed hydrogen intermediates
n_{site}	Number of active adsorption sites available on the studied catalyst surface
O	Oxidized form of a system (the oxidant)
R	Reduced form of a system (the reductant)
S	Number of active sites on the electrode surface
S, S′	An adsorption site on the surface of a catalyst
$S^{\circ}(\mathrm{H_2})$	Gas phase entropy of H_2 at the standard conditions
t	Time
T	Absolute temperature
TOF	Turnover frequency
$\mathrm{TOF}_{\mathrm{avg}}$	Turnover frequency averaged across all surface sites
U	Applied potential (the cathodic potential)
v	Reaction rate
v_{b}	Rate of a backward reaction
v_{f}	Rate of a forward reaction
x	Distance to a reference point (*e.g.* electrode surface)
α	Charge transfer coefficient
ΔE_{H}	The hydrogen chemisorption energy

ΔE_{ZPE}	The difference in the zero point energy between the adsorbed and the gas phase
$\Delta E_{\mathrm{reaction}}$	Reaction energy (the difference between the initial and final state of a reaction)
ΔG	The reaction energy (free energy difference between reactants and producs, thermodynamic barrier)
$\Delta G_{\mathrm{a}}^{\ddagger}$	Standard free energy of activation at anode (non-equilibrium)
$\Delta G_{\mathrm{c}}^{\ddagger}$	Standard free energy of activation at cathode (non-equilibrium)
$\Delta G_{0,\mathrm{a}}^{\ddagger}$	Standard free energy of activation at anode (in equilibrium)
$\Delta G_{0,\mathrm{c}}^{\ddagger}$	Standard free energy of activation at cathode (in equilibrium)
ΔG_{H^*}	The Gibbs free energy of hydrogen adsorption
ΔG_{diff}	The differential free energy of hydrogen adsorption
ΔG_{tot}	The total free energy of adsorption (the integral adsorption energy)
$\Delta G^{\ddagger}$	Standard free energy of activation
ΔS_{H}	The entropy of adsorption
ε_d	the d-band center
ε_{F}	The Fermi energy
η	Overpotential
θ_{H}	The hydrogen coverage
μ	The chemical potential
*	Intermediate state, an adsorption site on the surface of a catalyst
ln	Natural logarithm, base e (Euler's number)
$\log_{10}$	Common logarithm, base 10

Quantum mechanics:

$d_{i\mu}$	Coefficients corresponding to $g_i(\boldsymbol{r})$ (GTO basis set)
E_n	Electronic eigenvalues (electronic total energies)
E_n	Electron density functional, $E_n = E_n[\rho(\boldsymbol{r})]$ (DFT)
E_0	Energy corresponding to the electronic ground-state Φ_0
E_{xc}	Exchange-correlation energy
$E_{\mathrm{xc}}^{\mathrm{GGA}}$	GGA form of exchange-correlation functional
$E_{\mathrm{xc}}^{\mathrm{LDA}}$	LDA form of exchange-correlation functional
$\mathcal{E}_n$	Electron-nuclear eigenvalues (total energies)
$\boldsymbol{F}_I$	Force acting on a nucleus I
$\boldsymbol{G}$	Reciprocal lattice vectors
$g_i(\boldsymbol{r})$	Primitive Gaussian functions (GTO basis set)
$\hat{\mathcal{H}}$	Electron-nuclear Hamiltonian operator
$\hat{h}_{\mathrm{e}}$	Electronic Hamiltonian operator
i	Imaginary unit

M	Mass (nuclei)
n	State of a system
N	Number of electrons
N_s	Number of double occupied single-electron orbitals
P	Number of nuclei
$\boldsymbol{P}$	Momentum operator
$P_{\mu v}$	Element of a density matrix (GTO basis set)
$\boldsymbol{r}$	Spatial coordinates (electrons)
$\boldsymbol{R}$	Spatial coordinates (nuclei)
$\boldsymbol{R}$	Position operator
$\boldsymbol{R}_\mathrm{cl}$	Cartesian coordinates of classically treated nuclei
$\hat{T}_\mathrm{e}$	Kinetic energy operator (electrons)
$\hat{T}_\mathrm{n}$	Kinetic energy operator (nuclei)
T_0	Kinetic energy of non-interacting electrons
$\hat{U}_\mathrm{ee}$	Electron-electron interaction operator
v_ext	External potential acting on electrons
V_ext	External potential energy
V_H	Hartree potential (Classical Coulomb potential, electrons interacting with electron density)
$\hat{V}_\mathrm{ne}$	Electron-nucleus interaction
$\hat{V}_\mathrm{nn}$	Nucleus-nucleus interaction operator
v_xc	Exchange-correlation potential
Z	Atomic number
ε	Single-electron eigenvalue
$\epsilon_\mathrm{xc}^\mathrm{LDA}$	Average exchange-correlation energy per particle in homogeneous electron gas
Θ_n, Θ_m	Nuclear sub-system eigenstates (time-dependent wave functions)
ρ	Electron density
$\tilde{\rho}$	Electron density in the plane wave basis set
ρ_0	Ground-state of electron density
$\rho_\uparrow$	Density representing spin up states
$\rho_\downarrow$	Density representing spin down states
ϕ	Single-electron wave function (Kohn–Sham orbital)
φ	Orbital (GTO basis set)
Φ_n, Φ_q	Adiabatic eigenstates (electron sub-system wave functions, time-independent)
Φ_0	Electronic ground-state (many-electron wave function)
Ψ	Time-dependent wave function (electron-nuclear)
ψ_n	Electron-nuclear eigenstates (time-independent wave functions)

Ω	The volume of the unit cell (plane wave basis set)
∇	Gradient operator
∇^2	Laplacian operator
$\left[\hat{A},\hat{B}\right]$	Commutator of operators $\hat{A}$ and $\hat{B}$: $[\hat{A}\hat{B} - \hat{B}\hat{A}]\psi = 0$, where ψ is any wave function
$\langle x \rangle$	Expectation value of variable x

Analysis methods and results:

CT	Charge transfer
E_{ads}	Adsorption energy
E_{exc}	Excess energy
g_{AB}	Radial distribution function for atoms A and B
n	Number of Pt atoms (Pt-Ni clusters)
N_{A}	Number of A atoms in a system
N_{B}	Number of B atoms in a system
$N_A(r_i)$	Number of A atoms at a distance r from B atoms
N_r	Number of bins (spherical shells)
Q_{cluster}	Charge of a cluster in the gas phase
$Q_{\text{cluster/support}}$	Charge of an adsorbed cluster
r	Radial distance (in the context of RDF)
$R_{\text{A-B}}$	Bond length between atoms A and B
r_{ave}	Average bond length between atoms
r_{max}	Bin cutoff radius
$S(\boldsymbol{Q})$	Structure factor
V	Volume of a system
$V_\delta(r_i)$	Volume of a bin i
$\delta_{i,j}$	Kronecker delta, equals 1 if i and j are equal, and 0 otherwise
ΔE	Energy difference to the ground-state configuration of a system
Δr	Bin thickness
μ_{T}	Total magnetic moment per atom
ρ_A	Average density of A atoms in a system
$\rho_{AB}(r)$	Density of A atoms at a distance r to B atoms
σ^2	Variance (Gaussian distribution)

1. INTRODUCTION

Finding methods to produce energy sustainably in global scale is challenging and essential. The global population, currently around 7.5 billion, is expected to rise above 9.7 billion in 2050 and above 11 billion in 2100 [1]. Increasing population and rising living standards together result in growing energy consumption. Although renewable energy technologies such as wind and solar have seen a boom during the last few years, around 80 % of the world's energy is still produced by burning fossil resources (oil, gas, and coal). The world's total primary energy supply from 1970 to 2015 by different fuel sources [2] is represented in Figure 1.1. Fossil fuels store energy in a very concentrated form, making them widely used and applicable in different sectors such as electricity production, transportation, and production of industrial chemicals. In order to reduce global pollution levels, material and energy consumption, and to meet the energy demands of growing population and living standards, the world's energy has to be produced in more environment friendly and sustainable ways. Alternative solutions to fossil fuels must be found also due to their limited supply. [3]

In 2010 the electricity sector accounted for approximately 12 % of global energy demand [3]. Notable, less polluting alternative energy sources for electricity production are nuclear power and renewable sources such as hydroelectric, wind, and solar power. As nuclear power also has a limited supply similar to fossil fuels, renewable energy sources would be an attractive choice. However, renewable energy production varies depending on conditions and time of the day, which may result in a shortage or oversupply of energy. This is illustrated in Figure 1.2, which presents the electricity consumption and the production of wind and solar energy in Denmark. Obviously if the main source of energy ought to be renewable, a large-scale energy storage solution is needed to smooth the difference between energy supply and demand. [4]

An attractive solution to the energy storage problem would be to use renewable energy to produce molecular hydrogen by splitting water electrochemically [5]. Hydrogen could be stored and on demand converted into electricity using fuel cells. This is an attractive solution especially since fuel cells produce negligible emissions [6].

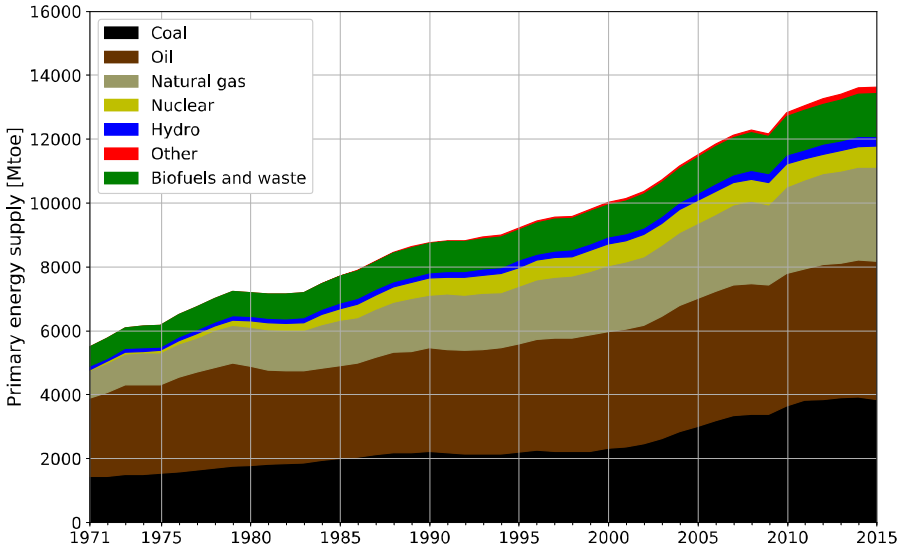

Figure 1.1 *The world's total primary energy supply (TPES) from 1970 to 2015 by different fuel sources [2]. A tonne of oil equivalent (toe) is the amount of energy released by burning one tonne of crude oil (approximately 42 GJ or 11.630 kWh). TPES of the world has over doubled in 45 years, from 6101 Mtoe in 1973 to 13647 Mtoe in 2015. Solar, wind, geothermal and tide/wave/ocean are included in Other, which comprises 1.5 % of the TPES in 2015.*

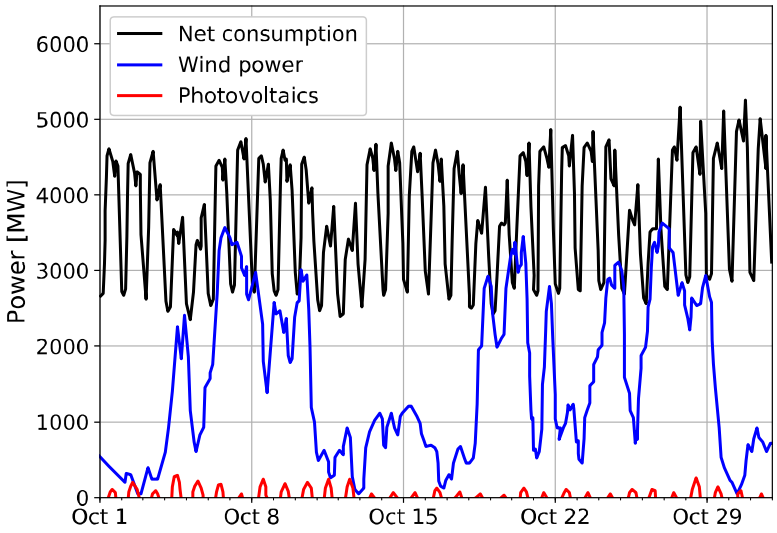

Figure 1.2 *Danish electricity grid data for October 2014, adapted from [4]. The net consumption (black) fluctuates in cyclic manner, and so does the electricity production from photovoltaics (red). The peaks in solar power production match the peaks in consumption fairly well. The net electricity consumption is lower during weekends. The need for storage arises especially from rather randomly fluctuating winder power (blue).*

In addition, molecular hydrogen can also be used as a fuel in transportation, which accounts for approximately a quarter of humanity's energy consumption [6]. At the moment oil is the most widely used energy source (93 %) in the transportation sector [2, 4].

Water-splitting process can be performed in various devices such as *electrolyzers* and *photoelectrochemical cells* (PECs). Electrolyzers require an external source of electricity to drive the water-splitting process [7], whereas PECs utilize a semiconductor electrode where excited electrons and holes are produced by sunlight hitting the electrode [5]. In a water-splitting cell, the hydrogen evolution reaction (HER) occurs at the cathode, and the oxygen evolution reaction (OER) occurs at the anode [5, 7]. Suitable catalyst materials are required on the electrodes to lower the activation energy of both half-reactions. The field of *electrocatalysis* studies how catalysts affect reaction kinetics and energy barriers in electrochemical interfaces [8]. Besides its practical use in water-splitting, HER has for decades served as a model reaction for studying the nature of different electrode materials [8]. The rate of HER affects greatly the performance of a water-splitting device [9]. Therefore, in order to be able to utilize electrocatalytic water-splitting in large scale, finding earth-abundant and affordable catalysts with required properties is crucial.

Platinum (Pt) is widely known as the best-performing catalyst for hydrogen evolution [3]. It is not an optimal catalyst material due to its high supply risk; it is a rare and expensive metal, it has a low recycling rate, and it is produced in politically and economically unstable countries such as South Africa and Russia, which comprise approximately 70 % and 16 % of the global platinum production in 2014, respectively [10]. Materials with high supply risk coupled with high economic importance are called critical raw materials. Platinum and other platinum group metals (PGMs) are considered as critical raw materials by the European Union [11]. Therefore, finding alternative catalysts or reducing the amount of platinum is of great importance.

One way to reduce the amount of platinum in catalysts is to replace it with metal alloys. If the amount of platinum in catalysts is done by replacing Pt with cheaper metals, such as transition metals (TMs), the material costs decrease. Some Pt-TM alloys, such as Pt-Ni alloy, have also been observed to show increased catalytic activity in oxygen reduction reactions[1] (ORRs) compared to pure platinum [13, 14]. The unique electronic properties of transition metals are due to their unfilled d-orbitals. This allows the electronic structure of a TM surface to be modified, which affects the adsorption energy of reactants [15, 16]. Recent advances in nanoscience

[1] Oxygen reduction reactions play a crucial role in fuel cell development [12].

and nanotechnology have made it possible to study and tune the electronic structure of different nanoscale systems such as nanoclusters and nanoparticles [17].

Out of different Pt-TM alloy systems, bimetallic Pt-TM nanoclusters are of special interest [12]. Nanosystems, especially nanoclusters, are promising in catalysis perspective, because they have a large surface-to-volume ratio, which results in an increased number of catalytically active sites and reduces material costs [17]. In recent years, Pt-TM catalysts like Pt-Fe, Pt-Co, Pt-Ni, and Pt-Cu have been studied, primarily for oxygen reduction reactions [12]. It is of general interest if these systems could be used as catalysts in reactions such as hydrogen evolution.

In this thesis, catalytic properties of bimetallic platinum-nickel (Pt-Ni) nanoclusters are investigated for the hydrogen evolution reaction. The reaction is assumed to occur in an acidic environment. Two platinum-poor 55-atom nanoclusters, namely $Pt_{12}Ni_{43}$ and $Pt_{20}Ni_{35}$, are studied. Clusters are simulated computationally using the density functional theory (DFT) and their catalytic properties for HER are evaluated in the gas phase and on alumina Al_2O_3 support using the Gibbs free energy of hydrogen adsorption as a descriptor. DFT calculations are performed using the CP2K software package [18]. In addition to studying the two clusters, $Pt_{12}Ni_{43}$ and $Pt_{20}Ni_{35}$, the aim is to find a general routine to study catalytic properties of small Pt-TM nanoclusters. If catalytic properties of the aforementioned Pt-Ni clusters are promising, this work would guide experimental groups to test these systems.

Chapter 2 is a brief introduction to catalysis, heterogeneous catalysis and electrode kinetics. Various equations governing the electrode kinetics are derived to understand experimentally measured activities of HER catalysts. Chapter 3 introduces the different reaction mechanisms of the hydrogen evolution reaction. Characteristics of a good HER catalyst are briefly described and recent developments in HER catalysts are presented. First-principles modeling of HER catalyst is discussed in Chapter 4, which includes important concepts such as Brønsted–Evans–Polanyi (BEP) relations, the *d*-band model, and active site models. The required thermochemical equations for determining the Gibbs free energy of hydrogen adsorption are presented. Electronic structure calculations, the density functional theory, and various analysis methods that were applied in the present work are explained in Chapter 5. The results of the computational study are presented in Chapters 6 and 7, while the conclusions are drawn in Chapter 8.

2. FUNDAMENTALS OF ELECTROCATALYSIS

This chapter is a brief introduction to the theory of heterogeneous catalysis and electrochemistry, especially electrode kinetics. The reactions in electrochemical water-splitting devices occur at electrode surfaces. Therefore, a short theoretical inspection of the kinetics is done for a single-electron transfer reaction. The hydrogen evolution reaction is a two-electron transfer process, but the equations derived in this chapter are relevant in the context of HER as well. It is common in the field of electrocatalysis to present experimental results in form of *Tafel plots* and *polarization curves*. These concepts will be seen to arise from the theory in this chapter, providing a theoretical connection between catalytic reactions on electrode surfaces and experimental observations. [19, 20]

Electrode reactions are heterogeneous reactions [19], therefore the chapter starts off with a short introduction to heterogeneous catalysis and catalysis in general, most importantly to the *Arrhenius equation*. This is then followed by an introduction to electrochemistry. The *Butler–Volmer model* will be applied to derive the equations governing electrode kinetics: *current–overpotential equation* and *Butler–Volmer equation*. Important concepts such as *overpotential* and *exchange current density* will be presented. A more profound introduction to heterogeneous catalysis can be found for example in [21] and introduction to electrocatalysis and electrode kinetics in [19].

2.1 Introduction to Catalysis

In catalysis, the rate of a chemical reaction is increased due to an additional substance, called a catalyst, participating the reaction. This was recognized as a phenomenon in chemistry in the beginning of 19th century. Practical catalysis research became popular in the 20th century, notably in the 1910s after the German chemists Fritz Haber and Carl Bosch found a suitable iron-based catalyst for ammonia synthesis in 1909, making the industrial level production of ammonia possible. During the 20th century the empirical basis of catalysis was well founded and nowadays the practical aspects of catalysis are well understood. However, practical catalysis

has always been better understood than the theory of catalysis, *i.e.*, understanding of the underlying molecular level mechanisms. Nowadays, modern computational chemistry is expanding catalyst material design and the understanding of catalysis rapidly. [21]

During the last century, catalysis has become an essential technology in the chemical industry. It is a multibillion-dollar business, which influences our everyday life [22]. Catalysis is used in many applications world-wide such as in oil refineries, productions of chemicals, materials and fertilizers, and reducing pollution caused by traffic and industry. The production of most industrially important chemicals involves catalysis and over 85 % of the products of chemical industry are made in catalytic processes. Catalysts are in a crucial role in fuel cells and energy conversion technologies [3]. Catalysis also exists in the nature. Chemical reactions that are essential for life, *e.g.* photosynthesis, are dependent on biological catalysts called enzymes. [21]

Several fairly recent scientific and technological developments are currently changing the field of catalyst design and material screening. Firstly, advances in nanoscience and nanotechnology have made it possible to study and tune the electronic structure of nanoscale system such as nanoparticles (NPs) [17]. Nanosystems are very important in catalysis perspective due to their large surface-to-volume ratio and possibility to tune their electronic properties. Secondly, over the past decade quantum chemistry and the density functional theory (DFT) have made it possible to study electrocatalysis computationally. This has increased the understanding of the molecular level mechanisms in catalytic reactions, because properties that are difficult to measure experimentally can be calculated using computer simulations. Computational (high-throughput) catalyst material screening has became possible to support the experimental catalyst development. [3, 23]

The use of catalysts provides many advantages over non-catalytic, stoichiometric chemical reactions. Catalytic reactions are energetically more favorable than their non-catalytic counterparts, thus they have higher reaction rates due to the lower activation energy barriers. Because the reaction rates are accelerated the reactions can be carried under lower, practically attainable temperatures and pressures. This generally reduces costs in the chemical industry and enables safer working conditions. Catalysts also usually allow avoiding toxic and hazardous reagents and solvents, and their use can help to minimize the formation of waste and undesirable byproducts, increasing the efficiency of raw material consumption. Without catalysts many reactions would not be economical due to aforementioned reasons. Some reactions would not be even possible because there are thermodynamic limitations to the

conditions under which products can be formed. [21]

Catalysts can be atoms, molecules, enzymes (biocatalysts) and solid surfaces. Catalysis is usually categorized as heterogeneous and homogeneous catalysis. In heterogeneous catalysis, the reactant species and the catalyst are in different phases. Typically the catalyst is a surface of a solid catalyst, and the reactant species are in liquid or gas phase. In homogeneous catalysis, the reactant species and the catalyst are in the same phase, usually liquid or gas. Similar categorization applies to catalysts as well; there are heterogeneous and homogeneous catalysts. Heterogeneous catalysts are more common the industrial applications due to their practicality. They are easier to recycle than homogeneous catalysts, because they do not mix with the reactant species. [21]

2.2 Heterogeneous Catalysis

Catalytic reaction is a cyclic process, where the catalyst offers an alternative path for the reaction to proceed. The catalytic path is generally more complex, but energetically more favorable due to its lower activation energy. This is illustrated in Figure 2.1, which represents a potential energy diagram of the catalytic and non-catalytic paths of a simple chemical reaction. The potential is generally presented against *reaction coordinates*, which represent the progress along the reaction pathway. [19, 21, 22]

First, in the presence of a suitable catalyst, the reactant molecules bind to the catalyst surface. These binding sites, where the catalytic cycle takes place, are called *catalytic centers* or *active centers*. The binding step has to be exothermic *i.e.* free energy has to decrease. Next, the reactant molecules interact with each other while bound to the catalyst surface and form a product species, which is still bound to the catalyst surface. Finally, the product desorbs from the catalyst surface (endothermic step), leaving the catalyst site free and available for the next reactant species to bind, starting the catalytic cycle over. [21]

A catalyst lowers the kinetic reaction barrier by lowering the free energy difference (*activation energy*) between reactant species and intermediate state(s) (also called transition states, usually denoted by the symbol ‡). The dependence of *reaction rate constant*, k, on the activation energy E_a and temperature T is approximately[1]

[1] Arrhenius equation is an empirical equation, and it is a very good approximation of real world behavior. In reality, the overall rate of a catalytic reaction depends on the temperature in a very complicated way. For example, transition state theory (TST) shows that prefactor A may be proportional to temperature, but this dependency can usually be neglected. [21]

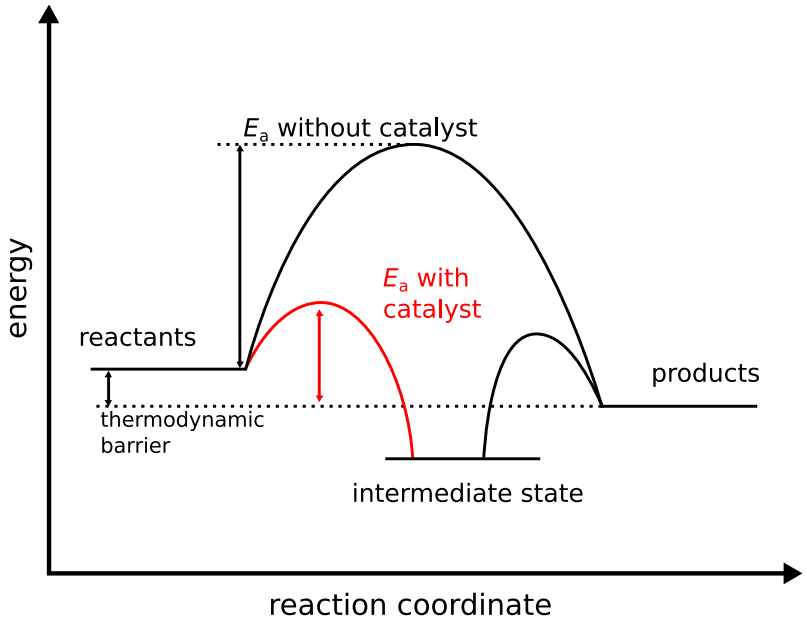

Figure 2.1 *Potential energy diagram of a catalytic and non-catalytic reaction paths. The activation energy E_a of the alternative path is lower compared to the non-catalytic path. The free energy difference between reactants and products, known as the reaction energy or the thermodynamic barrier, is the same regardless of the reaction path.*

governed by *Arrhenius equation*

$$k = K \exp\left(-\frac{E_a}{RT}\right) \tag{2.1}$$

where K is a prefactor, R is the universal gas constant, and T is the absolute temperature. It is also common to use the Boltzmann constant k_B instead of R. E_a has the same units as RT or k_BT. Another interpretation of the Arrhenius equation is

$$k = K' \exp\left(-\frac{\Delta G^{\ddagger}}{RT}\right) \tag{2.2}$$

where $\Delta G^{\ddagger}$ is the *standard free energy of activation*, and K' is a prefactor (the apostrophe emphasizes that Equations (2.1) and (2.2) have different prefactors) [19]. Because the activation energy and temperature are in the exponential term, changes in temperature and/or activation energy have a huge impact on the reaction rate. As a catalyst lowers the activation energy of a reaction, the reaction rate may increase by several magnitudes. Forward and reverse reactions are both accelerated to the same extent. [19, 21]

It is noteworthy that presence of a catalyst changes the reaction kinetics but not

the thermodynamics. It does not change the reaction energy, *i.e.* the free energy difference between reactants and products, also called the thermodynamic barrier. In other words, a catalyst cannot make a reaction to occur, if the reaction would not occur without the catalyst. The equilibrium constant for the overall reaction is also not affected by the catalyst. Catalyst is not a reactant species nor a product species and it is not consumed in the reaction. It continues to affect the reaction until degradation occurs, for example catalyst nanoparticles may deform over time. [21]

Figure 2.1 is a very simplified illustration of what is really going on in catalytic processes in the molecular level. The number of possible intermediate steps and reaction paths may be very large, even if the chemical reaction equations look simple [22]. In experimental and industrial conditions, *i.e.* in aqueous solutions, there are electrochemical driving forces such as pH and applied potential U that have to be taken into account when constructing a realistic model of a catalysis process [24]. In addition the environment of the catalyst surface may contain surface defects and impurities in real operation conditions. Charging of the surface and the liquid phase being in direct contact with the catalyst surface also cause additional difficulties in electrocatalysis modeling [23]. All these contribute to the fact that understanding the full catalytic cycle even for simple surface reactions is very challenging. [22]

2.3 Electrochemistry

An electrochemical reaction takes place in a *cell* which consists of two *electrodes*. The real chemical changes at the electrodes are described by *half-reactions*. Electrodes are standardized by measuring their potentials against so called *reference electrode*. Commonly used reference electrodes are standard hydrogen electrode (SHE), normal hydrogen electrode (NHE), and reversible hydrogen electrode (RHE). [19, 25]

In an electrochemical device, the half-reactions at the electrodes are heterogeneous. Compared to the non-electrochemical heterogeneous catalysis, in electrocatalysis the electrodes can transfer electric charge to or from the reactant species. The overall cell reaction is a *redox* reaction, whereas the electrode half-reactions are called *reduction reaction* and *oxidation reaction*. In a reduction reaction, an *oxidant* gains electrons and its oxidation state decreases. An oxidation reaction is the opposite; a *reductant* loses electrons and its oxidation state increases. From now on, the oxidized form (the oxidant) of a system is denoted by O and the reduced form (the reductant) by R. Thus the general form of an electrochemical (electron-transfer) reduction reaction is

$$\mathrm{O} + n\mathrm{e}^- \underset{k_b}{\overset{k_f}{\rightleftharpoons}} \mathrm{R} \tag{2.3}$$

where e^- denotes a single electron, n is the stoichiometric number of electrons involved in the reaction, and k_f and k_b denote the rate constants of forward and backward reactions, respectively. The electrode where the reduction reaction occurs is called a *cathode*, and the electrode where oxidation reaction (the opposite of Eq. (2.3)) occurs is called an *anode*. In electrochemistry it is common to define the reaction rate v of an electrode reaction as

$$v = \frac{i}{nFA} = \frac{j}{nF} \tag{2.4}$$

where i is the electric current, F is the Faraday constant, A is the cross-sectional area of the electrode, and j is the current density. The reaction rate v has units of mol $s^{-1}m^{-2}$. [19]

The forward reaction in Eq. (2.3) is a reduction and therefore it occurs at the cathode. The backward reaction is an oxidation and occurs at the anode. The electric current originates from the electron transfer between the electrodes. Both electrodes contribute to the total current i, whose cathodic and anodic components are denoted by i_c and i_a, respectively. The overall current is $i = i_c - i_a$. [19]

The rate of the forward reaction in Eq. (2.3), v_f, must be proportional to the surface concentration of O. If the concentration of O at distance x from the surface and at time t is denoted as $C_O(x,t)$, the surface concentration of O is $C_O(0,t)$. Rate constant k_f links [19] the forward reaction rate to the surface concentration

$$v_f = k_f C_O(0,t) \tag{2.5}$$

and similarly for the backward reaction

$$v_b = k_b C_R(0,t) \tag{2.6}$$

The net reaction rate is acquired by subtracting the backward rate from the forward rate

$$v = v_f - v_b = k_f C_O(0,t) - k_b C_R(0,t) = \frac{i}{nFA} \tag{2.7}$$

which, rearranged, yields an equation for the total current

$$i = nFA\Big[\underbrace{k_f C_O(0,t)}_{\text{cathode}} - \underbrace{k_b C_R(0,t)}_{anode}\Big] \tag{2.8}$$

It was mentioned above that the reaction rate of a heterogeneous catalytic reaction

follows Arrhenius equation (Eq. (2.2)), and depends on the activation barrier (represented by either E_a or $\Delta G^\ddagger$). However, in electrochemistry it is possible to shift the activation barrier by a potential change [19]. In other words, the kinetics of a reaction occurring on the electrode surface are strongly affected by the electrode potential, and it is possible to drive the reaction out of equilibrium. Therefore, the rate constant for a heterogeneous electrochemical reaction is a function of the applied potential E. The next section will present how the equations governing the electrode reaction kinetics emerge. The relationship between the reaction rate (current) and the applied potential will be derived.

2.4 Electrode Kinetics

This section is a brief introduction to electrode kinetics by applying theory known as *Butler–Volmer model*. The model predicts the Nernst equation and the Tafel equation, both of which have been experimentally confirmed and a valid theory of electrode kinetics must predict them. The theoretical approach into electrode kinetics provides insight that will be useful in later chapters, because experimental data is usually presented in form of Tafel plots and current–overpotential curves, which arise from the model.

This section considers the electrode kinetics of the simplest possible electrode process, involving only a one-electron transfer, expressed by

$$\mathrm{O} + \mathrm{e}^- \underset{k_b}{\overset{k_f}{\rightleftharpoons}} \mathrm{R} \tag{2.9}$$

An electrochemical cell has several reference points, most importantly the formal potential of the electrode couple, $E^{0'}$, and the equilibrium potential of the cell, E_eq. $E^{0'}$ is a more general reference point, whereas the equilibrium state (E_eq) does not always exist, *e.g.* if the cathode and anode reactions are poorly chosen. The potential difference between the applied potential E and the equilibrium potential

$$\eta = E - E_\mathrm{eq}. \tag{2.10}$$

is called *overpotential*. [19, 20]

2.4.1 Butler–Volmer Model

The standard free energies of activation at the equilibrium are denoted by $\Delta G^\ddagger_{0,\mathrm{c}}$ and $\Delta G^\ddagger_{0,\mathrm{a}}$ at the cathode and the anode, respectively. The non-equilibrium free

energies of activation at the cathode and anode are denoted by $\Delta G_{\mathrm{c}}^{\ddagger}$ and $\Delta G_{\mathrm{a}}^{\ddagger}$, respectively. As aforementioned, it is possible to shift these activation barriers by applying potential E, and the governing equations are

$$\Delta G_{\mathrm{c}}^{\ddagger} = \Delta G_{0,\mathrm{c}}^{\ddagger} + \alpha F(E - E^{0'}) \tag{2.11}$$

$$\Delta G_{\mathrm{a}}^{\ddagger} = \Delta G_{0,\mathrm{a}}^{\ddagger} - (1-\alpha) F(E - E^{0'}) \tag{2.12}$$

where α is called the *charge transfer coefficient*, whose value is between 0 and 1 and it determines how much the applied potential affects the charge transfer. It is a measure of the symmetry of the energy barrier, and depends on the shape of the intersection of the anode and cathode free energy curves (as plotted against the reaction coordinate)[2]. [19, 20]

Now, if the rate constants at the cathode (k_{f}) and the anode (k_{b}) are assumed to have the Arrhenius form, substituting $\Delta G_{\mathrm{a}}^{\ddagger}$ and $\Delta G_{\mathrm{c}}^{\ddagger}$ into Eq. (2.2) yields

$$k_{\mathrm{f}} = K_{\mathrm{f}} \exp\left(-\frac{\Delta G_{\mathrm{c}}^{\ddagger}}{RT}\right) = K_{\mathrm{f}} \exp\left(-\frac{\Delta G_{0,\mathrm{c}}^{\ddagger}}{RT}\right) \exp\left(-\frac{\alpha F}{RT}(E - E^{0'})\right) \tag{2.13}$$

$$k_{\mathrm{b}} = K_{\mathrm{b}} \exp\left(-\frac{\Delta G_{\mathrm{a}}^{\ddagger}}{RT}\right) = K_{\mathrm{b}} \exp\left(-\frac{\Delta G_{0,\mathrm{a}}^{\ddagger}}{RT}\right) \exp\left(\frac{(1-\alpha) F}{RT}(E - E^{0'})\right) \tag{2.14}$$

where K_{f} and K_{b} are prefactors. The rate constants clearly have terms that depend only on the equilibrium free energies and terms that depend on the potential.

At the formal potential $E = E^{0'}$ the forward and reverse rate constants are equal. This rate constant value is called *the standard rate constant*, denoted here by k_0

$$k_0 = k_{0,\mathrm{f}} = K_{\mathrm{f}} \exp\left(-\frac{\Delta G_{0,\mathrm{c}}^{\ddagger}}{RT}\right) \tag{2.15}$$

$$= k_{0,\mathrm{b}} = K_{\mathrm{b}} \exp\left(-\frac{\Delta G_{0,\mathrm{a}}^{\ddagger}}{RT}\right) \tag{2.16}$$

These equations represent the reaction rate at the equilibrium. The standard rate constant can be physically interpreted as a measure of the kinetic facility. A system with large k_0 will achieve equilibrium faster than a system with small k_0.

[2] More details on α can be found in pp. 94–95 and 97–98 in reference [19].

The rate constants at other potentials can now be expressed as

$$k_\mathrm{f} = k_0 \mathrm{e}^{-\alpha f(E-E^{0'})} \tag{2.17}$$

$$k_\mathrm{b} = k_0 \mathrm{e}^{(1-\alpha) f(E-E^{0'})} \tag{2.18}$$

where $f = \frac{F}{RT}$. Substituting these forward and backward rate constants into Eq. (2.8) results in a current–potential relation

$$i = nFAk_0 \Big[\underbrace{C_\mathrm{O}(0,t)\mathrm{e}^{-\alpha f(E-E^{0'})}}_{cathode} - \underbrace{C_\mathrm{R}(0,t)\mathrm{e}^{(1-\alpha) f(E-E^{0'})}}_{anode} \Big] \tag{2.19}$$

which describes the current–potential (i–E) characteristics of the electrode reactions.

2.4.2 Nernst Equation and Exchange Current

Inspecting the current–potential equation (2.19) at the equilibrium state $E = E_\mathrm{eq}$, where the net current is zero, yields

$$\begin{aligned} & C_\mathrm{O}(0,t)\mathrm{e}^{-\alpha f(E_\mathrm{eq}-E^{0'})} = C_\mathrm{R}(0,t)\mathrm{e}^{(1-\alpha) f(E_\mathrm{eq}-E^{0'})} \\ \Leftrightarrow & \frac{C_\mathrm{O}(0,t)}{C_\mathrm{R}(0,t)} = \frac{\mathrm{e}^{(1-\alpha) f(E_\mathrm{eq}-E^{0'})}}{\mathrm{e}^{-\alpha f(E_\mathrm{eq}-E^{0'})}} = \mathrm{e}^{(1-\alpha) f(E_\mathrm{eq}-E^{0'})+\alpha f(E_\mathrm{eq}-E^{0'})} = \mathrm{e}^{\frac{F}{RT}(E_\mathrm{eq}-E^{0'})} \end{aligned} \tag{2.20}$$

Because the system is at equilibrium, the surface concentrations of R and O are equal to their bulk concentrations C^*_R and C^*_O, respectively [19]. Rearranging the equation results in

$$E_\mathrm{eq} = E^{0'} + \frac{RT}{F} \ln \left(\frac{C^*_\mathrm{O}}{C^*_\mathrm{R}} \right) \tag{2.21}$$

which is the well-know *Nernst equation.*

The *exchange current* i_0 is defined as equal in magnitude to both current components, i_c and i_a. Therefore, it can be solved from the equilibrium state of Eq. (2.19) from either i_c or i_a:

$$i_0 = i_\mathrm{a} = i_\mathrm{c} = FAk_0 C^*_\mathrm{O} \mathrm{e}^{-\alpha f(E_\mathrm{eq}-E^{0'})} \tag{2.22}$$

The proportionality of i_0 and k_0 can be derived by rising the exponential form of Nernst equation (Eq. (2.20)) to the $-\alpha$ power and using the bulk concentrations as

above, yielding

$$\mathrm{e}^{-\alpha f(E_{\mathrm{eq}}-E^{0'})} = \left(\frac{C_{\mathrm{O}}^*}{C_{\mathrm{R}}^*}\right)^{-\alpha} \tag{2.23}$$

Substituting this into Eq. (2.22) gives

$$i_0 = FAk_0(C_{\mathrm{O}}^*)^{(1-\alpha)}(C_{\mathrm{R}}^*)^{\alpha} \tag{2.24}$$

Because the exchange current is proportional to k_0, it can often be substituted for k_0 in kinetic equations. Furthermore, if the bulk concentrations are equal the exchange current becomes

$$i_0 = FAk_0C \tag{2.25}$$

where $C = C_{\mathrm{O}}^* = C_{\mathrm{R}}^*$. It is also common in the literature to use *exchange current density* $j_0 = i_0/A$ instead of the exchange current. [19]

2.4.3 Current–overpotential Equation

The advantage of working with j_0 (or i_0) rather than k_0 is that the current can be described in terms of the overpotential, η (the deviation from the equilibrium potential), rather than the formal potential, $E^{0'}$ [19]. The relationship between the exchange current density and overpotential can be derived as follows: dividing (2.19) by (2.24) yields

$$\begin{aligned}\frac{i}{i_0} = \frac{j}{j_0} &= \frac{C_{\mathrm{O}}(0,t)\mathrm{e}^{-\alpha f(E-E^{0'})}}{(C_{\mathrm{O}}^*)^{(1-\alpha)}(C_{\mathrm{R}}^*)^{\alpha}} - \frac{C_{\mathrm{R}}(0,t)\mathrm{e}^{(1-\alpha)f(E-E^{0'})}}{(C_{\mathrm{O}}^*)^{(1-\alpha)}(C_{\mathrm{R}}^*)^{\alpha}} \\ &= \frac{C_{\mathrm{O}}(0,t)}{C_{\mathrm{O}}^*}\mathrm{e}^{-\alpha f(E-E^{0'})}\left(\frac{C_{\mathrm{O}}^*}{C_{\mathrm{R}}^*}\right)^{\alpha} - \frac{C_{\mathrm{R}}(0,t)}{C_{\mathrm{R}}^*}\mathrm{e}^{(1-\alpha)f(E-E^{0'})}\left(\frac{C_{\mathrm{O}}^*}{C_{\mathrm{R}}^*}\right)^{-(1-\alpha)}\end{aligned}$$

Equations (2.20) and (2.23) can be used to evaluate $\left(\frac{C_{\mathrm{O}}^*}{C_{\mathrm{R}}^*}\right)^{\alpha}$ and $\left(\frac{C_{\mathrm{O}}^*}{C_{\mathrm{R}}^*}\right)^{-(1-\alpha)}$. Substituting them yields

$$j = j_0\left[\underbrace{\frac{C_{\mathrm{O}}(0,t)}{C_{\mathrm{O}}^*}\mathrm{e}^{-\alpha f\eta}}_{cathode} - \underbrace{\frac{C_{\mathrm{R}}(0,t)}{C_{\mathrm{R}}^*}\mathrm{e}^{(1-\alpha)f\eta}}_{anode}\right] \tag{2.26}$$

This is the *current–overpotential equation.* Current–(over)potential curves are commonly called the *polarization curves.* It is important to note that this equation is an approximation and does not take into account certain effects that also influence the

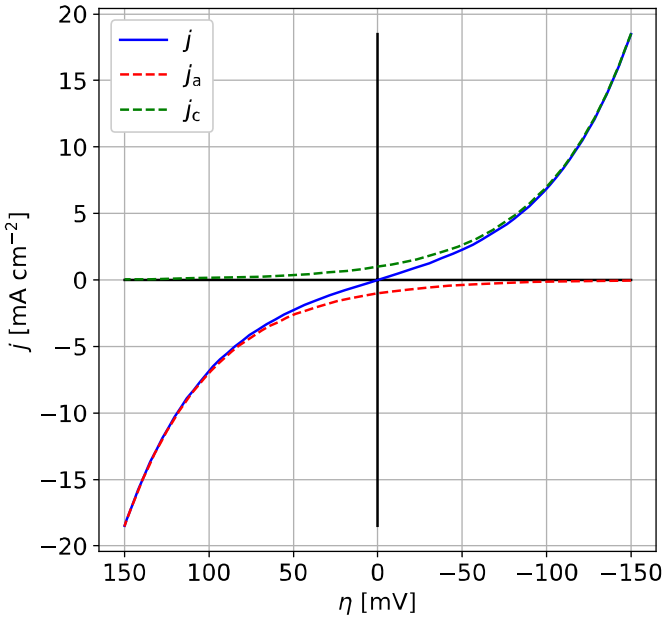

Figure 2.2 *An example of a polarization curve (j–η behavior) with $\alpha = 0.5$, $T = 298$ K, and $j_0 = 1.0 \cdot 10^{-3}$ A/cm^2. The solid blue line is the total current, and the green and red dashed lines represent the cathodic and anodic current components, respectively.*

current density, such as mass-transfer limitations on the electrodes[3]. At low current densities the mass-transfer effects can be ignored and the surface concentrations are approximately equal to the bulk concentrations [19]. Therefore, Eq. (2.26) reduces into the so-called *Butler–Volmer equation*

$$j = j_0 \left[\underbrace{\mathrm{e}^{-\alpha f \eta}}_{cathode} - \underbrace{\mathrm{e}^{(1-\alpha) f \eta}}_{anode} \right] \tag{2.27}$$

The current–overpotential curve predicted by (2.27) is shown in Fig. 2.2. The total current is the blue solid line, whereas the cathodic and anodic components are plotted in green and red dashed lines, respectively. At large positive (negative) η the cathodic (anodic) component is negligible. Figure 2.3 demonstrates the influence of the transfer coefficient α on the shape of polarization curves.

Equation (2.27) holds only for low overpotentials, because if the overpotential and therefore the current becomes large enough, the mass-transfer effect start to limit the current instead of the heterogeneous kinetics, and the current will asymptotically approach a limit value[4]. At low currents, *i.e.* when the mass-transfer effects are not

[3]Other notable effects include for example ohmic losses and material stability. These are out of the scope of this thesis.

[4]The effect of the limiting current is not shown in Figures 2.2 and 2.3 because it does not arise from Eq. (2.27).

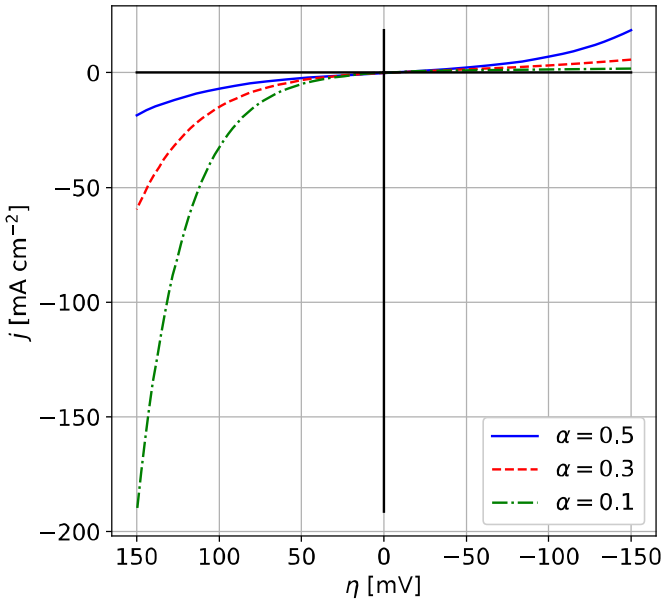

Figure 2.3 *The effect of transfer coefficient on j–η behavior. $T = 298\ K$ and $j_0 = 1.0 \cdot 10^{-3}\ A/cm^2$, while $\alpha = 0.5$ (blue solid line), $\alpha = 0.3$ (red dashed line), and $\alpha = 0.1$ (green dash-dot line).*

important, the overpotential is called the *activation overpotential*. The activation overpotential is a measure of the activity of the electrodes, because it provides the activation energy required to drive the heterogeneous catalysis process at the rate corresponding to the current. [19]

2.4.4 Tafel Equation

If the overpotential η is a large positive (negative) value, the cathodic (anodic) component in Eq. (2.27) vanishes and the equation simplifies into

$$j = j_0 \mathrm{e}^{-\alpha f \eta} \tag{2.28}$$

which rearranged yields

$$\eta = \frac{RT}{\alpha F} \ln j_0 - \frac{RT}{\alpha F} \ln j \tag{2.29}$$

This can be recognized as a form of *Tafel equation*, originally observed experimentally by Tafel in 1905 [26] as

$$\eta = a + b \log_{10} i \tag{2.30}$$

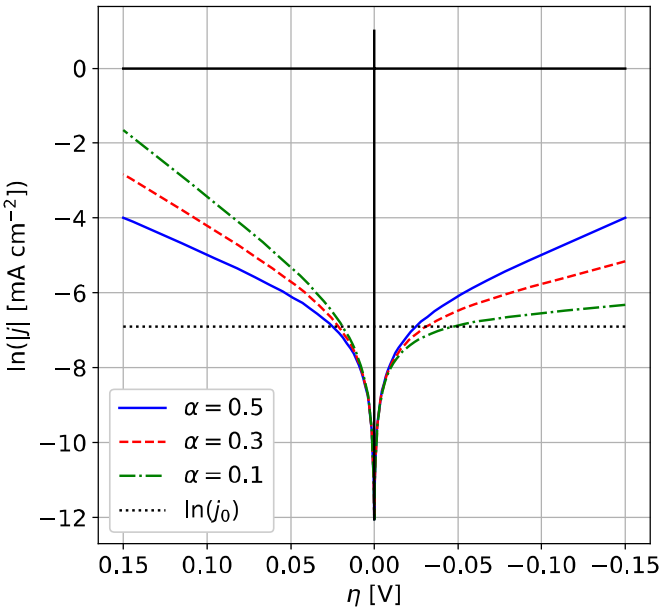

Figure 2.4 *Tafel plots* ($\ln(|j|)$ *against* η) *with different transfer coefficient values.* $T = 298$ *K and* $j_0 = 1.0 \cdot 10^{-3}$ *A/cm*^{2}, *while* $\alpha = 0.5$ *(blue solid line),* $\alpha = 0.3$ *(red dashed line), and* $\alpha = 0.1$ *(green dash-dot line).*

where a and b are empirical constants. The constant b is commonly called the *Tafel slope*. Tafel slopes are commonly presented in the units of mV/decade, representing how large overpotential change is required to change the current density by 10 mA/cm^2. Tafel plots are useful because they allow determining the transfer coefficient and the exchange current from experimental measurements. Values for the empirical constants a and b can be derived from Eq. (2.29) as [19]

$$a = \frac{2.3RT}{\alpha F} \ln j_0 \tag{2.31}$$

$$b = \frac{-2.3RT}{\alpha F} \tag{2.32}$$

Figure 2.4 shows natural logarithms of the magnitudes of the current densities plotted in Figure 2.3. Logarithm with base 10 is also sometimes used in the literature. Linear behavior is clearly shown at large enough positive or negative overpotentials, as predicted by the Tafel equation. Extrapolated these lines intercept at $\eta = 0$ where $\ln j = \ln j_0$. Tafel analysis only works when the reaction is out of equilibrium, *i.e.* when the overpotential is near zero the behavior is far from linear, because both current components (cathodic and anodic) contribute to the total current. When the so far ignored mass-transfer effects come into play, the linear behavior can be expected to end and the curves will approach a constant limit value asymptotically.

3. HYDROGEN EVOLUTION REACTION

A variety of devices can be utilized to perform the electrochemical water-splitting. Such devices can roughly be classified into water electrolysis and water photolysis devices. Water electrolyzers require an external and preferably a renewable source of electricity, whereas photoelectrochemical and photocatalytic water-splitting devices produce charge carriers by themselves by absorbing sunlight. Regardless of the type of the device, the total water-splitting reaction is [5, 7]

$$\mathrm{H_2O} \longrightarrow \mathrm{H_2} + \frac{1}{2}\mathrm{O_2} \tag{3.1}$$

At the standard conditions, an energy input of $\Delta G = 237.1$ kJ/mol is required to drive this reaction. This corresponds to a thermodynamic voltage requirement of 1.23 V. [7, 27]

In a water-splitting cell, the hydrogen evolution reaction (HER) occurs at the cathode, and the oxygen evolution reaction (OER) occurs at the anode[1]. HER is a process where protons and electrons are combined to form molecular hydrogen $\mathrm{H_2(g)}$ [28]. It is one of the most important reactions in electrochemistry [29], and there has been an academic and a technological interest towards it for over 70 years [27]. While HER can occur in both acidic and alkaline environments[2] [27], the present work will focus primarily on HER in acidic media.

Fundamental understanding of HER is very important, because it is one of the simplest electrochemical reactions, and it is an essential benchmark reaction in hydrogen production and fuel cell techniques. HER also bridges the gap between the fundamental electrocatalysis and the practical catalyst design [27]. Understanding HER is also important from a technological perspective, because it is the cathode half-reaction in water-splitting devices. In the future such devices could become an important, environmentally friendly source of molecular hydrogen ($\mathrm{H_2}$), a majority of

[1] More information of the OER and the recent developments in the OER electrocatalysts can be found for example in [3].

[2] In HER related experimental measurements, acidic solutions are typically 0.5–1.0 M $\mathrm{H_2SO_4}$ (mol per liter of solution, corresponds to pH 0.3–0.0) and alkaline solutions 0.1–1.0 M NaOH or KOH (pH 13–14).

which is currently derived from steam-reformed methane, producing large amounts of CO_2 as an unwanted side product. Therefore, it is important to develop efficient, affordable and earth-abundant electrocatalysts for hydrogen evolution. Currently the best performing electrocatalysts for HER and OER are Pt and RuO_x, respectively, both of which are expensive and scarce. [5]

This chapter is a brief introduction to the hydrogen evolution reaction. It presents the reaction mechanisms and the corresponding reaction equations for HER in acidic environments. The characteristics of a good HER electrocatalyst are discussed, followed by a short summary of the recent developments in HER catalyst design and materials screening.

3.1 HER Mechanisms in Acidic Environments

In an acidic environment the total reaction for the hydrogen evolution is [3, 24, 29]

$$2\,\mathrm{H^+} + 2\,\mathrm{e^-} \longrightarrow \mathrm{H_2(g)} \tag{3.2}$$

where H^+ is an aqueous proton, e^- is an electron and $H_2(g)$ is gaseous, molecular hydrogen. HER is a two-electron transfer reaction with one intermediate state, denoted generally by H^*. There are two possibilities for the intermediate state, and therefore HER can proceed through two mechanisms called the Volmer–Tafel (VT) and the Volmer–Heyrovsky (VH) mechanism [24]. The reaction equations representing the different steps of HER are

$$\mathrm{H^+ + S + e^- \longrightarrow S{-}H} \qquad \text{Volmer step} \tag{3.3}$$

$$\mathrm{S{-}H + S'{-}H \longrightarrow S/S' + S'/S{-}H_2} \qquad \text{Tafel step} \tag{3.4}$$

$$\mathrm{S{-}H + H^+ + e^- \longrightarrow S{-}H_2} \qquad \text{Heyrovsky step} \tag{3.5}$$

$$\mathrm{S{-}H_2 \longrightarrow S + H_2(g)} \qquad \text{desorption} \tag{3.6}$$

The Volmer step is the first step in both mechanisms: a hydrogen atom binds to a site (S) on the surface of an electrocatalyst. Next, there are two different ways in which the reaction can proceed: (i) *The Tafel step*: another hydrogen atom binds to a separate surface site S′, which may be similar or different type of site compared to S. The two hydrogen atoms recombine to form an H_2 molecule which is bound to either S or S′. (ii) *The Heyrovsky step*: another hydrogen atom binds directly on the already adsorbed hydrogen atom (S−H), forming an H_2 molecule which is bound to the surface site S. After either the Tafel or the Heyrovsky step, the reaction finishes by the desorption of the $H_2(g)$ molecule. [3, 7, 24]

Depending on the properties of an electrocatalyst, any of the three aforementioned steps can be the rate-limiting step of HER. The Tafel slope is an inherent property of the catalyst, determined by the rate-limiting step [30]. Therefore, measuring the Tafel slope may provide valuable information on the HER reaction mechanism of the catalyst in question. The theoretical Tafel slopes that correspond to the different rate-limiting HER mechanisms in acidic media are [30, 31, 32, 33]

$$b = \frac{-2.3RT}{\alpha F} \approx -116 \text{ mV/decade} \qquad \text{Volmer reaction} \tag{3.7}$$

$$b = \frac{-2.3RT}{2F} \approx -30 \text{ mV/decade} \qquad \text{Tafel reaction} \tag{3.8}$$

$$b = \frac{-2.3RT}{(1+\alpha)F} \approx -40 \text{ mV/decade} \qquad \text{Heyrovsky reaction} \tag{3.9}$$

calculated with a transfer coefficient of $\alpha \approx 0.5$ for HER [30, 31].

A platinum surface has a Tafel slope of -29 mV/decade in strong acids [34, 35]. HER is known to proceed through the Volmer–Tafel mechanism on a Pt surface [30, 31]. At low overpotentials, the Tafel step (recombination) is known to be the rate-limiting step, as indicated by the measured low Tafel slope and Eq. (3.8) [30]. Non-precious HER electrocatalysts usually have Tafel slopes ranging from -40 to -120 mV/decade [36], whereas some may have almost as low Tafel slopes as Pt, such as in the case of Ni_5P_4 pellets (-33 mV/decade) [35] and $NiMoN_x$|C nanosheets on carbon (-35 mV/decade) [37].

3.2 Characteristics of a Good HER Catalyst

Identification of new active electrocatalytic materials is a major part of modern electrocatalysis [38]. The performance of an electrocatalyst is defined primarily by three constituents: activity, selectivity, and stability [38]. A valid HER catalyst should be highly active towards HER, therefore identifying highly active catalyst materials is always the first step in the search for new catalysts [38]. Various experimental and theoretical methods exist to determine the activity of a catalyst [7]. The experimental methods for measuring activity are presented in Section 3.3, whereas the theoretical methods (namely the ΔG_{H^*} descriptor) are discussed in Chapter 4.

Selectivity describes the fraction of a reactant that is converted to the desired product. In the context of HER, the selectivity is usually not a critical issue, because in acidic environments the only feasible product is hydrogen. In general, selectivity is very important in green chemistry[3], because a catalyst with high selectivity helps

[3]Chemistry that is environmentally friendly, *e.g.* avoids the use of toxic materials.

to reduce the amount of wasted reactants. For an HER catalyst, the selectivity can be determined by measuring the concentration of the evolved H_2 using *e.g.* volume displacement or gas chromatography [7]. [21]

Most of the studies on new HER catalysts focus on the activity. However, especially stability is of great importance in industrial applications, because an HER catalyst should be stable and work under the operating conditions (*e.g.* pH, temperature and the electrode potential of an electrochemical cell [9]) for a long time, preferably as long as possible. The stability of a catalyst includes chemical, thermal, and mechanical stability. Together they determine the lifetime of the catalyst, *i.e.* how long the catalyst can continuously catalyze HER before it degrades and deactivates. Therefore, a high stability is crucial for the economics in practical electrocatalysis. Many various factors influence the stability of a catalyst, *e.g.* acidic conditions on the cathode, poisoning, decomposition and deformation. Experimentally the stability of a catalyst can be determined by measuring its activity as a function of time. The long-term stability is difficult to determine using computer simulations, because in practice the time scales are very large compared to what can be done with methods such as DFT or kinetic Monte Carlo. [21, 38]

In addition to the aforementioned catalyst characteristics, an applicable HER catalyst material should be affordable, recyclable, easy to produce and earth-abundant [9][21, p. 167]. These characteristics eventually determine if an HER catalyst is valid for industrial applications and large-scale production of hydrogen. The high cost and scarcity of platinum, the best known HER catalyst, are the main reasons why alternative, non-precious HER catalysts are searched in the first place [4, 5].

3.3 HER Catalyst Activity Measurements

The activity is a critical performance characteristic of a catalyst. The experimental methods for determining the activity of an HER catalyst have two categories: *total electrode activity* measurements and *intrinsic activity* measurements. The total electrode activity measurements are normalized to the geometric area of an electrode, whereas the intrinsic activity measurements aim to measure the catalytic activity of each catalytic site. These different methodologies are fundamentally related, as will be seen below. [7]

The activity of an electrocatalyst system can generally be improved by increasing the number of active sites or by increasing the intrinsic activity of each site. These are not mutually exclusive and will result in improved total electrode activity. The number of active sites can be increased *e.g.* through improved catalyst structuring

or increased catalyst loading. Improving the intrinsic activity is important, because there are physical limitations such as charge and mass transport that limit how much the number of active sites can be increased. Various methods may improve the intrinsic activity, *e.g.* doping and applying strain, however these are catalyst-dependent. Improved intrinsic activity also helps in reducing catalyst costs, because it allows the catalyst loading to be decreased. [3]

3.3.1 Total Electrode Activity Measurements

The total electrode activity measurements are based on measuring the catalytic current as a function of the applied potential. The measurements are typically carried out by cyclic voltammetry (CV) or linear sweep voltammetry (LSV). The potential scale is calibrated to a suitable reference electrode, which for the water-splitting reactions is the reversible hydrogen electrode (RHE). The current is normalized to the surface area of the electrode, therefore the total electrode activity is also referred to as *geometric activity*. [7]

A generally used metric of the catalytic activity of an HER electrode is the overpotential required to reach an operating current density of the device of interest. Commercial water-splitting devices typically operate at high current densities of 1–10 mA/cm^2 [4]. Water electrolyzers typically operate at current densities around 1–2 mA/cm^2, whereas 10 mA/cm^2 is commonly used to compare catalyst materials for PECs. The potential at which the catalytic current is first observed is called the *onset potential*. The onset potential and the Tafel slope of a catalyst determine the overpotential required to reach the operating current, because the overpotential at any current can be calculated from the Tafel equation once the onset potential and the Tafel slope are known. [7]

Figure 3.1 illustrates how the activities of HER electrodes can be compared. It represents the linear sweep voltammograms of four theoretical catalysts; the current density is plotted as a function of the potential. At the current density of 10 mA/cm^2 (the dashed line), the catalyst illustrated by the green curve requires the lowest potential. Therefore, it performs better than the other three catalyst. The influence of the Tafel slope is illustrated by the two catalysts represented in red and blue. They perform similarly at the current density of 10 mA/cm^2 but their Tafel slopes are different. In low current density regions (< 10 mA/cm^2), the catalyst represented in blue requires lower potential and therefore outperforms the catalyst represented in red for devices that operate at low current densities. The catalyst represented in red would perform better in devices which run at high current densities (> 10 mA/cm^2).

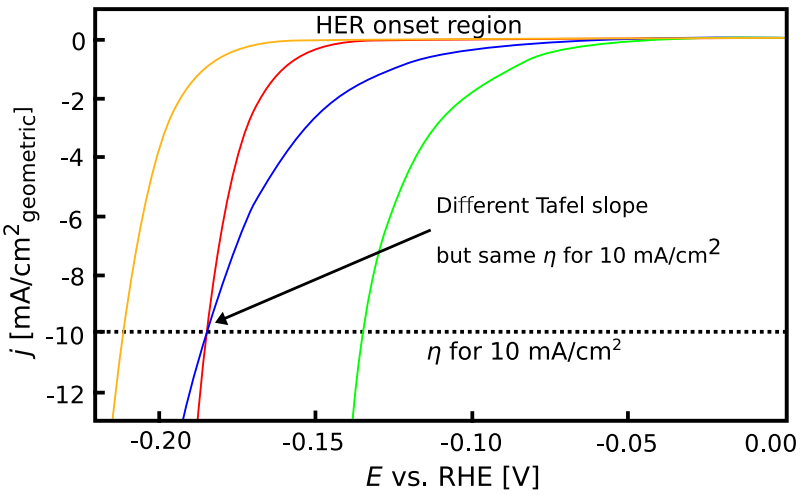

Figure 3.1 *The linear sweep voltammograms of four theoretical catalysts. The dashed line represents the current density of 10 mA/cm^2, which is a commonly used metric to compare the total electrode activities. The catalytic current is first observed in the onset region (at the onset potential). The catalyst represented in green is the best catalyst at $j =$ 10 mA/cm^2. The influence of the Tafel slope is illustrated by the two catalysts represented in red and blue. Blue would perform better than red in low current density regions ($<$ 10 mA/cm^2), whereas red would perform better than blue in high current density regions ($>$ 10 mA/cm^2). The Figure is adapted from [7].*

In conclusion, low Tafel slopes are desirable for electrolyzers and high Tafel slopes for PECs. [7]

The total electrode activity measurements are useful in practice, when complete HER electrodes are compared with each other. However, they are not ideal in rational catalyst design, because they do not reveal information of the underlying physical and chemical events that define the catalytic activity of a material. This information can be provided by intrinsic activity measurements, which are challenging due to technical limitations. [7, 38]

3.3.2 Intrinsic Activity Measurements

The intrinsic activity measurements seek to measure the activity of each individual catalytic site. This is of great importance in rational catalyst development, especially when determining the activity of novel catalysts, because it provides insight into the relationship of molecular level structural properties and catalyst's activity. Besides the activity of each site, the total number of active sites is also a critical parameter for understanding this relationship. [7]

The activity of a catalytic site is commonly described by the *turnover frequency*

(TOF) per-site, also called the *turnover rate* [7, 39]. TOF describes the number of reactant molecules that a single catalytic center can convert into products in a given time [39]. From the perspective of the whole catalyst, TOF is

$$\text{TOF} = \frac{\text{reaction rate}}{\text{density of catalytic sites}} \tag{3.10}$$

where the reaction rate is moles of product per area per unit time (mol m^{-2} s^{-1}) and the density of catalytic sites (centers) is moles of catalytic sites per area (mol m^{-2}). The unit of TOF is usually s^{-1} or sometimes h^{-1} (moles of product per mole of catalytic sites per unit time). In the context of HER, TOF is usually reported as H_2 s^{-1}, denoting "mol H_2 / mol surface atoms / s".

The physical and chemical properties of a catalyst surface primarily determine its TOF [7]. TOF is a chemical reaction rate and therefore it depends on the reaction conditions: temperature, pressure and concentrations [39]. It is difficult to measure because the catalytic sites have to be identified and counted *in situ* (during the catalytic reaction) [39]. The number of active catalytic sites is commonly evaluated by measuring the total active surface area of the catalyst [7]. Determining the number of active sites is always approximate, because catalyst surfaces may be very complex structures and there may exist many different unidentical catalytic sites on the surface with different turnover frequencies. Sites may also interact with each other. If all sites are not equally active, TOF will be an average value. In practice this is always the case, therefore TOF is typically averaged across all surface sites (denoted by TOF_{avg}). The TOF_{avg} value is then used as a descriptor of the catalyst's activity [39]:

$$\text{TOF}_{\text{avg}} = \sum_{i=1}^{S} \text{TOF}_i = \frac{v}{\frac{S}{N_{\text{A}} \cdot A}} \tag{3.11}$$

where v is the reaction rate, S is the number of sites on the electrode surface, N_{A} is the Avogadro's number, and A is the area of the electrode surface. The sum expresses that the average is computed over the turnover frequencies of all different catalytic sites i. In electrochemistry, TOF and the current density depend on the overpotential η. Eq. (2.4) can be used to derive their relationship for HER:

$$\begin{aligned} \text{TOF}_{\text{avg}} &= \frac{j}{nF\frac{S}{N_{\text{A}} \cdot A}} \\ \Leftrightarrow j(\eta) &= S \cdot \text{TOF}_{\text{avg}}(\eta) \cdot \frac{nF}{AN_{\text{A}}}. \end{aligned} \tag{3.12}$$

Equation (3.12) represents the relationship between the total electrode activity (cur-

rent density) and the intrinsic activity (TOF) [7]. In practice the easiest and the most common strategy for determining the intrinsic activity of each catalytic site is to measure the current density and the catalytically active surface area of an electrode, then approximate the number of active surface sites and finally derive the average TOF per site from Eq. (3.12). [7, 40]

In addition to providing fundamental insight of the origins of the catalytic activity, there are also several other reasons why TOF is a good descriptor of the catalytic activity. If the methods and conditions of measurement are fully described, especially the method of identifying and counting the catalytic sites, TOF is a straightforward way to compare data obtained by different experimental groups in different laboratories. TOF values of different catalysts are comparable, enabling comparison of the catalytic activity of potential new HER catalysts and the currently used catalysts. TOF also reveals if a catalyst truly is a catalyst, *i.e.*, if it is a reagent or not, and it can provide a quantitative insight into how catalytic cycles work. [39]

The turnover frequency can be used to determine the effects of heat and mass transfer in heterogeneous catalysis. These phenomena make the experimental measurement of reaction rates difficult. TOFs have to be measured for a given reaction at fixed conditions on two catalytic samples containing different amounts of catalyst materials. If the measured turnover frequencies are identical, the heat and mass transfer effects on the kinetic data are negligible. [39]

3.4 Recent Developments in HER Catalysts

No catalyst has been found to have a better overall HER performance than platinum [3], therefore it is the benchmark catalyst for HER [4]. However, Pt and other platinum-group metals (PGMs) are scarce, expensive and have a high supply risk. This limits their large-scale technological applicability and has induced the search for new PGM-free catalysts for HER [3, 4, 5]. The replacement of Pt with earth-abundant, highly active, stable and affordable HER catalyst remains a great challenge.

The overall rate of HER, Eq. (3.2), in acidic environments has been observed to be determined primarily by the Gibbs free energy of hydrogen adsorption, ΔG_{H^*} [3, 29, 41]. This is reasonable because the adsorbed hydrogen (H^*) is one of the intermediates regardless of the actual reaction path [23]. The Volmer step (adsorption) will limit the reaction rate if the hydrogen binds to the surface too weakly, whereas if the hydrogen binds too strongly the reaction rate is limited by the desorption step [3]. Therefore, a necessary condition for an active and optimal HER catalyst is that

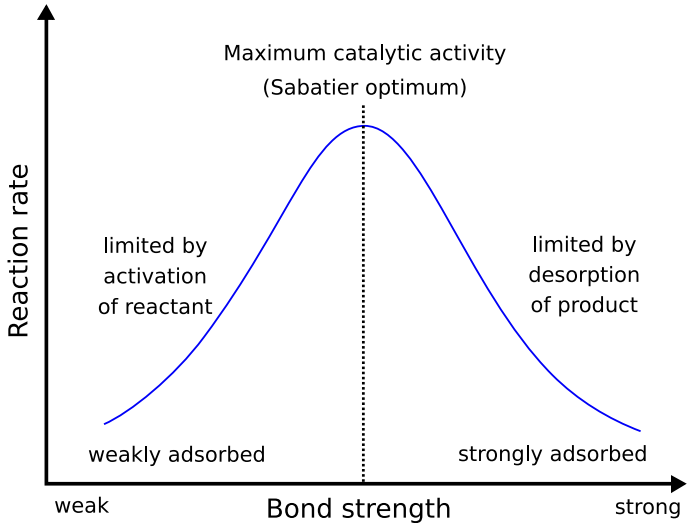

Figure 3.2 *Illustration of the Sabatier principle: "the intermediate species should bind neither too weakly nor too strongly". If the bond between the surface of a catalyst and the intermediate species is too weak, the reaction rate is limited by the adsorption of the reactant species, whereas if the bond is too strong, the reaction rate is limited by the desorption of intermediate species [3][21, p. 261].*

$\Delta G_{H^*} \approx 0$, as originally suggested by Parsons [29, 41]. Finding active HER catalysts thus follows the idea of the *Sabatier principle*, which is illustrated in Figure 3.2. The Sabatier principle states that the interaction between the adsorbates and the catalyst surface should be neither too strong not too weak, because both extremes limit the reaction rate [21, p. 261].

The aforementioned influence of ΔG_{H^*} on the activity of an HER catalyst is generally illustrated as a *volcano plot*. The volcano shape arises when the experimentally measured exchange current densities (which are measures of the catalytic activity) are plotted as a function of the computationally calculated[4] ΔG_{H^*} values for different materials, as presented in Figure 3.3. The results of several kinetic models are also shown in Figure 3.3 [29, 42]. Platinum is near the top of the volcano with its slightly negative ΔG_{H^*} and the highest HER activity [43]. Several other PGMs (Ir, Rh, Pd) also exhibit a good HER performance, whereas the other elements bond with hydrogen either too weakly or too strongly. The reactive metals (such as Fe, Ni, Co) are on the left side of platinum and the unreactive metals (Cu, Ag, Au, Bi) are on the right side [29]. Fig. 3.3 also shows two HER catalysts that were originally discovered computationally: molybdenum disulfide MoS_2 [28] and PtBi surface alloy [42]. It is noteworthy that the ΔG_{H^*} values are not perfectly consistent in the literature. For example Skúlason *et al.* [44] reported ΔG_{H^*} for Pt,

[4]Calculated using the density functional theory at appropriate hydrogen coverages, which will be discussed more in Chapter 4.

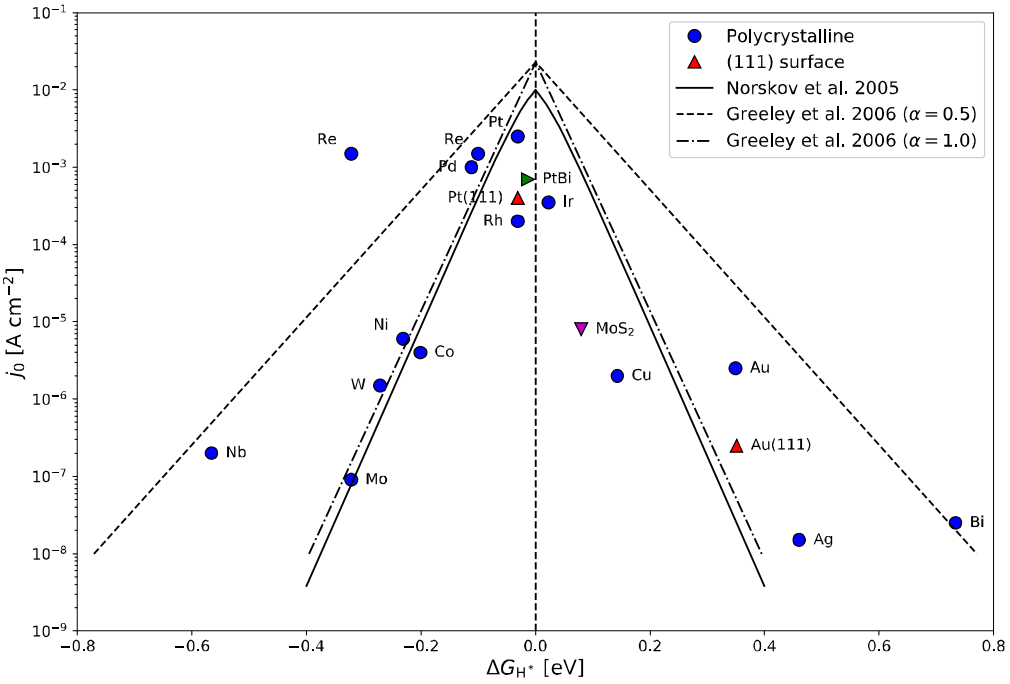

Figure 3.3 *The HER activity volcano: the experimentally measured exchange current densities as a function of the computationally calculated Gibbs free energies of hydrogen adsorption for various catalyst materials: polycrystalline metals (blue), (111) surfaces of platinum and gold (red), close-packed PtBi surface (green), and molybdenum disulfide MoS_2 (magenta). The data is adapted from [3, 23, 43, 44]. The solid black line represents the result of a simple kinetic model by Norskov et al. [29], and the two dashed lines correspond to the activity predictions of two microkinetic models by Greeley et al. [42], who assumed the transfer coefficients (α) of 0.5 and 1.0. Some inconsistencies exist in the values for Pt, Pt(111), and Rh between references [43] and [44]. These values were adapted from [43].*

Pt(111) and Rh to be almost zero, whereas Jaramillo *et al.* [43] reported them to be closer to -0.1 eV. Two very different ΔG_{H^*} values were reported for rhenium (Re), both shown in Fig. 3.3 [43, 44].

Over the last decade many promising alternatives for the platinum HER catalysts have been developed. MoS_2 and phosphide families of materials in particular have emerged as viable HER catalyst candidates in acidic environments with their excellent performance and stability [4]. Other promising non-precious HER catalysts are for example various carbides, selenides, nitrides, and borides [3, 24]. Ni-Mo alloys and Ni-based homogeneous catalysts are promising catalysts for HER in alkaline solutions [3]. MoS_2-based HER catalysts are presented briefly in Subsection 3.4.1, phosphide-based HER catalysts in Subsection 3.4.2, and all other PGM-free HER catalysts are discussed in Subsection 3.4.3. The current densities and the average turnover frequencies for some of the promising non-precious HER catalysts are represented in Figure 3.4 as a function of the overpotential.

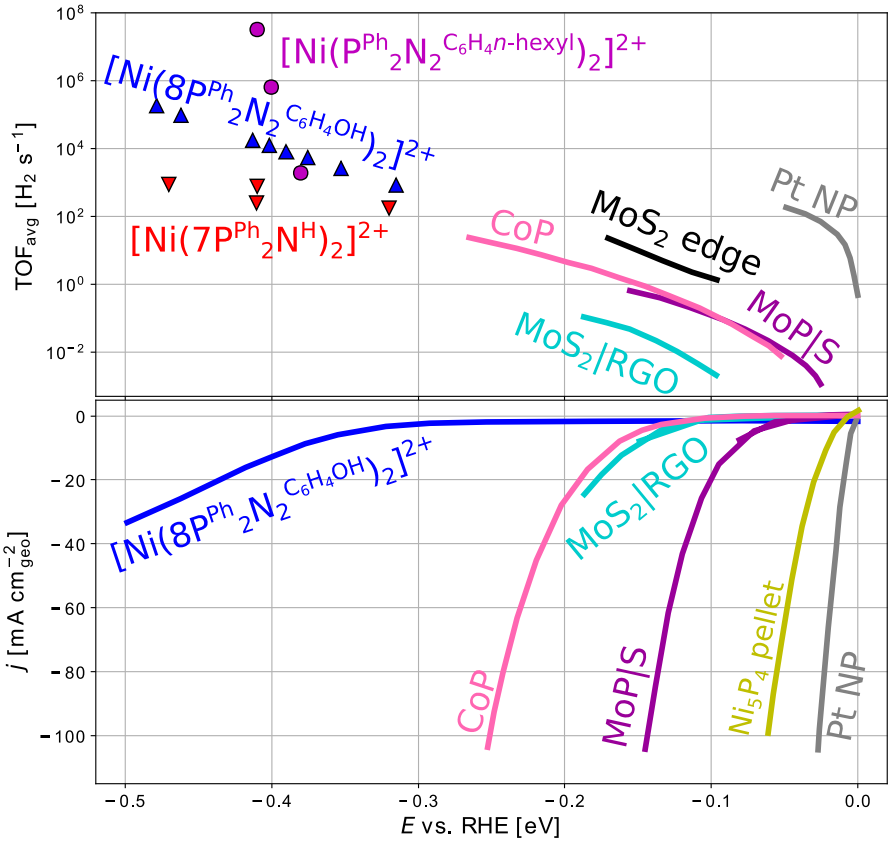

Figure 3.4 *The average turnover frequencies (*$\mathrm{TOF_{avg}}$*) and the total electrode current densities of various HER catalysts, measured with linear sweep voltammetry. The original figure is by Seh et al. [3]. The catalysts and the corresponding references are:* $\mathrm{MoS_2}$ *edges [7, 45],* $\mathrm{MoS_2}$ *nanoparticles on reduced graphene oxide nanosheets (*$\mathrm{MoS_2}$*/RGO) [7, 30, 46], CoP [45, 47], molybdenum photosulfide (MoP|S) [46, 47], platinum nanoparticles (Pt NP) [47],* $\mathrm{Ni_5P_4}$ *pellets [35], and Ni-based homogeneous catalysts [48, 49, 50].*

To illustrate the chronological trend in the HER catalyst development, Figure 3.5 shows the overpotential at -10 mA/cm^2 for various $\mathrm{MoS_2}$-based, phosphide and carbide HER catalysts as a function of publication date. The dashed line at -30 mV represents the performance of platinum, which has been reported to be between -20 and -40 mV, depending on the reference [4]. Individual catalysts in Figures 3.4 and 3.5 are described in the following subsections.

3.4.1 $\mathrm{MoS_2}$-based HER Catalysts

The HER activity of molybdenum disulfide $\mathrm{MoS_2}$ was discovered in 2005, when Hinnemann *et al.* [28] performed DFT calculations and found that at 50 % hydrogen coverage the $(\bar{1}010)$ edges of $\mathrm{MoS_2}$ have ΔG_{H^*} of 0.08 eV, which is close to the ΔG_{H^*} observed for PGMs such as platinum [7]. Their work was inspired by hydrogen-

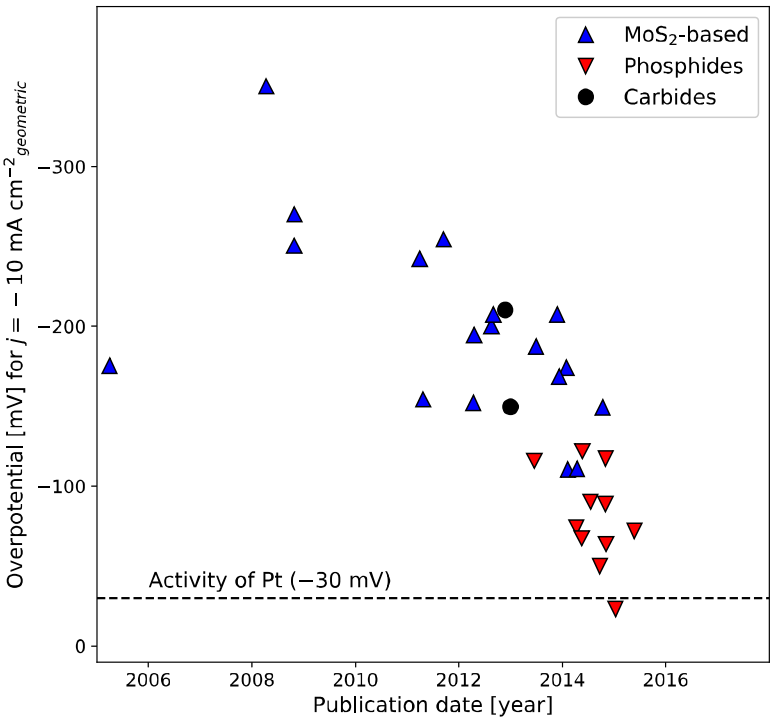

Figure 3.5 *Chronological trend in the overpotential required to reach the current density of* $-10\ mA/cm^2$ *for different HER catalysts:* MoS_2*-based, phosphides and carbides. The figure is adapted from reference [3]. The data for sulfides and phosphides is originally from references [7, 32, 33, 34, 35, 46, 47, 51, 52, 53, 54, 55], whereas data for carbides is from [4, 56]. For Pt the overpotential required to reach* $-10\ mA/cm^2$ *is between* -20 *and* $-40\ mV$*, depending on the reference [4]. The dashed reference line represents the activity of Pt and is at* $-30\ mV$*. For example Laursen et al. [35] reported that for* Ni_5P_4 *micron sized particles and bulk Pt the overpotentials required for* $-10\ mA/cm^2$ *in acid are* $-23\ mV$ *and* $-27\ mV$*, respectively.*

producing enzymes such hydrogenases and nitrogenases. Moreover, the experimental measurements by Hinnemann *et al.* for graphite supported MoS_2 nanoparticles also indicated that MoS_2 might be a reasonable earth-abundant HER catalyst [28, 34].

Jaramillo *et al.* [43] confirmed experimentally in 2007 that the HER activity of MoS_2 correlates linearly with the number of MoS_2 edge sites. They also reported that the sulfur atoms on the molybdenum edges of MoS_2 are the active sites. The basal plane of MoS_2 has ΔG_{H^*} of 1.92 eV [57] and is therefore catalytically inert [28, 43]. This explains why bulk MoS_2 crystals are poor HER catalysts [3, 57].

Since 2007 the HER performance of MoS_2 has been extensively developed by increasing the density of the active sites and achieving high edge-to-bulk ratios using various approaches [3, 4]. One method for exposing the active edge sites is by *nanostructuring* the MoS_2 [3, 7, 58]. Studies on MoS_2 *nanowires*, such as MoS_2–MoO_3

core–shell nanowires, resulted that, despite the high surface area of the nanowire morphology, they had a low density of exposed active edge sites due to the inert MoS_2 basal planes being curved around the circumference of the nanowires [7, 32]. The *double-gyroid mesoporous nanostructure* has been found to be an excellent MoS_2 HER catalyst structure [7, 58]. It contains no extended basal planes and has a high density of exposed active edge sites. A disadvantage of the double-gyroid structure is that the electron transfer paths from the active sites to the conducting substrate are long, which results in resistive losses. Lower resistive losses and a promising HER performance has been observed for MoS_2 *thin films* [7, 59].

Another attractive approach for achieving high edge-to-bulk ratio is by dispersing MoS_2 nanoparticles on supports with high surface area [3, 4]. Li *et al.* [30] reported an excellent performance for MoS_2 NPs synthesized on reduced graphene oxide (RGO) nanosheets. The MoS_2|RGO electrode was observed to have a Tafel slope of -41 mV/decade, suggesting (Eq. 3.9) that the MoS_2-catalyzed HER proceeds via the Volmer–Heyrosvky mechanism in acid solutions. The MoS_2|RGO required an overpotential of -150 mV to reach the current density of -10 mA/cm^2. Li *et al.* also reported that the RGO support significantly improved the activity compared to the free MoS_2 NPs, because MoS_2|RGO had a better NP dispersion and different NP morphology, which improved the charge transport and the active site access. In addition to nanostructured MoS_2, systems such as amorphous molybdenum sulfides and various molecular molybdenum clusters (*e.g.* Mo_4S_{13}) have also been found to exhibit high activity towards HER [7, 30].

The success of increasing the performance of MoS_2-based HER catalysts can be observed in Figure 3.5, as the overpotential required to reach the current density of -10 mA/cm^2 has decreased greatly over the last decade [3, 4, 7]. Besides their promising HER activity, the MoS_2-based catalysts are also highly stable in acidic environments [4, 7]. The electrode consisting of MoS_2 NPs on the RGO support is among the best-performing MoS_2-based electrodes and its catalytic activity is presented in Figure 3.4, along with the activity of MoS_2 edge sites only [7, 30, 43].

The performance improvements of the MoS_2-based electrodes have been achieved mostly by increasing the density of active sites (the molybdenum edges of the MoS_2) [3]. However, as the number of active sites becomes large enough, transport limitations such as charge and mass transfer start to limit the catalyst performance [3, 7]. These limitations can be overcome by improving the intrinsic activity of MoS_2 [3, 7]. This is possible by increasing the intrinsic activity of the active MoS_2 sites, or making the inactive sites active towards HER [3, 7]. Without improvements, the intrinsic activity of Pt is 10^2–10^5 times higher than the intrinsic activity of the active MoS_2

edges [7].

Various approaches have emerged to improve the intrinsic activity of MoS_2 catalysts. Transition metal dopants Fe, Co and Ni have been demonstrated to improve the intrinsic activity of MoS_2 S-edges [7, 60, 61, 62, 63, 64]. The inert basal planes can exhibit high HER activity through the formation of different defects [65, 66]. Li *et al.* [66] reported that the otherwise inactive MoS_2 basal planes show high activity when vacancies are introduced by applying strain on the MoS_2 sheets. Other approaches for improving the intrinsic activity of MoS_2 include *e.g.* modifying the hydrogen binding energy through substrate interactions, tuning the electronic properties through lithium ion intercalation, and utilizing the 1T metallic polymorph phase of MoS_2. More details on these methods and on MoS_2 catalyst development in general can be found for example in [3, 4, 7].

3.4.2 Phosphide-based HER Catalysts

The promising capabilities of MoS_2-based HER catalysts sparked a development of various different non-precious HER catalysts in the 2010s. New types of HER catalysts have been developed especially to have a higher intrinsic activity than the MoS_2-based catalysts to avoid the performance limitations caused by mass and charge transfer. The phosphide family of HER catalysts, namely the transition metal phosphides (TMPs), have emerged as viable HER catalyst candidates due to their excellent performance and stability. Notable TMPs are for example Ni_2P, Ni_5P_4, CoP, FeP, MoP, WP, and mixed metal TMPs such as $Co_xFe_{1-x}P$, all of which will be discussed below. A more detailed comparison of different TMPs can be found for example in [47].

In 2005, Liu and Rodriguez predicted computationally using DFT that the (001) plane of nickel-phosphide Ni_2P exhibits excellent HER activity [67]. Previously it was known that nickel can be used as an HER catalyst in alloys such as Ni-Mo, Ni-Mo-Zn, Ni-Fe and Ni-P, but they are not stable in acidic solutions and show significantly lower HER activity compared to PGMs such as platinum [34]. In 2013, Popczun *et al.* [34] observed the HER activity of hollow Ni_2P nanoparticles to be comparable to that of MoS_2 NPs deposited on RGO, requiring -150 mV of overpotential to reach $j = -10$ mA/cm^2 in acidic solutions. The Ni_2P NPs were tested to be stable in long-term usage and their average TOF was estimated to be 0.015 H_2 s^{-1} at $\eta = -100$ mV. The Ni_2P NPs also catalyzed HER in alkaline solutions, but they quickly degraded into Ni, resulting in a rapid HER performance decline [34]. Feng *et al.* [68] improved the hollow Ni_2P NPs by synthesizing them with simpler, safer and more scalable techniques. They observed the NPs to have an

excellent activity and a good long-term stability in both acidic and alkaline solutions, and reported an overpotential of -122 mV to reach $j = -10$ mA/cm^2 in acid.

In 2014, Laursen *et al.* [35] synthesized micron sized particles of Ni_5P_4 and found them to exhibit superior performance compared to Ni_2P in acidic and alkaline solutions. The Ni_5P_4 NP pellets also exhibited excellent stability in acid and base, as no catalyst degradation was observed in short term studies at $j = -10$ mA/cm^2. The average TOF per surface site for Ni_5P_4 in acid was estimated to be 3.5 H_2 s^{-1} for $\eta = -100$ mV, which is significantly higher compared to Ni_2P (0.015 H_2 s^{-1}), but lower compared to bulk Pt (329 H_2 s^{-1} for $\eta = -100$ mV) [35]. Nevertheless the turnover frequency of Ni_5P_4 NPs is remarkable for a PGM-free HER catalyst. In addition, the overall electrode efficiency (geometric activity) was reported to be on par with bulk Pt catalysts in strong acid: the Ni_5P_4 NPs had aTafel slope of -33 mV/decade and -23 mV of overpotential was required for $j = -10$ mA/cm^2. The excellent performance of Ni_5P_4 is seen in Figures 3.4 and 3.5, where Ni_5P_4 is the second best performing HER catalyst, not far from platinum nanoparticles in terms of the total electrode activity.

Cobalt phosphide (CoP) has been observed to exhibit high HER activity [33, 45, 47, 51, 52]. Popczun *et al.* [33] deposited CoP NPs on Ti support and found CoP|Ti electrodes to be acid-stable and exhibit higher HER activity than Ni_2P NPs under strong acidic conditions ($\eta_{-10\ \mathrm{mA/cm^2}} = -75$ mV, $\mathrm{TOF_{avg}} = 0.046$ H_2 s^{-1} at $\eta = -100$ mV). Tian *et al.* [51] fabricated self-supported nanoporous cobalt phosphide nanowire arrays on carbon cloth (CoP|CC), which catalyzed HER efficiently in acidic, neutral and basic conditions. The CoP|CC was reported to have excellent durability and performance close to that of CoP|Ti. Liu *et al.* [52] decorated carbon nanotubes (CNTs) with CoP nanocrystals. They reported CoP|CNT to catalyze HER in acidic conditions, but not as well as CoP|Ti or CoP|CC. The CoP thin films catalysts studied by Hellstern *et al.* [45] were stable in acidic environment and exhibited $\mathrm{TOF_{avg}} = 0.48$ H_2 s^{-1} at 100 mV overpotential, indicating a significantly higher intrinsic activity compared to the CoP NPs. The performance of the CoP thin films is shown in Figure 3.4. It is noteworthy that cobalt is a critical metal and it is produced largely in the Democratic Republic of the Congo [11] under unbearable worker conditions.

Iron, tungsten, and molybdenum phosphide nanoparticles (FeP, WP, and MoP) are also promising catalysts for HER. Callejas *et al.* [55] reported hollow FeP nanoparticles to exhibit high HER activity in acidic and neutral solutions. Deposited on Ti substrates, the FeP NPs required an overpotential of -50 mV for -10 mA/cm^2. FeP NPs deposited on titanium dioxide TiO_2 were reported to produce H_2 at rates and

amounts close to Pt|TiO_2. WP NPs were studied by McEnaney *et al.* [69]. They reported WP|Ti to have an excellent stability under acidic conditions and to require an overpotential of -120 mV for -10 mA/cm^2. MoP NPs have been studied by several groups and reported to have an excellent stability and activity towards HER in acidic environments [46, 54, 70, 71]. Kibsgaard *et al.* [46] improved the activity of pure MoP by introducing sulfur on its surface. Molybdenum phosphosulfide (MoP|S) required an overpotential of -86 mV for -10 mA/cm^2. Its performance is shown in Figure 3.4 [46, 47]. Kibsgaard *et al.* reported that for MoP|S there is still room for improvements and the geometric area activity could be improved by nanostructuring.

In addition to the aforementioned TMPs, various binary transition metal phosphide nanoparticles have also been developed. Hao *et al.* [53] synthesized $Co_xFe_{1-x}P$ nanocubes with different Co and Fe ratios: $x = 0.38$, 0.59, and 0.71. They found $Co_{0.59}Fe_{0.41}P$ nanocubes to have the best performance compared to the other two ratios. $Co_{0.59}Fe_{0.41}P$ nanocubes had a good stability in both acidic and alkaline conditions, and they required an overpotential of -72 mV (acid) and -92 mV (alkaline) for $j = -10$ mA/cm^2.

In 2015 Kibsgaard *et al.* [47] combined a computational, ΔG_{H^*} descriptor-based approach and an experimental approach to comprehensively study a wide range of TMP systems in acidic solutions: CoP, Co_2P, FeP, Fe_2P, $Fe_{0.25}Co_{0.75}P$, $Fe_{0.5}Co_{0.5}P$, $Fe_{0.75}Co_{0.25}P$, MoP, MoP|S, and Ni_2P. Importantly, they found that transition metal phosphides follow the HER volcano relationship, shown in Figure 3.6. Out of different TMP systems that they considered, $Fe_{0.5}Co_{0.5}P$ had its ΔG_{H^*} closest to zero, indicating that it would have the highest activity. Kibsgaard *et al.* confirmed experimentally that $Fe_{0.5}Co_{0.5}P$ does indeed have the highest intrinsic HER activity of the considered TMP systems. While previous studies on TMPs had considered the geometric current density as a metric for electrode activity, Kibsgaard *et al.* measured the electrochemically active surface area (ECSA) for each material and normalized the linear sweep voltammograms (LVSs) to ECSA, allowing them to estimate the intrinsic activity (TOF_{avg} per surface site) consistently for all the TMP systems.

According to Kibsgaard *et al.* [47], $Fe_{0.5}Co_{0.5}P$ has higher intrinsic activity than pure Ni_2P, MoP, CoP and FeP. TOF_{avg} for MoP|S is almost equal to that of $Fe_{0.5}Co_{0.5}P$. It is notable that Kibsgaard *et al.* did not include Ni_5P_4 in their study. TOF_{avg} per surface site for $Fe_{0.5}Co_{0.5}$ is approximately 0.19 H_2 s^{-1}, whereas Laursen *et al.* [35] estimated their Ni_5P_4 pellets to have TOF_{avg} of 3.5 H_2 s^{-1} per surface site. Both of these were reported for $\eta = -100$ mV and in strong acid, indicating that the intrinsic

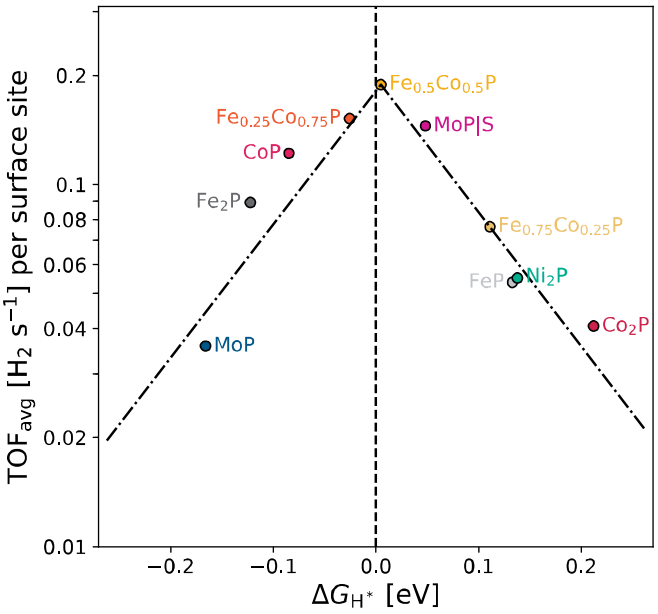

Figure 3.6 *The HER activity volcano for transition metal phosphide catalysts. The figure is adapted from [47]. Kibsgaard et al. obtained* TOF_{avg} *by normalizing linear sweep voltammograms (LVSs) to the electrochemically active surface area (ECSA).* $Fe_{0.5}Co_{0.5}P$ *has the most thermo-neutral* ΔG_{H^*} *and exhibits the highest intrinsic activity towards HER.*

activity of Ni_5P_4 would be approximately 18 times higher than that of $Fe_{0.5}Co_{0.5}P$. This would suggest that Ni_5P_4 is currently the most promising TMP HER catalyst. Kibsgaard *et al.* noted that according to their results the HER activity of TMPs might be inherently limited, preventing them from reaching Pt-level performance.

3.4.3 Other HER Catalysts

In addition to different MoS_2 and phosphide-based materials, a good activity towards HER in acidic solutions has been reported for various carbides (Mo_2C, Mo_2C|CNT) [32, 56, 72], selenides ($MoSe_2$, $CoSe_2$, WSe_2) [36, 57, 73], sulfides (CoS_2, WS_2) [73, 74], borides (MoB, α-MoB_2) [56, 75], nitrides ($NiMoN_x$|C) [37], and binary surface alloys (BiPt) [42]. Many new promising catalysts have been found through computational studies, for example Greeley *et al.* [42] performed a high-throughput computational catalyst screening for over 700 binary surface alloys using the ΔG_{H^*} descriptor-based approach. Their calculations predicted BiPt to have an HER activity comparable to that of Pt. They synthesized the BiPt alloy and the experimental studies showed improved HER performance compared with pure Pt, therefore in agreement with the computational screening results. Seh *et al.* [72] studied two-dimensional layered transition metal carbides using the ΔG_{H^*} approach and found Mo_2CT_x (T_x = H, O, OH, H_2O) to be an active and stable catalyst candidate for

HER in acid. They confirmed their prediction experimentally. The ΔG_{H^*} descriptor approach was also used by Tsai *et al.* [57] in their study of layered transition metal dichalcogenides (TMDs). TMDs have a composition of MX_2, where M is a metal and X is a chalcogen. Tsai *et al.* found that for TMDs (M = Ti, V, Nb, Ta, Mo, W, Pd and X = S, Se) the HER activity improvements are strongly limited by a decrease in stability. Recently, Chen *et al.* [75] used the ΔG_{H^*} descriptor approach combined with experimental studies and identified the α-phase molybdenum diboride (α-MoB_2) to exhibit excellent HER activity and stability in acidic solutions.

In alkaline solutions, amorphous NiMo nanoparticles are considered the state-of-the-art in efficiency [3, 35]. McKone *et al.* [76] synthesized unsupported Ni-Mo nanopowders which exhibited high activity towards HER in acidic and alkaline conditions. The nanopowders were stable in alkaline, but in acid they degraded rapidly. McKone *et al.* estimated the Ni-Mo nanopowders to have TOF_{avg} of 0.05 H_2 s^{-1} at $\eta = 100$ mV [76]. McCrory *et al.* [77] reported high geometric activities for electrodeposited NiMo, CoMo, NiMoCo, NiMoFe and NiW in acid and alkaline. They determined NiMo and NiMoCo to show similar geometric activity in acid to that of Pt, with no loss of activity after 2 hours. All materials except NiW showed good stability in 24 hour short-term stability tests. The long-term stability of NiMo was tested and was good in alkaline, but a significant decline in activity was observed in acidic solutions. This indicates that the short-term stability tests are insufficient to determine the long-term stability of an HER catalyst [77].

Nickel alloys such as NiMo NPs are stable in alkaline environments, but they degrade in acid solutions [35, 37, 76, 77, 78]. However, Chen et al. [37] synthesized NiMo nitride nanosheets on a carbon support and found that the presence of nitrogen stabilized $NiMoN_x$ nanosheets in acid. The $NiMoN_x$|C electrode exhibited an excellent HER activity and no corrosion was observed in acidic solution. This indicates that it might be possible to create cheap Ni-based electrocatalysts that are stable under acidic environment.

All HER catalysts mentioned so far are heterogeneous catalysts. Various homogeneous HER catalysts, namely different molecular complexes, have also been developed [48, 49, 50]. They are stable and exhibit superior intrinsic activity with TOF_{avg} of the order 10^2–10^7 H_2 s^{-1}. However, large overpotentials (> 350 mV) are required to reach considerable current densities, as can be seen in Figure 3.4.

4. FIRST-PRINCIPLES MODELING OF HYDROGEN EVOLVING ELECTROCATALYSTS

The rapid development in theoretical understanding of surface reactions and the computational technology has made it possible to describe catalytic reactions on surfaces with the precision required to compare with experiments [17, 23]. The density functional theory (DFT) is a widely applied computational method in computational electrocatalysis [22, 23]. Computational simulations of catalytic reactions are of great importance in the modern electrocatalysis due to several reasons. Firstly, they provide valuable information that is difficult or impossible to access using experimental techniques, *e.g.*, the adsorption energies of intermediate species. A better understanding of the atomistic mechanisms of catalytic reactions help the design and fabrication of efficient electrocatalysts [24, 79]. Secondly, computational approaches enable large-scale screening for catalyst materials [23], which can be automatized to a great extent. Potential catalyst materials may also be found that would have never been considered in experimental research.

This chapter presents various important concepts related to first-principles modeling of HER electrocatalysts and rational catalyst design. The descriptor-based screening method, Brønsted–Evans–Polanyi (BEP) relations, the *d*-band model, and active site models are discussed in the context of hydrogen evolution. In the present work, the Gibbs free energy of hydrogen adsorption (ΔG_{H^*}), which was introduced in Chapter 3, is used as a descriptor of HER activity. Therefore, a thermochemical scheme for determining the relevant hydrogen coverage and the value of ΔG_{H^*} for a given surface is presented.

4.1 Descriptor-based Approach

DFT calculations of reaction energies, reaction barriers, and the associated entropies can be used to evaluate the kinetics of a catalytic reaction [23]. The results obtained with DFT-based kinetic models agree well with experimental data in cases such as CO oxidation over ruthenium oxide at low oxygen pressures, ammonia synthesis over a ruthenium catalyst at industrial reaction conditions, and methanol decomposition

over a Pt catalyst, for example [23]. Unfortunately, evaluating the complete kinetic description of a catalytic reaction from first-principles is a demanding task, even with the state-of-the-art computing capabilities and theoretical methods. Vast spaces of potential catalyst materials cannot be efficiently screened by determining the reaction kinetics in detail for each material. This has led to the construction of predictive theories such as the *descriptor-based approach*, which tries to find the atomic scale properties that define the macroscopic kinetics [23, 79, 80, 81, 82]. This allows describing of the catalytic activity of a material as a function of a few parameters, which are called *descriptors*. The descriptor-based approach can be used either to screen a large pool of catalyst material candidates, or as a guiding principle in rational catalyst design. [79]

The identification of descriptors is based on *scaling relations*, which are linear relations that have been observed between different variables in catalytic reactions [83]. One example of a scaling relation is that the activation energies of catalytic reactions on surfaces have been observed to depend strongly on the adsorption energies of intermediate species [23]. For transition metal catalysts, Hammer and Nørskov [15] discovered the *d-band model*, which connects the density of the d electrons on the catalyst surface to how strongly the intermediate species bind. The linear scaling relations between activation energies and reaction energies are called Brønsted–Evans–Polanyi (BEP) relations [83]. The d-band model and BEP relations are discussed more in the next section.

Scaling relations are useful because they reduce the dimensionality of the rational catalyst design problem. By combining the scaling relations with a kinetic model (*micro-kinetic modeling*), catalytic activity can be mapped onto the descriptor space. This is denoted by *activity maps*, which are a generalization of, *e.g.*, the volcano relationships. An example of a volcano relationship was shown in Chapter 3 for HER (see Figures 3.3 and 3.6). Activity maps are helpful tools in catalyst design, because they rationalize the process of finding better catalyst materials with desired properties.

For HER, the Gibbs free energy of hydrogen adsorption, ΔG_{H^*}, has been used as a descriptor in a large number of computational studies [3]. The principle of the ΔG_{H^*} descriptor-based approach was already explained in Chapter 3: materials with $\Delta G_{\mathrm{H}^*} \cong 0$ exhibit higher activity towards HER, thus following the principle of Sabatier. ΔG_{H^*} has been observed to be an accurate descriptor of the HER activity on transition metal surfaces [29, 42, 44, 84] and various systems beyond pure TMs, *e.g.*, TM alloys [42], MoS_2 [28, 43, 60, 85], and TM phosphides [24, 47, 86]. The HER activity of several materials, such as MoS_2 and Ni_2P, was originally predicted

with the ΔG_{H^*} descriptor approach. In conclusion, the approach is powerful and robust in screening different types of HER catalyst materials [87].

The descriptor-based approach does not take into account all factors required to determine the absolute rate of HER [3]. Kinetic barriers, for example, change as a function of pH, which results in pH dependence of current density. The effect of pH on the rate of HER is not yet fully understood quantitatively [3]. Strmcnik *et al.* [27] reported that HER behaves differently in acid and alkaline solutions, because hydrogen is evolved from a different proton donor (H_3O^+ in acid and H_2O in alkaline). Strmcnik *et al.* suggested that a bifunctional catalyst capable of stabilizing both parts of water, *i.e.* H and OH, would be advantageous. The size of the kinetic barriers also varies between different types of materials, which is observed in Figure 3.3, where MoS_2 has lower activity compared to the PGMs, although its ΔG_{H^*} is near the optimum. The variations in *e.g.* pH or kinetics barriers shift the HER activity volcano vertically, but not horizontally. Therefore, the ΔG_{H^*} descriptor is still valid for determining active HER catalysts [3, 8].

The reaction paths can be calculated with the nudged elastic band (NEB) method. This is computationally more demanding than determining ΔG_{H^*}, but provides valuable information on the reaction mechanisms and the kinetic barriers. These are traditionally determined for selected systems, which are of particular importance and/or interest, such as platinum surfaces [44, 84], MoS_2 [85], and Ni_2P [86].

4.2 Brønsted–Evans–Polanyi Relations and the *d*-band Model

For the electrochemical processes in heterogeneous catalysis and generally in chemistry, the linear scaling relations between activation energies (barriers) E_a and reaction energies[1] $\Delta E_{reaction}$ are known as Brønsted–Evans–Polanyi (BEP) relationships [22, 44, 83]. If a chemical reaction follows a BEP relation, the activation barriers, which are tedious to compute, can be estimated using the thermochemical data [22]. Calculating the reaction energy (*i.e.* the thermochemical difference) involves only geometry optimizations of ground-state configurations, which is significantly cheaper computationally compared to finding transition states with the NEB method [88].

Skúlason *et al.* [44] studied computationally the Tafel, Heyrovsky, and Volmer mechanisms of HER on a Pt(111) electrode. They calculated the reaction activation barriers, E_a, with the NEB method and found them to depend linearly on the reaction energies, $E_{reaction}$, establishing the BEP relations for all three HER mechanisms.

[1] The energy difference between the initial and final state of a reaction. The potential energy diagram of a catalytic reaction is illustrated in Figure 2.1.

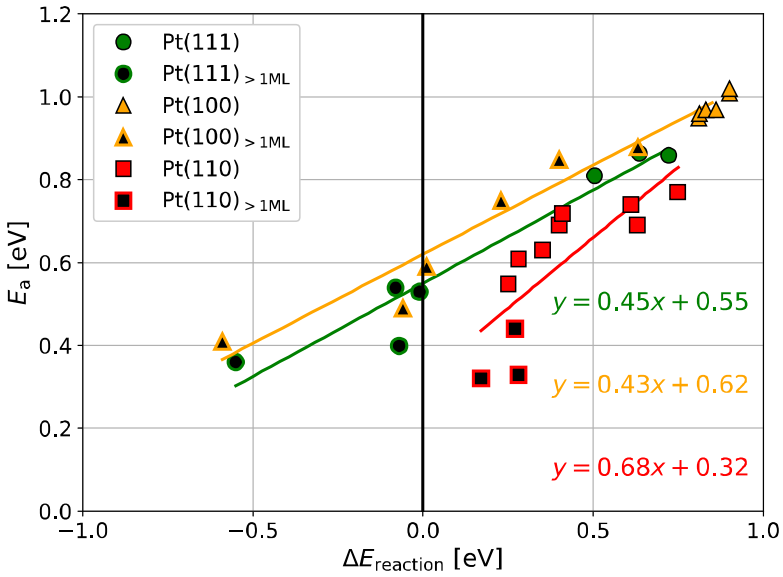

Figure 4.1 *The activation barrier E_a for HER on Pt(111), Pt(100), and Pt(110) via the Tafel reaction as a function of the reaction energy $E_{reaction}$. The energies follow the BEP relationship. The Figure is adapted from [44].*

Skúlason *et al.* [44] observed that the predominant HER mechanism on the Pt(111) electrode is the Tafel reaction, which is in agreement with the experimental observations [30, 31]. The BEP relations for the Tafel mechanism on Pt(111), Pt(100), and Pt(110) electrodes are shown in Figure 4.1, which is adapted from [44]. Skúlason *et al.* obtained the variations in E_a and $E_{reaction}$ by varying the hydrogen coverage.

In 2000, Hammer and Nørskov [15] discovered that the center of the *d*-band, denoted by ε_d, is strongly related to the energies of the intermediate states for catalytic processes on transition metal surfaces. In TM catalysis, this theory is known as the *d*-band theory and it is based on a large number of theoretical and experimental studies. The theory states that variations between adsorption energies of different TMs are largely described by the coupling between the adsorbate valence states and the *d*-states (*d* electrons) of the TM surface [23]. The theory is important in understanding the bonding of adsorbate species on TM catalysts, because according to it, the *d*-band center is a good descriptor of the adsorption bond strength of intermediate species [87]. The higher the *d*-states are in energy relative to the highest occupied state (the Fermi energy, ε_F) of the metal, the stronger the interaction with the adsorbate states [23, 83]. The *d*-band theory can be explained by the filling of the anti-bonding states that form between the *d*-states of the TM surface and the adsorbate valence states. The anti-bonding (bonding) *d*-states near ε_F can be shifted above (below) it and become empty (occupied), which increases the bond strength [23, 83]

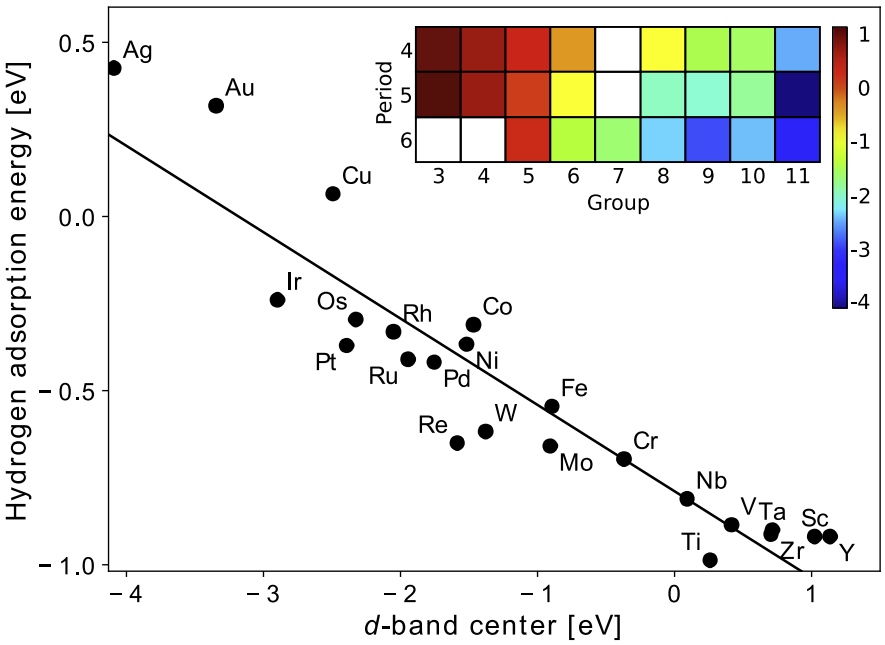

Figure 4.2 *The hydrogen adsorption energy in hollow sites of fcc and bcc lattices plotted against the d-band center of various transition metals. The inset shows the d-band center (in eV) in the periodic table. The equation of the linear fit is* $y = -0.25x - 0.79$. *The Figure is adapted from [89].*

Kristinsdóttir and Skúlason [89] studied the adsorption of hydrogen on transition metals from the 4th, 5th, and 6th periods using DFT calculations. They observed a good correlation between the *d*-band center of the metals and the hydrogen adsorption energy in hollow sites of fcc and bcc lattices, as shown in Figure 4.2. The metals with higher lying *d*-states bind hydrogen atoms more strongly, which is explained by the *d*-band model.

The BEP relations and the *d*-band theory are of great importance, because they give guidelines for rational catalyst design. The *d*-band theory is particularly interesting in the context of nanoscale TM catalysts, because theoretical understanding of tuning of their electronic structure has developed rapidly in recent years. The precise control of the composition, morphology, ionic and electronic states of NPs allows tuning of their catalytic properties. [17]

4.3 Active Site Models

In the equations describing the mechanisms of a catalytic reaction, for example the HER Equations (3.3), an active site is merely denoted by * or S. However, in molecular-level computational approaches such as DFT calculations, the location of

the adsorbate species on the surface of a catalyst has to be defined in a structure file, *e.g.*, an XYZ file. Therefore, one has to have knowledge of which surface sites are favorable for the given reaction. The binding energy of the intermediate species depends on the active site. Choosing the model for active site(s) is a crucial part of computational catalyst materials screening and it will determine the outcome of a screening study. For simple reactions, such as hydrogen evolution and ammonia synthesis, the active site models are relatively well established. For more complex reactions with multiple intermediate and product species, such as the reactions of synthesis gas (CO and H_2), the active site models are more complex and often controversial. [79]

Choosing the active site model is system dependent, and it is more straightforward if the surface of the catalyst is well-defined and simple. For complex surfaces and composite catalyst materials, the active sites are not easily and unambiguously defined. This is a major bottleneck in the reliable use of the descriptor-based computational screening approach, because it causes considerable uncertainty to the outcome. It is also questionable, how far the known active site models and the insight of the reaction mechanisms are still valid for different catalyst materials. Another issue in computational studies is that they usually do not take into account surface defects and grain boundaries, both of which affect the availability of active sites in experimental studies and in practical catalysis [27, 79]. Lattice strain, pH, and charging may also affect the active sites. [79]

Experimentally, the active sites can be investigated using *in situ* or *operando* studies [17, 79]. Most of the experimental atomic-scale catalyst characterization is obtained under ultra-high vacuum (UHV). There is still room for improvement, because the state-of-the-art experimental techniques have difficulties characterizing catalysts under the conditions at which catalytic processes actually occur without distorting the true nature of the processes [17]. The development of experimental techniques is of great importance, because detailed experimental studies allow narrowing down the possible active sites and mechanisms. Large catalyst material spaces cannot be explored and screened reliably without profound knowledge of the active sites. [79]

The active site models and reaction mechanisms have been studied for HER catalysts such as Pt(111) [44, 84], MoS_2 [28, 60, 75, 85], transition metal phosphides [24, 47, 86], and binary surface alloys [42]. For fcc(111) transition metal surfaces, *e.g.* a Pt(111) surface, the active sites are traditionally modeled by considering three types of sites; top sites, bridge sites, and hollow sites [79, 84]. An illustration of these sites by Reuter *et al.* [79] is shown in Figure 4.3(a). The fcc(111) surface atoms form triangles, whose vertices are the top sites, edges are the bridge sites,

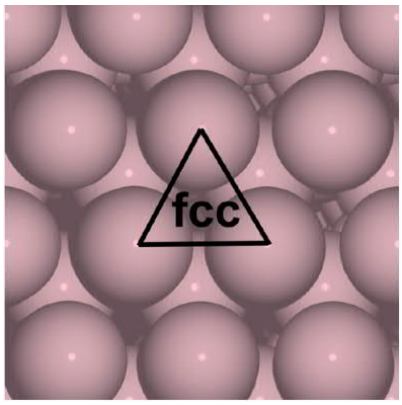

(a) Three sites of the fcc(111) surface, illustrated by a triangle: vertices/edges/center of the triangle represent the fcc(111) top/bridge/hollow sites, respectively. The Figure is adapted from [79].

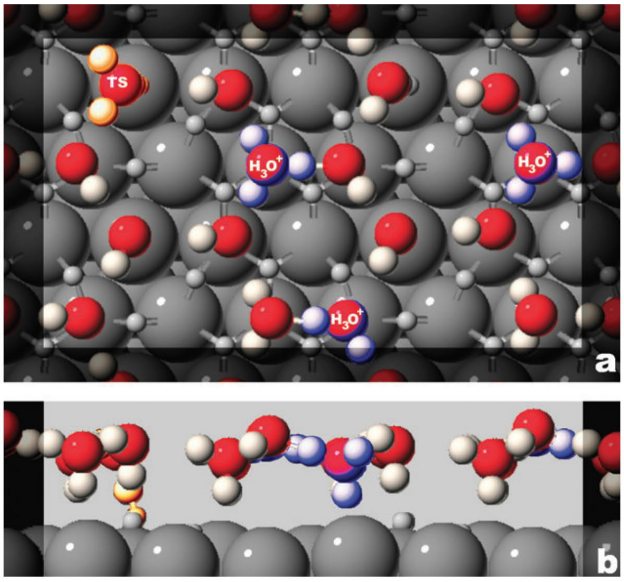

(b) Top (a) and side (b) view of the model system for Pt(111) electrode, modeled by Skúlason *et al.* [84]. The system contains hydronium ions (H_3O^+), and the adsorbed H atoms (light gray) are located in the fcc top, bridge and hollow sites.

Figure 4.3 *Two examples of active site models for transition metal surfaces.*

and at the center of each triangle is a hollow site. Another example is presented in Figure 4.3(b). It shows the hydrogen adsorption sites considered by Skúlason *et al.* [84], who studied the HER reactions mechanisms on a Pt(111) electrode. The hydrogen atoms are located in the fcc(111) top, bridge, and hollow sites.

In computational HER studies, the fraction of available adsorption sites occupied by hydrogen atoms is called the *hydrogen coverage*, denoted by θ_{H}. This is mathematically expressed as

$$\theta_{\mathrm{H}} = \frac{n_{\mathrm{H}}}{n_{\mathrm{site}}} \tag{4.1}$$

where n_{H} is the number of adsorbed hydrogen intermediates and n_{site} is the total number of active adsorption sites available on the studied catalyst surface [60].

4.4 Free Energy of Hydrogen Adsorption

In order to determine the Gibbs free energy of hydrogen adsorption, ΔG_{H^*}, for a given catalyst material, the relevant hydrogen coverage has to be found. This

coverage (the number of adsorbed hydrogen atoms) is called the *critical coverage*. It is found by minimizing the total adsorption energy (*i.e.* the integral adsorption energy):

$$\Delta G_{\mathrm{tot}}(n_{\mathrm{H}}) = G(n_{\mathrm{H}}) - G(0) - n_{\mathrm{H}}\mu \tag{4.2}$$

with respect to the number of adsorbed H atoms, n_{H} [44, 84, 86]. In Eq. (4.2), $G(n_{\mathrm{H}})$ and $G(0)$ are the free energies of a surface with n_{H} adsorbed H atoms and uncovered surface, respectively, and μ is the chemical potential of protons and electrons, given by

$$\mu = \frac{1}{2}G(\mathrm{H_2}) - q_{\mathrm{e}}U \tag{4.3}$$

where $G(\mathrm{H_2})$ is the gas phase free energy of molecular hydrogen, q_{e} is the elementary charge, and U is the cathodic potential. The coverage relevant at the chemical potential μ is the number of H atoms that minimizes Eq. (4.2). Calculating the derivative of Eq. (4.2) with respect to n_{H} yields the differential free energy

$$\Delta G_{\mathrm{diff}}(n_{\mathrm{H}}) = G(n_{\mathrm{H}}) - G(n_{\mathrm{H}} - 1) - \mu \tag{4.4}$$

The differential free energy is relevant in the analysis of HER at a given n_{H}, because when it is equal to zero, $\Delta G_{\mathrm{diff}} = 0$, the minimum of Eq. (4.2), and therefore the critical coverage, has been found. The Gibbs free energy of hydrogen adsorption, ΔG_{H^*}, is equal the differential free energy closest to zero, $\Delta G_{\mathrm{diff}} \cong 0$.

The Gibbs free energies are not obtained directly from DFT calculations, since the total energies obtained from DFT calculations are at 0 K, and they do not take into account the entropy or the zero point energy [86]. The relevant corrections can be done by using the equation

$$\Delta G = \Delta E_{\mathrm{H}} + \Delta E_{\mathrm{ZPE}} - T\Delta S_{\mathrm{H}} \tag{4.5}$$

where ΔE_{H} is the hydrogen chemisorption energy, ΔE_{ZPE} is the difference in the zero point energy between the adsorbed and the gas phase, T is the temperature and ΔS_{H} is the entropy of adsorption. The vibrational entropy in the adsorbed state is small, therefore the entropy of the adsorption of a hydrogen atom is $\Delta S_{\mathrm{H}} = -\frac{1}{2}S^{\circ}(\mathrm{H_2})$, where $-\frac{1}{2}S^{\circ}(\mathrm{H_2})$ is the gas phase entropy of $\mathrm{H_2}$ at the standard conditions [29, 86]. The entropy and ZPE correction terms have been reported to make an addition of approximately 0.24 eV to the total energy, independent of the number of adsorbed

hydrogen atoms [24, 29, 86]. Therefore, Eq. (4.5) becomes

$$\Delta G = \Delta E_{\mathrm{H}} + 0.24 \text{ eV} \tag{4.6}$$

where the hydrogen chemisorption energy, ΔE_{H}, can be obtained from DFT by

$$\Delta E_{\mathrm{H}} = E(n_{\mathrm{H}}) - E(n_{\mathrm{H}} - 1) \tag{4.7}$$

where $E(n_{\mathrm{H}})$ and $E(n_{\mathrm{H}} - 1)$ are the total energies of the ground-state structures of the system with n_{H} and $n_{\mathrm{H}} - 1$ adsorbed hydrogen atoms, respectively.

Using equations (4.3), (4.4), (4.6), and (4.7), the differential Gibbs free energy can be approximated as

$$\Delta G_{\mathrm{diff}}(n_{\mathrm{H}}) \approx E(n_{\mathrm{H}}) - E(n_{\mathrm{H}} - 1) - \frac{1}{2}E(\mathrm{H_2}) + 0.24 \text{ eV} + q_{\mathrm{e}}U \tag{4.8}$$

where $E(\mathrm{H_2})$ is the DFT total energy of a hydrogen molecule in the gas phase. For each n_{H}, the hydrogen adsorption sites should be sampled to find the ground-state structure of the hydrogen coverage. If the cathodic potential is zero, $U = 0$, Eq. (4.8) simplifies into

$$\Delta G_{\mathrm{diff}}(n_{\mathrm{H}}) \approx E(n_{\mathrm{H}}) - E(n_{\mathrm{H}} - 1) - \frac{1}{2}E(\mathrm{H_2}) + 0.24 \text{ eV} \tag{4.9}$$

Furthermore, if only one hydrogen atom is adsorbed, $n_{\mathrm{H}} = 1$, Eq. (4.9) becomes

$$\Delta G_{\mathrm{diff}}(n_{\mathrm{H}} = 1) \approx E(1) - E(0) - \frac{1}{2}E(\mathrm{H_2}) + 0.24 \text{ eV} \tag{4.10}$$

where $E(1)$ and $E(0)$ are the total energies of the surface with one adsorbed hydrogen atom and uncovered surface, respectively.

Now the differential free energy can be calculated for different hydrogen coverages using either Eq. (4.9) or (4.10). ΔG_{diff} are commonly presented as a function of either n_{H} or the hydrogen coverage, θ_{H}. As aforementioned, when ΔG_{diff} is zero, the critical coverage has been found. Because n_{H} values are discrete, in practice the critical coverage is found when ΔG_{diff} changes its sign from negative to positive. ΔG_{H^*} is then equal to the ΔG_{diff} value closest to zero.

An example of the differential free energy calculated as a function of hydrogen coverage is presented in Figure 4.4, which is by Kibsgaard *et al.* [47]. They calculated ΔG_{diff} values for various transition metal phosphides. The corresponding HER activities of these systems are presented in Figure 3.6, where the ΔG_{H^*} values are

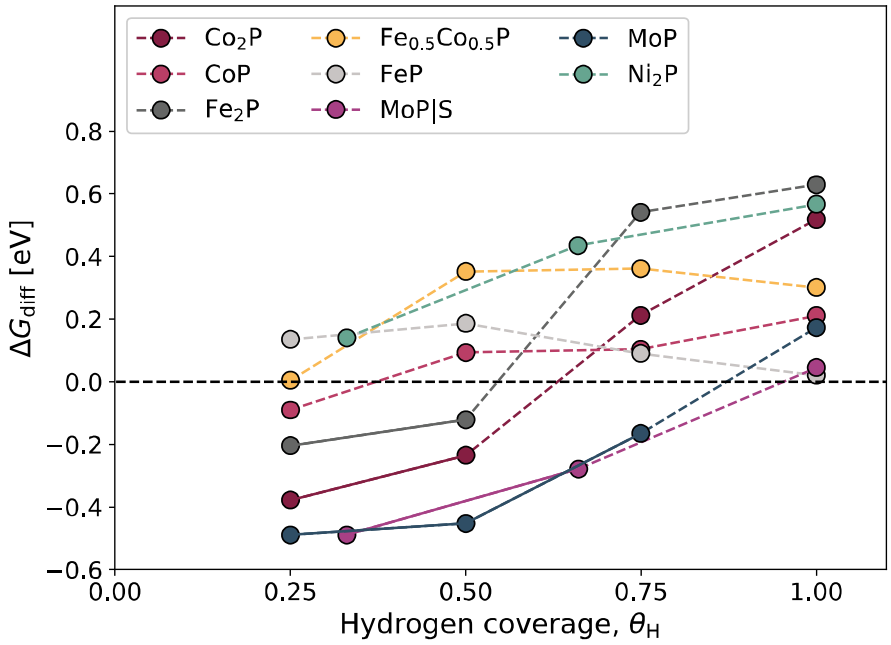

Figure 4.4 *The differential Gibbs free energy of hydrogen adsorption as a function of hydrogen coverage for various transition metal phosphides. θ_H is defined as a fraction of a monolayer with respect to the number of active sites on the surface. The Figure is adapted from [47].*

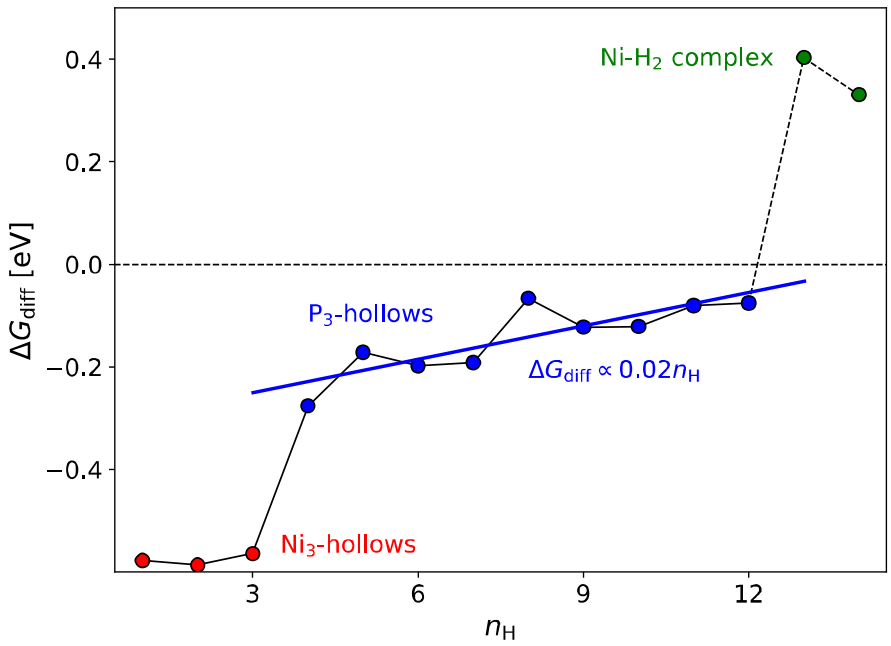

Figure 4.5 *The differential Gibbs free energy of hydrogen adsorption as a function of the number of adsorbed hydrogen atoms for Ni_5P_4 surface. The colors differentiate H binding sites. The Figure is adapted from [24].*

obtained from Figure 3.6 using the method explained above. Another example is shown in Figure 4.5, originally by Wexler *et al.* [24], who studied the hydrogen adsorption on the surface of Ni_5P_4. They emphasized different adsorption sites, such as Ni_3 and P_3 hollow sites, with different colors, because the sites were occupied at specific order. Similar examples of ΔG_{diff} plots can be found in the literature for other systems as well, such as MoS_2 in Refs. [60, 75, 85].

5. ELECTRONIC STRUCTURE THEORY AND COMPUTATIONAL METHODS

Before one can compute any interesting catalysis related properties of a material, its atomic structure has to be found. The key to finding the atomic structure and material properties is the electronic structure of the material. The electronic structure is governed by the famous Schrödinger equation and, in the end, defines all material properties. Solving the Schrödinger equation is a challenging task due to complexity of the quantum many-body problem, which is solvable only in a few simple cases, such as in the case of the hydrogen atom. Fortunately, different approximations and computational methods have been developed, allowing one to solve the electronic and atomic structures of larger and more interesting systems.

This chapter provides a brief introduction to the theory of electronic structure calculations. It presents some important concepts such as the adiabatic approximation, Born–Oppenheimer approximation, and density functional theory (DFT). All material structure calculations for this thesis were done by employing CP2K, an open-source DFT software package. The computational details are presented in the latter part of this chapter, *e.g.* the important parameters and algorithms used in the calculations. The specifications of the computing hardware are presented. Analysis methods such as the radial distribution function and Bader charge analysis are also briefly discussed.

5.1 Quantum Many-body Problem

The structure of a piece of matter (*e.g.* a solid or a molecule) can be modelled as a set of atomic nuclei and electrons interacting via electrostatic forces. The particles may also be under the influence of an external field (*e.g.* an electric field). In principle all the properties can be derived by solving the time-independent Schrödinger equation (SE) [90] for this many-body system

$$\hat{\mathcal{H}}\psi_n(\boldsymbol{R},\boldsymbol{r}) = \mathcal{E}_n\psi_n(\boldsymbol{R},\boldsymbol{r}). \tag{5.1}$$

This is an eigenvalue equation where $\hat{\mathcal{H}}$ is the Hamiltonian operator and state of the system is denoted by n. $\mathcal{E}_n$ are the total (electron-nuclear) energy eigenvalues and $\psi_n(\boldsymbol{R}, \boldsymbol{r})$ are the corresponding eigenstates of the whole system (the total electron-nuclear wave functions). Spatial coordinates of the electrons are denoted by $\boldsymbol{r}$ and nuclear coordinates by $\boldsymbol{R}$. [91, pp. 4–5]

The Hamiltonian for the many-body system in the operator form is

$$\hat{\mathcal{H}} = \hat{T}_\mathrm{n} + \hat{T}_\mathrm{e} + \hat{V}_\mathrm{nn} + \hat{U}_\mathrm{ee} + \hat{V}_\mathrm{ne} \tag{5.2}$$

where $\hat{T}_\mathrm{n}$ and $\hat{T}_\mathrm{e}$ are the kinetic energy operators for the nuclei and the electrons respectively, $\hat{V}_\mathrm{nn}$ is the nucleus-nucleus interaction, $\hat{U}_\mathrm{ee}$ is the electron-electron interaction and $\hat{V}_\mathrm{ne}$ is electron-nucleus interaction. The interaction terms represent the electrostatic interactions between the particles. For the sake of simplicity we assume an idealized situation without external fields. [91, pp. 4–5]

For a system with N electrons and P nuclei, the general form of the Hamiltonian is

$$\begin{aligned}\hat{\mathcal{H}} = &-\sum_{I=1}^{P} \frac{\hbar^2}{2M_I}\nabla_I^2 - \sum_{i=1}^{N} \frac{\hbar^2}{2m_\mathrm{e}}\nabla_i^2 + \frac{1}{2}\frac{e^2}{4\pi\varepsilon_0}\sum_{I=1}^{P}\sum_{J\neq I}^{P}\frac{Z_I Z_J}{|\boldsymbol{R}_I - \boldsymbol{R}_J|} \\ &+ \frac{1}{2}\frac{e^2}{4\pi\varepsilon_0}\sum_{i=1}^{N}\sum_{j\neq i}^{N}\frac{1}{|\boldsymbol{r}_i - \boldsymbol{r}_j|} - \frac{e^2}{4\pi\varepsilon_0}\sum_{I=1}^{P}\sum_{i=1}^{N}\frac{Z_I}{|\boldsymbol{R}_I - \boldsymbol{r}_i|}\end{aligned} \tag{5.3}$$

where the lower case letters $\boldsymbol{r}$, i and j are related to the electrons and upper case letters $\boldsymbol{R}$, I and J are related to the nuclei. $\boldsymbol{R}_I$ $(I = 1, 2, \ldots, P)$ are the nuclear spatial coordinates and $\boldsymbol{r}_i$ $(i = 1, 2, \ldots, N)$ are the electronic spatial coordinates. Z_I,Z_J and M_I are the atomic numbers and masses of the nuclei, m_e is the electron mass, e is the elementary charge, $\hbar$ is the Planck constant, and ε_0 is the vacuum permittivity. [91, pp. 4–5][92]

The two-body nature of electrostatic interactions means that separation of variables cannot be applied to the Schrödinger equation (5.1). The many-body SE can be solved analytically only in a few very simple cases (*e.g.* hydrogen atom and H_2^+ molecule). Exact numerical solutions are also limited to small systems such as atoms and very small molecules. Therefore, several approximations have to be applied in order to be able to solve the electronic structure of more complicated systems. [91, p. 5]

5.2 Adiabatic Approximation

The first approximation is the *adiabatic approximation*, which is an assumption that the electrons do not undergo transitions between stationary states, *i.e.* they remain always in the same stationary state of the electronic Hamiltonian. The electrons can be thought of as instantaneously following the motion of nuclei. The validity of this approximation raises from the fact that the nuclei are significantly heavier than the electrons (electron and proton mass ratio is approximately 1:1836) and therefore the nuclei are much more sluggish than the electrons. [91, pp. 6–10][92]

The adiabatic approximation suggests to separate the degrees of freedom connected with the motion of the nuclei from those of the electrons. The total (time-dependent) wave function of a system can be reduced to

$$\Psi(\boldsymbol{R}, \boldsymbol{r}, t) = \Theta_n(\boldsymbol{R}, t)\Phi_n(\boldsymbol{R}, \boldsymbol{r}) \tag{5.4}$$

where $\Psi(\boldsymbol{R}, \boldsymbol{r}, t)$ is the total *time-dependent* wave function of the system, t denotes time, $\Theta_n(\boldsymbol{R}, t)$ are wave functions describing the evolution of the nuclear sub-system in each one of the *adiabatic electronic eigenstates* $\Phi_n(\boldsymbol{R}, \boldsymbol{r})$. The dynamics of the atomic nuclei and the electrons are therefore separated and their wave functions decoupled. The state n can be the ground-state or an excited state. [91, pp. 6–10]

The electronic wave function satisfies the time-independent Schrödinger equation

$$\hat{h}_{\mathrm{e}}\Phi_n(\boldsymbol{R}, \boldsymbol{r}) = E_n(\boldsymbol{R})\Phi_n(\boldsymbol{R}, \boldsymbol{r}) \tag{5.5}$$

where

$$\hat{h}_{\mathrm{e}} = \hat{T}_{\mathrm{e}} + \hat{U}_{\mathrm{ee}} + \hat{V}_{\mathrm{ne}} = \hat{\mathcal{H}} - \hat{T}_{\mathrm{n}} - \hat{V}_{\mathrm{nn}} \tag{5.6}$$

is the electronic Hamiltonian and $E_n(\boldsymbol{R})$ are the electronic total energies (eigenvalues) corresponding to the electronic eigenstates $\Phi_n(\boldsymbol{R}, \boldsymbol{r})$. [91, p. 8]

The time-dependent adiabatic Schrödinger equation for the nuclear wave functions $\Theta_m(\boldsymbol{R}, t)$ is

$$i\hbar\frac{\partial\Theta_m(\boldsymbol{R}, t)}{\partial t} = \left(-\sum_{I=1}^{P}\frac{\hbar^2}{2M_I}\nabla_I^2 + \tilde{E}_n(\boldsymbol{R})\right)\Theta_m(\boldsymbol{R}, t) \tag{5.7}$$

where

$$\tilde{E}_n(\boldsymbol{R}) = E_n(\boldsymbol{R}) + \sum_{I=1}^{P} \frac{\hbar^2}{2M_I} \left\langle \Phi_q \left| \nabla_I^2 \right| \Phi_q \right\rangle . \tag{5.8}$$

The second term in Eq. (5.8), noted by the Dirac bracket notation, is a diagonal correction to the electronic energy levels due to the dependence of the electronic wave function on the nuclear coordinates. [91, p. 11]

5.3 Classical Nuclei Approximation

The many-body problem can be simplified further by using the fact that in practise the correction term in Eq. (5.8) is negligible (usually < 0.5 %). Neglecting this term is called the *Born–Oppenheimer approximation*[1] [93], which proposes that *the atomic nuclei can be treated as classical particles* which move according to the frozen potential energy surface of the system. This approximation is valid in most cases. [91, p. 11][92]

To formulate equation of motion for the nuclei, Ehrenfest's theorem [91, pp. 12] can be applied to first obtain the dynamics of the position and momentum operators

$$i\hbar \frac{\mathrm{d}\left\langle \boldsymbol{R} \right\rangle}{\mathrm{d}t} = \left\langle \left[\hat{\mathcal{H}}, \boldsymbol{R} \right] \right\rangle = i\hbar \frac{\left\langle \boldsymbol{P} \right\rangle}{M} \Longrightarrow M \frac{\mathrm{d}\left\langle \boldsymbol{R} \right\rangle}{\mathrm{d}t} = \left\langle \boldsymbol{P} \right\rangle \tag{5.9}$$

$$i\hbar \frac{\mathrm{d}\left\langle \boldsymbol{P} \right\rangle}{\mathrm{d}t} = \left\langle \left[\hat{\mathcal{H}}, \boldsymbol{P} \right] \right\rangle = -i\hbar \left\langle \nabla E_n(\boldsymbol{R}) \right\rangle \tag{5.10}$$

Ehrenfest's theorem thus clarifies that classical mechanics deals with the average values (*i.e.* expectation values) and quantum mechanics with the underlying details. [94, pp. 31–32]

Combined these two equations result in the Newtonian equation of motion for the nuclei

$$M \frac{\mathrm{d}^2\left\langle \boldsymbol{R} \right\rangle}{\mathrm{d}t^2} = - \left\langle \nabla E_n(\boldsymbol{R}) \right\rangle \tag{5.11}$$

In classical nuclei approximation we identify mean values as Cartesian coordinates of the classical particles: $\boldsymbol{R}_{\mathrm{cl}}(t) = \langle \boldsymbol{R} \rangle$ and $\nabla E_n(\boldsymbol{R}_{\mathrm{cl}}) = \langle \nabla E_n(\boldsymbol{R}) \rangle$. The equation

[1] To avoid misconception: the approximation is called adiabatic when the $\tilde{E}_n$ includes the correction term and Born–Oppenheimer approximation when the correction term is neglected. These two approximation names are commonly used quite unclearly.

of motion becomes

$$M\frac{\mathrm{d}^2\boldsymbol{R}_{\mathrm{cl}}}{\mathrm{d}t^2} = -\nabla E_n(\boldsymbol{R}_{\mathrm{cl}}) \tag{5.12}$$

where $\nabla E_n(\boldsymbol{R}_{\mathrm{cl}})$ is th nth adiabatic potential energy surface (PES). Each different PES has one corresponding equation of motion. [91, p. 12]

To determine the force acting on a nucleus, $\boldsymbol{F}_I$, one can apply the Hellmann–Feynman theorem [91, pp. 12-13][95] which yields

$$\begin{aligned}\boldsymbol{F}_I = M_I\frac{\mathrm{d}^2\boldsymbol{R}_I(t)}{\mathrm{d}t^2} &= -\nabla E_n(\boldsymbol{R}_I) \\ &= -\left\langle \Phi_n(\boldsymbol{R}) \left| \frac{\partial \hat{h}_{\mathrm{e}}(\boldsymbol{R},\boldsymbol{r})}{\partial \boldsymbol{R}_I} \right| \Phi_n(\boldsymbol{R}) \right\rangle - \frac{\partial V_{\mathrm{nn}}(\boldsymbol{R})}{\partial \boldsymbol{R}_I}\end{aligned} \tag{5.13}$$

where

$$\begin{aligned}\hat{h}_{\mathrm{e}}(\boldsymbol{R},\boldsymbol{r}) = &-\sum_{i=1}^{N}\frac{\hbar^2}{2m_{\mathrm{e}}}\nabla_i^2 + \frac{1}{2}\frac{e^2}{4\pi\varepsilon_0}\sum_{i=1}^{N}\sum_{j\neq i}^{N}\frac{1}{|\boldsymbol{r}_i-\boldsymbol{r}_j|} \\ &- \frac{e^2}{4\pi\varepsilon_0}\sum_{I=1}^{P}\sum_{i=1}^{N}\frac{Z_I}{|\boldsymbol{R}_I-\boldsymbol{r}_i|}\end{aligned} \tag{5.14}$$

and

$$V_{\mathrm{nn}}(\boldsymbol{R}) = \frac{1}{2}\frac{e^2}{4\pi\varepsilon_0}\sum_{I=1}^{P}\sum_{J\neq I}^{P}\frac{Z_I Z_J}{|\boldsymbol{R}_I-\boldsymbol{R}_J|} \tag{5.15}$$

Solving Eq. (5.13) in the stationary case; $-\nabla E_n(\boldsymbol{R}_I) = 0$ (*i.e.* relaxing the forces acting on the nuclei) is known as *geometry optimization*. Integrating Equation (5.13) numerically is called first-principles (or *ab initio*) molecular dynamics, where $E_n(\boldsymbol{R}_I)$ is the first-principles potential. In both cases, molecular dynamics and geometry optimization, analyzing the structure of matter comes down to solving the time-independent electronic Schrödinger equation (5.5). This is known as electronic structure calculation. The second term in Eq. (5.14) containing the interactions between the electrons makes this problem a difficult task. [91, pp. 13]

There are multiple approaches to calculate the electronic structure numerically. The traditional approaches are Hartree–Fock (HF) approximation and density functional theory (DFT). Hartree–Fock theory is a wave function based method, which attempts to calculate the full N-electron wave function, expressed as a Slater determinant and constructed from a set of N single-electron wave functions. DFT also

considers single-electron functions, but instead of calculating the full multi-electron wave function, it attempts to calculate the overall electronic density distribution and the total electronic energy. In recent decades, DFT has become increasingly popular method in the field of modern computational material science, and it is also the method of choice in the present work. The next section is a brief summary of the fundamentals of the density functional theory. [91, pp. 13][96, pp. 126–127]

5.4 Density Functional Theory

Density functional theory is a popular and practical scheme for numerically solving the electronic Schrödinger equation (5.5). DFT attempts to overcome the complexity of wave function based methods, such as the Hartree–Fock approximation, by utilizing the electron density distribution, $\rho(\boldsymbol{r})$, and its connection to the total electronic energy. Since the late 1980s, DFT has become one of the most popular simulation tools in computational material science. State-of-the-art parallel computing resources allow one to use DFT simulations to study molecular systems, such as nanoclusters, consisting of several hundred atoms. [92][96, pp. 126–127]

Density functional theory is applied here to solve the electronic Schrödinger equation (5.5). The eigenvalues (electronic states) E_n define different potential energy surfaces. The most interesting of the electronic states is the ground state, which has the lowest energy and is the most stable. The ground state (many-electron wave function) is denoted by Φ_0, and the corresponding ground state energy (eigenvalue) by E_0. As a reminder, the electronic Schrödinger equation is

$$\hat{h}_\mathrm{e}\Phi_n(\boldsymbol{R},\boldsymbol{r}) = E_n(\boldsymbol{R})\Phi_n(\boldsymbol{R},\boldsymbol{r}). \tag{5.16}$$

The many-electron wave function depends parametrically on nuclear coordinates $\boldsymbol{R}$ because the electronic state is solved for fixed nuclear (*i.e.* atomic) positions. The electronic Hamiltonian $\hat{h}_\mathrm{e}$ is already presented in Eq. (5.14).

The definition of electron density is[2]

$$\rho(\boldsymbol{r}) = \sum_{i=1}^{N} |\phi_i(\boldsymbol{r})|^2 \tag{5.17}$$

where N is the number of electrons and ϕ_i are the single-electron wave functions. The electrons are assumed to be *non-interacting*, thus an i^th electron can be treated

[2]Each state n has corresponding electron density. For simplicity, the state denoting n is dropped from now on.

as a point charge in the effective field of all the other electrons. This simplifies the many-electron problem to many one-electron problems[3]. The total wave function of such non-interacting N electron system can be described by an antisymmetric wave function, expressed as a Slater determinant [97]:

$$\Psi_0(\boldsymbol{r}_1, \boldsymbol{r}_2, \cdots, \boldsymbol{r}_\mathrm{N}) = \frac{1}{\sqrt{N!}} \begin{vmatrix} \phi_1(\boldsymbol{r}_1) & \phi_2(\boldsymbol{r}_1) & \cdots & \phi_\mathrm{N}(\boldsymbol{r}_1) \\ \phi_1(\boldsymbol{r}_2) & \phi_2(\boldsymbol{r}_2) & \cdots & \phi_\mathrm{N}(\boldsymbol{r}_2) \\ \vdots & \vdots & \ddots & \vdots \\ \phi_1(\boldsymbol{r}_\mathrm{N}) & \phi_2(\boldsymbol{r}_\mathrm{N}) & \cdots & \phi_\mathrm{N}(\boldsymbol{r}_\mathrm{N}) \end{vmatrix} \tag{5.18}$$

where $\phi_\mathrm{i}(\boldsymbol{r}_\mathrm{j})$ refers to the i^{th} eigenfunction of a single-electron Hamiltonian equation, positioned at the coordinate of $\boldsymbol{r}_\mathrm{j}$. It is important to note that the true many-body wave function is not a single Slater determinant, but this will be taken into account later in context of exchange-correlation functionals.

The possible spin dependency is ignored here to keep this DFT introduction simple. This leads to electron density

$$\rho(\boldsymbol{r}) = 2 \sum_{i=1}^{N_\mathrm{s}} |\phi_i(\boldsymbol{r})|^2 \tag{5.19}$$

where $N_\mathrm{s} = N/2$ is the number of doubly occupied orbitals. The factor 2 raises from the fact that occupation number of each orbital is 2 (*i.e.* one orbital can be occupied by two electrons). If electron spin was taken into account, the electron density would be a sum of two independent densities representing spin up and down states: $\rho(\boldsymbol{r}) = \rho_\uparrow(\boldsymbol{r}) + \rho_\downarrow(\boldsymbol{r})$. The derived equations would be very similar to the spin-independent equations presented in the following subsections. [91, pp. 60–61]

5.4.1 Hohenberg–Kohn Theorems

Hohenberg and Kohn formulated two important theorems in 1964 [91, pp. 56–59]. The proofs of these theorems are left outside the scope of this thesis, but the actual theorems are as follows:

Theorem 1 *The external potential v_ext, acting on electrons, is unambiguously determined by the electron density $\rho(\boldsymbol{r})$, besides a trivial additive constant [98]. The external potential v_ext includes the interaction between the electrons and the nuclei,*

[3]It is important to note that the density defined by Eq. (5.17) is not the density of the original *interacting* many-body system. However, it can be shown that the ground state electron density of the non-interacting system coincides with that of the interacting system. This inspection is left outside this thesis, but a curious reader can check reference [91, pp. 59–63] for more details.

and any other external field, such as an electric field.

The consequence of this theorem is that since $\rho(\boldsymbol{r})$ determines the external potential, it also determines the ground state wave function $\Phi_0(\boldsymbol{R}, \boldsymbol{r})$, which would be obtained by solving the full many-body Schrödinger equation, (5.16). Practically this theorem states that the electron density is all that is needed to obtain the total ground state energy. Therefore, $\rho(\boldsymbol{r})$ is in a very important role and using it reduces dimensionality of the N electron many-body problem from $3N$ to 3, because $\rho(\boldsymbol{r})$ depends only on the three spatial coordinates.

Theorem 2 *The electronic energy, E_n, is a functional*[4] *of the electron density [99]:*

$$E_n = E_n[\rho(\boldsymbol{r})] \tag{5.20}$$

The electron density that minimizes this functional is the true ground-state electron density, $\rho_0(\boldsymbol{r})$:

$$E_0[\rho_0(\boldsymbol{r})] < E[\rho(\boldsymbol{r})] \tag{5.21}$$

Figures 5.1 and 5.2 illustrate the Hohenberg–Kohn theorems 1 and 2. The electron density contains all the information, and it is more attractive choice than the wave functions (many-body approach) due to reduced dimensionality. Figure 5.2 represents Hohenberg–Kohn theorem 2; one simply needs to minimize the energy functional $E_n[\rho(\boldsymbol{r})]$ (*i.e.* "move down" on the energy surface) until the ground state density, $\rho_0(\boldsymbol{r})$, is reached.

The energy functional, Eq. (5.20), consists of the kinetic energy of *non-interacting* electrons T_0, the external potential energy V_{ext}, the classical Coulomb potential V_{H} (electrons interacting with the electron density, also called Hartree potential), and the exchange-correlation energy E_{xc}. Therefore, the complete form of the functional, also called the Kohn–Sham (KS) functional, is

$$E_n[\rho(\boldsymbol{r})] = T_0 + V_{\text{ext}} + V_{\text{H}} + E_{\text{xc}} \tag{5.22}$$

[4] A functional is a function of a function, for example an integral: $F[f] = \int_{-1}^{1} f(x)\mathrm{d}x$.

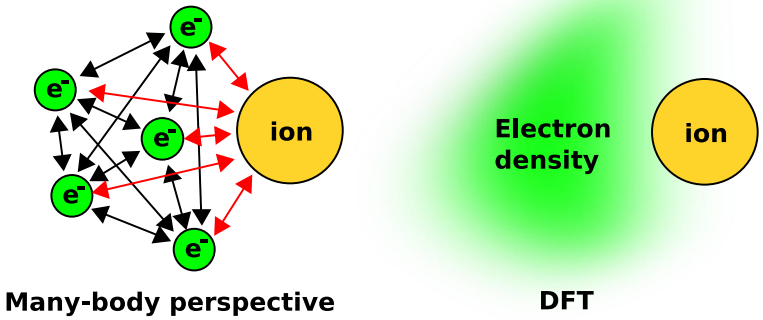

Figure 5.1 *Illustration of two different approaches to the electronic structure problem: many-body wave function based method, and density functional theory approach, where electron density is used to determine the state of the system.*

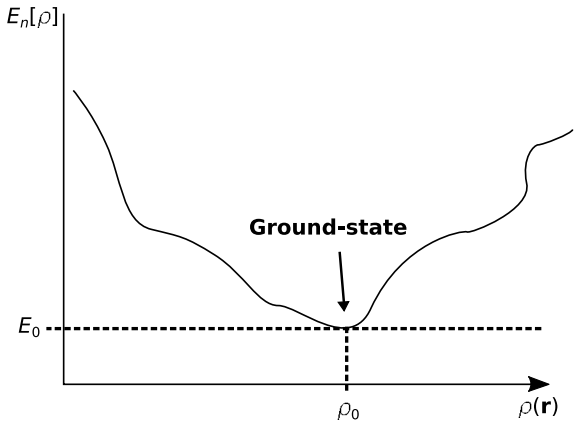

Figure 5.2 *Hohenberg–Kohn theorem 2: electronic energy is a functional of electron density, and the ground-state density $\rho_0(\boldsymbol{r})$ determines the ground-state energy E_0.*

where the first three terms are known:

$$T_0 = -\sum_i^N \int \frac{\hbar^2}{m_\mathrm{e}} \phi_i^*(\boldsymbol{r}) \nabla^2 \phi_i(\boldsymbol{r}) \mathrm{d}^3\boldsymbol{r} \tag{5.23}$$

$$V_\mathrm{ext} = \int \rho(\boldsymbol{r}) v_\mathrm{ext}(\boldsymbol{r}) \mathrm{d}^3\boldsymbol{r} \tag{5.24}$$

$$V_\mathrm{H} = \frac{1}{2} \iint \frac{e^2}{4\pi\varepsilon_0} \frac{\rho(\boldsymbol{r})\rho(\boldsymbol{r'})}{|\boldsymbol{r} - \boldsymbol{r'}|} \mathrm{d}^3\boldsymbol{r} \mathrm{d}^3\boldsymbol{r'} \tag{5.25}$$

but the exact form of the exchange-correlation energy is unknown:

$$E_{\mathrm{xc}} = E_{\mathrm{xc}}[\rho(\boldsymbol{r})] = ?$$

$E_{\mathrm{xc}}[\rho(\boldsymbol{r})]$ takes into account all quantum mechanical interactions between the electrons; not only does it account for contributions due to exchange and correlation, but also a contribution due to the difference between the true kinetic energy of the system and T_0. This difference exists because the true wave function of the system is not a Slater determinant, and therefore there is a correlation contribution to the kinetic energy that is not taken into account in T_0. Many different approximations to the E_{xc} have been developed. The choice of the exchange-correlation functional is the key to the success of the density functional approach and will be discussed later in this chapter. [92]

5.4.2 Kohn–Sham Equations

The Hohenberg–Kohn theorem 2 can be applied to find the electronic ground-state density. The Kohn–Sham functional, Eq. (5.22), has to be minimized with respect to $\rho(\boldsymbol{r})$. This variational problem can be solved by applying the Lagrangian method of undetermined multipliers. The KS functional is minimized respect to the density under the constraint that the density integrates to N particles [99]. Applying this variational principle on Eq. (5.22) and using the rules of functional derivation yields the single-electron *Kohn–Sham equation*:

$$\left[-\frac{\hbar^2}{2m_{\mathrm{e}}}\nabla^2 + v_{\mathrm{ext}}(\boldsymbol{r}) + \int \frac{e^2}{4\pi\varepsilon_0}\frac{\rho(\boldsymbol{r}')}{|\boldsymbol{r}-\boldsymbol{r}'|}\mathrm{d}^3\boldsymbol{r}' + v_{\mathrm{xc}}(\boldsymbol{r})\right]\phi_i(\boldsymbol{r}) = \varepsilon_i\phi_i(\boldsymbol{r}) \tag{5.26}$$

whose eigenfunctions are the Kohn–Sham orbitals (states) $\phi_i(r)$. Kohn–Sham equation is a single-electron Schrödinger equation; inside the square brackets is the single-electron Hamiltonian, and ε_i are the single-electron eigenvalues. $v_{\mathrm{xc}}(\boldsymbol{r})$ is the exchange-correlation potential, related to the exchange-correlation functional by:

$$v_{\mathrm{xc}}\left[\rho(\boldsymbol{r})\right] = \frac{\delta E_{\mathrm{xc}}\left[\rho(\boldsymbol{r})\right]}{\delta\rho(\boldsymbol{r})} \tag{5.27}$$

where $\delta\rho(\boldsymbol{r})$ is the variation of electron density.

Importantly, equations (5.26) and (5.27) together with the definition of electron

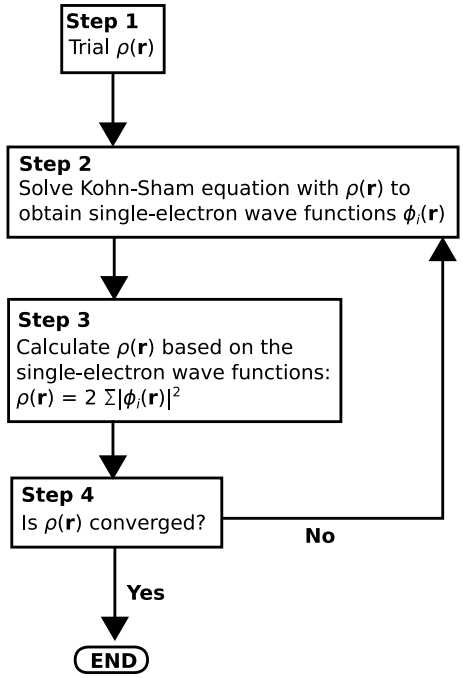

Figure 5.3 *A flow-chart of a DFT calculation with the self-consistent Kohn–Sham scheme.*

density (Eq. (5.19))

$$\rho(\boldsymbol{r}) = 2\sum_{i=1}^{N_\mathrm{s}} |\phi_i(\boldsymbol{r})|^2 \tag{5.28}$$

are the *self-consistent Kohn–Sham equations*. They can be solved with a self-consistent scheme, illustrated in the Figure 5.3. First an initial guess of the Kohn–Sham orbitals is made, and the electron density is calculated from Eq. (5.28). A new set of orbitals is calculated by substituting electron density into Eq. (5.26). These steps are repeated until convergence is reached, *i.e.* the difference in density between two subsequent iterations becomes small enough. This means that the true ground state density is found, and so is the ground state energy, which can be calculated from the Kohn–Sham functional, Eq. (5.22).

After the electronic ground state is obtained, forces on atoms can be easily calculated using previously derived equation of motion for nuclei, Eq. (5.13). As aforementioned, one can use the equation to, for example, relax forces acting on atoms (geometry optimization), run *ab initio* molecular dynamics, or calculate vibrational properties. If the positions of the nuclei change, the ground state electronic structure has to be found again using the self-consistent Kohn–Sham scheme.

In geometry optimization the ionic ground state (relaxed structure) can be calculated

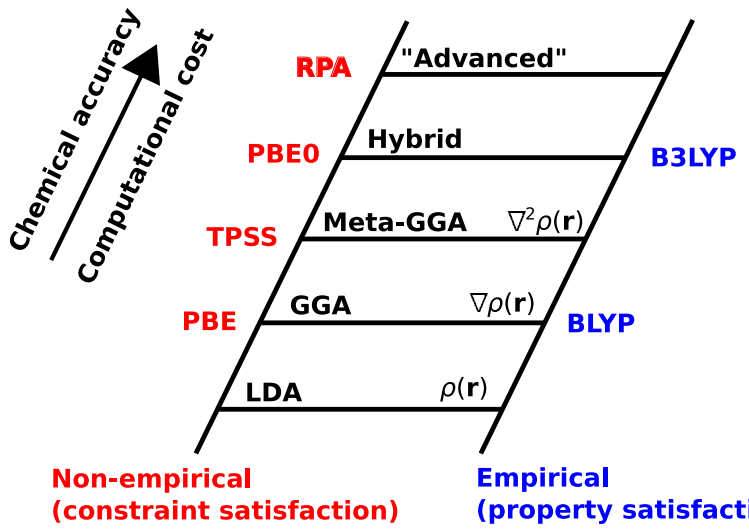

Figure 5.4 *Jacob's ladder of DFT approximations for the exchange-correlation functionals. Names of several functionals are shown. Some functionals require fitting to empirical data to determine their parameters. Climbing up the ladder results in higher chemical accuracy, but the computational cost is increased with increasing complexity. [22, 92, 100, 101]*

using the gradient descent algorithm; every iteration step the electronic ground state is calculated, then the atomic forces. Lastly, each atom is nudged on the direction of the force affecting that atom.

5.4.3 Approximations of the Exchange-correlation Energy

As mentioned above, the exact form of the exchange-correlation functional, E_{xc}, is not known. Several different approximations of E_{xc} have been developed since the introduction of DFT, and the choice of this functional is the bread and butter of density functional theory. The optimal choice of E_{xc} depends on the simulated system and the physical properties of interest. J. P. Perdew described the approximations of exchange-correlation as *Jacob's ladder* [100, 101], illustrated in Figure 5.4. Climbing up the ladder leads to better DFT results with added computational cost. The two simplest functionals are introduced here in a general level; local density approximation and generalized gradient approximation.

Local density approximation (LDA) was proposed by Kohn and Sham in 1965. It is the simplest E_{xc} functional, at the bottom of Jacob's ladder. LDA considers the electronic system as locally homogeneous rather than inhomogeneous, because the exchange-correlation for homogeneous electron gas is known to an excellent accuracy.

The LDA form of exchange-correlation is

$$E_{\mathrm{xc}}^{\mathrm{LDA}} = \int \rho(\boldsymbol{r}) \epsilon_{\mathrm{xc}}^{\mathrm{LDA}} [\rho(\boldsymbol{r})] \, \mathrm{d}^3\boldsymbol{r} \tag{5.29}$$

where $\epsilon_{\mathrm{xc}}^{\mathrm{LDA}} [\rho(\boldsymbol{r})]$ is the average exchange-correlation energy per particle in the homogeneous electron gas. Spin-considering version of LDA is called local spin density approximation (LSDA). [91, pp. 77–79][92]

The LDA (and LSDA) can provide good results for many systems, especially if the electron density is pretty uniform and slowly varying, such as in bulk metals [91, p. 82]. LDA tends to underestimate bond distances and lattice constants, and it erroneously overestimates the atomization energies [102].

A straightforward approach to address the issue of inhomogeneous electron density is to take into account (higher) derivatives of ρ. The next step in Jacob's ladder after LDA is the generalized gradient approximation (GGA), which takes into account the gradient of electron density, $\nabla\rho$. The general form of $E_{\mathrm{xc}}^{\mathrm{GGA}}$ is

$$E_{\mathrm{xc}}^{\mathrm{GGA}} = \int \rho(\boldsymbol{r}) \epsilon_{\mathrm{xc}}^{\mathrm{GGA}} [\rho(\boldsymbol{r}), \nabla\rho] \, \mathrm{d}^3\boldsymbol{r} \tag{5.30}$$

In contrast to LDA, GGA functionals may improve the accuracy of calculated atomization energies of molecules [103]. One of the most popular functionals is the Perdew–Burke–Ernzerhof (PBE) functional [103]. It is a GGA functional whose parameters can be determined without fitting to experimental data, *i.e.* PBE is a non-empirical functional. PBE has been successfully applied to a wide range of systems, and it is the functional of choice in the DFT simulations of this thesis.

The higher steps in Jacob's ladder include, for example, meta-GGA functionals and hybrid functionals. They are not discussed in detail here.

5.4.4 Gaussian and Plane Waves Method (GPW) and Pseudopotentials

In the present work, all calculations were performed by employing the CP2K program, which is a parallelized open source DFT software package, written in the Fortran 2003 programming language [18]. It is based on the Gaussian and plane waves method (GPW), which uses two representations for the electron density, namely a dual basis of atom centered Gaussian-type orbitals (GTOs) and plane waves. GTOs are primarily used to describe the wave functions, allowing compact representation

of wave functions compared to plane wave representations. This is beneficial in terms of memory and algorithm efficiency. Plane waves basis set is used to represent the electron density [18, 104]. This can allow the electrostatic energy term to be computed efficiently using the Fast Fourier Transform (FFT) algorithm.

In the GTO basis set the electron density is

$$\rho(\boldsymbol{r}) = \sum_{\mu v} P_{\mu v} \varphi_{\mu}^{*}(\boldsymbol{r}) \varphi_{v}^{*}(\boldsymbol{r}) \tag{5.31}$$

where $P_{\mu v}$ is the element of the density matrix and each orbital

$$\varphi_{\mu}(\boldsymbol{r}) = \sum_{i} d_{i\mu} g_i(\boldsymbol{r}) \tag{5.32}$$

is expressed by primitive Gaussian functions $g_i(\boldsymbol{r})$ and corresponding coefficients $d_{i\mu}$ [92]. The electron density in the plane wave basis set, denoted by $\tilde{\rho}$, is

$$\tilde{\rho}(\boldsymbol{r}) = \frac{1}{\Omega} \sum_{\boldsymbol{G}} \tilde{\rho}(\boldsymbol{G}) \exp(i\boldsymbol{G} \cdot \boldsymbol{r}) \tag{5.33}$$

where Ω is the volume of the unit cell, $\boldsymbol{G}$ are the reciprocal lattice vectors, and $\tilde{\rho}(\boldsymbol{G})$ are the expansion coefficients. Expressing the Hartree potential energy in the reciprocal space as

$$V_{\mathrm{H}}(\boldsymbol{G}) = 2\pi\Omega \sum_{\boldsymbol{G}} \frac{e^2 \tilde{\rho}^{*}(\boldsymbol{G}) \tilde{\rho}(\boldsymbol{G})}{4\pi\varepsilon_0 |\boldsymbol{G}|^2} \tag{5.34}$$

allows evaluation of the electron-electron interaction term efficiently using the FFT algorithm. [92]

Chemical bonding and other characteristics of materials are mainly characterized by valence electrons (outer shell electrons). The core electrons (non-valence electrons) are thus less important, and it is sufficient to take only the valence electrons accurately into account. We can replace the complicated effects of the motion of the core electrons with an effective potential known as the *pseudopotential*. The pseudopotential is similar to the actual potential outside the core region, which is defined by a cutoff radius. This is illustrated in Figure 5.5.

The core electrons are approximated to be frozen, and pseudopotentials replace the electron density from core electrons with a smooth density. Using pseudopotentials is beneficial in terms of computational cost, but it decreases the accuracy compared to all-electron wave function calculations. CP2K provides a library of Goedecker–

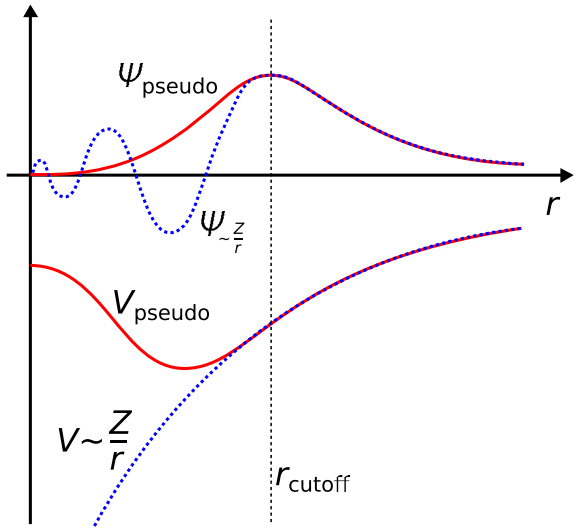

Figure 5.5 *Illustration of the pseudopotential. The effects caused by core electrons of atoms are simplified by replacing the actual potential (blue dashed line) with the pseudopotential (red solid line), which results in smooth behavior inside a cutoff radius* r_{cutoff}.

Teter–Hutter (GTH) [105] type pseudopotentials for different elements. [92]

5.5 Computational Details

The geometrical optimization of clusters in the gas phase and on alumina support were performed using DFT. All DFT calculations were carried out with the CP2K program, which uses the Gaussian and plane wave (GPW) basis sets to represent the electron density and the Kohn–Sham orbitals. The spin-polarized generalized gradient approximation with the functional form by Perdew–Burke–Ernzerhof (PBE) [103] was used to describe the exchange-correlation interaction. A molecularly optimized double-ζ valence plus polarization (DZVP) basis set was used for the Gaussian expansion of the wave functions [106]. The shorter range variants of the pseudopotentials by Goedecker, Teter, and Hutter (GTH) [105] were applied to describe the interaction between valence electrons and ions. Van der Waals corrections were taken into account with the pair potential density functional of Grimme's DFT-D3 method with zero damping [107, 108, 109]. The Kohn–Sham matrix diagonalization method was used, because it was observed to improve the convergence of calculations compared to the orbital transformation (OT) method. The Fermi–Dirac smearing method with the electronic temperature of 300 K was applied to improve convergence. All calculations were spin-polarized.

The Al_2O_3 support was modeled by a four-layer γ-phase alumina slab and a vacuum layer of 24 Å above the slab. Each layer consisted of 48 Al and 72 O atoms, therefore

the slab consisted of 480 atoms in total. The two lower layers of the slab were fixed during the geometry optimization calculations. The simulation box size was $22.33 \times 25.19 \times 30.44$ Å in the calculations with the Al_2O_3 support and $25 \times 25 \times 25$ Å in the gas phase calculations. Periodic boundary conditions were applied. In all calculations there was at least 5 Å of vacuum between the simulation box boundary and the cluster, with or without the hydrogen coverage. Therefore, the interactions among the cluster and its images were negligible.

The values of important CP2K calculation parameters are collected in Table 5.1. A 600 Ry kinetic energy cutoff was used for the plane-wave basis set. The cutoff of the reference grid was 60 Ry. The relaxation of atomic positions was carried out using the Broyden–Fletcher–Goldfarb–Shanno algorithm (BFGS) until the force on any atom was less than $9.75 \cdot 10^{-5}$ Ha/Bohr (gas phase) or $9.75 \cdot 10^{-4}$ Ha/Bohr (on alumina).

Table 5.1 *The CP2K calculation parameters. Various parameters were different in the gas phase and slab calculations, e.g. the force criteria were looser for the slab calculations due to the higher number of atoms in the system.*

Keyword	**Value (gas phase)**	**Value (on alumina)**
CUTOFF	600 Ry	600 Ry
REL_CUTOFF	60 Ry	60 Ry
EPS_SCF	$1.0 \cdot 10^{-6}$ Ha	$1.0 \cdot 10^{-6}$ Ha
MAX_FORCE	$9.75 \cdot 10^{-5}$ Ha/Bohr	$4.5 \cdot 10^{-4}$ Ha/Bohr
RMS_FORCE	$5.0 \cdot 10^{-5}$ Ha/Bohr	$5.0 \cdot 10^{-4}$ Ha/Bohr
ELECTRONIC_TEMPERATURE	300 K	300 K
ADDED_MOS	50	200

The electronic structure calculations in the present work were computed in the Sisu supercomputer provided by the IT Center for Science (CSC) [110]. Sisu is a Cray XC40 supercomputer and currently the most powerful supercomputer in Finland with its theoretical peak performance of 1688 TFlop/s [111]. It has 1688 compute nodes, each of which has two 12 core Intel Xeon E5-2690v3 (Haswell) 2.6 GHz CPUs, summing up to 40512 cores in total. Each node has 64 GB of memory (2.67 GB per core). The gas phase and support calculations were carried out by using 4 and 8 nodes, *i.e.* 96 and 192 cores, respectively.

5.6 Analysis Methods

Various methods were applied to analyze the relaxed structures, energies and electron densities obtained from the DFT simulations. The fundamentals of these meth-

ods are presented briefly in the following subsections, whereas the results are discussed in Chapters 6 and 7.

5.6.1 Excess Energy and Adsorption Energy

The *excess energy*, E_{exc}, measures the relative stability of an alloy configuration with respect to its parent compounds. In the present work, the relative stability of Pt_nNi_{55-n} clusters is calculated with respect to the ground-state Ni_{55} and Pt_{55} configurations. The excess energy per atom is

$$E_{\text{exc}} = \frac{E_{\text{tot}}^{Pt_nNi_{55-n}} - \frac{n}{55}E_{\text{tot}}^{Pt_{55}} - \frac{55-n}{55}E_{\text{tot}}^{Ni_{55}}}{55} \tag{5.35}$$

where $E_{\text{tot}}^{Pt_nNi_{55-n}}$, $E_{\text{tot}}^{Pt_{55}}$, and $E_{\text{tot}}^{Ni_{55}}$ are the total energies of the Pt_nNi_{55-n}, Pt_{55}, and Ni_{55} systems, respectively, and n is the number of Pt atoms. The excess energy of Pt_{55} and Ni_{55} is zero by definition. A negative (positive) E_{exc} value indicates that the alloy is energetically favorable (unfavorable). [12]

When a cluster is adsorbed on a support, its adsorption energy is calculated as

$$E_{\text{ads}} = E_{\text{cluster}} + E_{\text{support}} - E_{\text{cluster/support}} \tag{5.36}$$

where E_{cluster} is the total energy of the cluster in the gas phase, E_{support} is the total energy of the support (the four-layer alumina slab in this work), and $E_{\text{cluster/support}}$ is the total energy of the system where the cluster is adsorbed on the surface of the support. The higher the adsorption energy, the more favorable the adsorption of the cluster.

5.6.2 Radial Distribution Function

The bond lengths between atoms of different elements can be studied by calculating the *radial distribution function* (RDF), also known as the *pair correlation function* [112]. The Fourier transform of RDF yields the structure factor $S(\boldsymbol{Q})$, which can be determined experimentally using X-ray diffraction (XRD). Based on this relation, one can make comparisons with experimental powder XRD measurements [96, 112].

RDF is calculated separately for each pair of elements. RDF for elements A and B, denoted by $g_{\text{AB}}(r)$, describes how the density of A atoms varies as a function of distance r from atoms of a reference element B, with respect to the average density

of A atoms:

$$g_{\mathrm{AB}}(r) = \frac{\rho_{AB}(r)}{\rho_A} \tag{5.37}$$

where $\rho_{AB}(r)$ is the density of A atoms at a distance r to B atoms, and ρ_A is the average density of A atoms in the whole system.

In practise, the atoms of element B are set as the origin one after the other. The space around each B atom is radially divided into N_r bins, which are spherical shells with thickness Δr. The bins go to up to a cutoff radius r_{max}, which should be large enough so that the whole structure is included, but less than half of the length of the simulation box edge. The bins are indexed by an integer $i = 0, \ldots, N_r - 1$ with radial values $r_1, \ldots, r_{max}$. The number of A atoms is counted inside each bin i, *i.e.* between the distances r_i and $r_i + \Delta r$, for all atoms of type B. When Δr is small, this is approximately equal to counting the number of A atoms at a distance r from B atoms. Mathematically this can be expressed as

$$N_A(r_i) = \sum_{j}^{N_A} \sum_{k}^{N_B} \delta_{r_i, r_{j,k}} \tag{5.38}$$

where N_{A} and N_{B} are the total number of A and B atoms in the whole system, $r_{j,k}$ is the distance between jth A atom and kth B atom, and $\delta_{r_i, r_{j,k}}$ is the Kronecker delta, which is equal to 1 when atom A is the ith bin, *i.e.* inside the spherical shell, and otherwise it is zero.

When the spherical shells are thin enough, the volume of the shell at the distance r_i is approximately

$$V_\delta(r_i) \approx 4\pi r_i^2 \Delta r \tag{5.39}$$

The average number of A atoms at the distance r_i from the atoms of type B is obtained by dividing $N_A(i)$ by N_{B}, which divided by the volume $V_\delta(r_i)$ yields the average number density of A atoms at the distance r_i from the atoms of type B:

$$\rho_{AB}(r_i) = \frac{N_A(r_i)/N_B}{V_\delta(r_i)} = \frac{N_A(r_i)}{4\pi r_i^2 \Delta r N_B} \tag{5.40}$$

Now the radial distribution function can be obtained as

$$g_{\mathrm{AB}}(r_i) = \frac{\rho_{AB}(r_i)}{\rho_A} = \frac{\frac{N_A(r_i)}{4\pi r_i^2 \Delta r N_B}}{\frac{N_A}{V}} = \frac{V}{4\pi r_i^2 \Delta r N_B N_A} \sum_{j}^{N_A} \sum_{k}^{N_B} \delta_{r_i, r_{j,k}} \tag{5.41}$$

where V is the total volume of the system. The division term before the sums is also known as the normalization factor. [113, p. 205].

5.6.3 Bader Charge Analysis

To understand the chemical properties of a nanocluster, it is important to analyze the charge localisation and the charge transfer between atoms. DFT only suggests trends in the electronic charge transfer, but does not directly provide partial atomic charges. Various methods, *e.g.* the Mulliken population analysis and Bader charge analysis, have been developed to estimate the atomic charges from the electron density $n(\boldsymbol{r})$ [96]. In the present work, Bader charge analysis method was applied to evaluate the spatial atomic charge decomposition [114].

In Bader analysis, the volume space for each atom is determined by the zero-flux surfaces in the electron density $n(\boldsymbol{r})$. The charge of an atom, also called the *Bader charge*, is then calculated as the sum of electron and atomic core density within the atomic volume space [92, 114]. In this work the Bader charges were calculated with the Bader analysis algorithm [115], whose practical implementation is provided in the program written by Arnaldsson *et al.* [116]. The program calculates the charge associated with each atom according to the Bader partitioning.

For a cluster adsorbed on a surface (support), the charge transfer CT can be calculated by

$$CT = Q_{\text{cluster/support}} - Q_{\text{cluster}} \tag{5.42}$$

where $Q_{\text{cluster/support}}$ is the charge of the adsorbed cluster and Q_{cluster} is the charge of the cluster in the gas phase. The net charge of the cluster is the sum of the atomic partial charges. In this work, a positive (negative) Bader charge indicates the depletion (accumulation) of electronic charge, Therefore, if the free cluster has larger Bader charge than the adsorbed cluster ($CT < 0$), the electrons have been transferred from the surface to the cluster, and *vice versa*.

For the adsorption of n_{H} hydrogen atoms, the charge transfer is calculated as

$$CT_{\text{gas phase}} = Q_{\text{cluster}+n_{\text{H}}\text{H}} - Q_{\text{cluster}} - Q_{n_{\text{H}}\text{H}} \tag{5.43}$$

$$CT_{\text{supported}} = Q_{(\text{cluster}+n_{\text{H}}\text{H})/\text{support}} - Q_{\text{cluster/support}} - Q_{n_{\text{H}}\text{H}} \tag{5.44}$$

where $CT_{\text{gas phase}}$ and $CT_{\text{supported}}$ refer to the charge transfer in the gas phase and with the support. $Q_{\text{cluster}+n_{\text{H}}\text{H}}$, $Q_{(\text{cluster}+n_{\text{H}}\text{H})/\text{support}}$, and $Q_{n_{\text{H}}\text{H}}$ are the charge of the cluster with the H coverage, the charge of the supported cluster with the H coverage, and the charge of the H coverage, respectively.

6. STRUCTURAL AND ELECTRONIC PROPERTIES OF BIMETALLIC 55-ATOM PT-NI NANOCLUSTERS

The present work aims to predict the HER activity of bimetallic platinum-nickel nanoclusters. The results of the computational study are divided into two chapters. The structural and electronic properties of bimetallic Pt_nNi_{55-n} nanoclusters, namely $Pt_{12}Ni_{43}$ and $Pt_{20}Ni_{35}$, are presented in this chapter, whereas the hydrogen adsorption on the $Pt_{12}Ni_{43}$ and $Pt_{20}Ni_{35}$ clusters is presented in Chapter 7.

Two platinum-poor clusters were chosen for the study: $Pt_{12}Ni_{43}$ and $Pt_{20}Ni_{35}$. The structural properties, electronic structures and other properties of similar 55-atom Pt-Ni alloy clusters have been studied before by Guedes-Sobrinho *et al.* [12]. Before studying the hydrogen adsorption on the clusters, some results found in the literature were reproduced, such as the most stable Ni_{55} and Pt_{55} structures [117], and the excess energies for Pt_nNi_{55-n} systems [12]. This chapter starts by discussing these reproduced results. After a profound understanding of the Pt_nNi_{55-n} systems has been established, $Pt_{12}Ni_{43}$ and $Pt_{20}Ni_{35}$ clusters are aligned on the Al_2O_3 support. The adsorption energies, charge transfer, and bond lengths of the adsorption are examined.

6.1 Ni_{55} and Pt_{55} Clusters

Metal particles of different sizes and with different elements, number of atoms, and morphology can be obtained by using various synthesis techniques. The thermodynamic stability of a cluster depends on the aforementioned properties. Particles of certain sizes have higher rate of occurrence in mass spectra experiments. Such particles are known as *magic size particles* and they exhibit higher thermodynamic stability than other particles. 55 is a particularly interesting *magic number*[1], because various 55-atom transition metal nanoparticles (*e.g.* Ti_{55}, Co_{55}, Ni_{55}, and Cu_{55}) exhibit relatively high energetic stability, which is due to formation of the

[1]The number of atoms in a magic size particle.

closed-shell Mackay 55-atom icosahedron structure. [12, 117]

The ground-state structure for bulk nickel is the face-centered cubic (fcc) structure with the lattice constant of 3.52 Å and the average weighted bond length of 2.49 Å [12, 117, 118]. In the gas phase the ground-state structure of Ni_{55} cluster is known to be icosahedral with I_h symmetry [12, 117, 119, 120]. In the present work, the ground-state Ni_{55} structure reported by Piotrowski *et al.* [117] was relaxed in the gas phase. The relaxed cluster is shown[2] in Figure 6.1(a). The positions of the ions changed negligibly during the relaxation. Ni_{55} icosahedron (ICO) structure has one atom in the center, 12 other atoms in the first (inner) shell and the remaining 42 atoms in the second (outer) shell. The cluster core consists of 13 atoms and has the shape of the Ni_{13} icosahedron, which is a magic cluster and has been reported as the ground-state structure for Ni_{13} [120, 121], although Chaves *et al.* [122] recently reported polyhedral Ni_{13} to be 23 mV lower in energy compared to the icosahedral Ni_{13}. Ni_{55} has a high surface to volume ratio, because the 42 outer shell atoms, which comprise 76 % of the cluster, are located on the surface and exposed to the vacuum region. The cluster has 12 corner atoms and 20 facets, which are all identical, (111)-like and consist of 6 atoms each [117].

The radial distribution function was calculated for Ni-Ni atom pairs to analyze the bond lengths and structure of Ni_{55} ICO. RDF calculated with $\Delta r = 0.01$ Å is shown in Figure 6.1(b). All RDF peaks are sharp, which indicates that the structure is ordered. The first peak at 2.44 Å is prevalent, whereas the next three peaks are at 3.48 Å, 4.11 Å, and 4.73 Å. Due to the other peaks being at longer distances, the first peak describes the average bond length between nickel atoms. Its value (2.44 Å) agrees with the results by Piotrowski *et al.* [117]. who studied the structure of Ni_{55} computationally and reported an average bond length of 2.44 Å. The last peak in RDF is at 9.26 Å, which is the diameter of the rather spherical cluster.

Bulk nickel is ferromagnetic with the total magnetic moment per atom $m_T = 0.62\ \mu_B$ [12, 117, 118]. The Ni_{55} cluster is also reported to be highly magnetic, with the total magnetic moment of 40 μ_B (0.73 μ_B per atom) [117, 120]. Experimentally m_T has been measured to be 0.92 μ_B [120]. In the present work the total magnetic moment of Ni_{55} is zero, because for simplicity the default value for multiplicity[3] was used in all CP2K calculations. This was tested to have no effect on structure or hydrogen adsorption of bimetallic Pt-Ni clusters.

[2] In all figures, green color refers to nickel (Ni), silver to platinum (Pt), red to oxygen (O), gray to aluminium (Al), and white to hydrogen (H).

[3] Multiplicity is two times the total spin plus one. In CP2K the default value for multiplicity is 1 for an even number and 2 for an odd number of electrons.

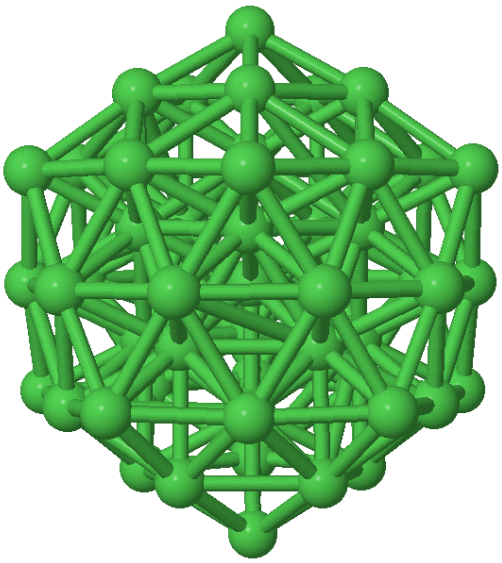

(a) The icosahedral ground-state structure of Ni_{55} cluster.

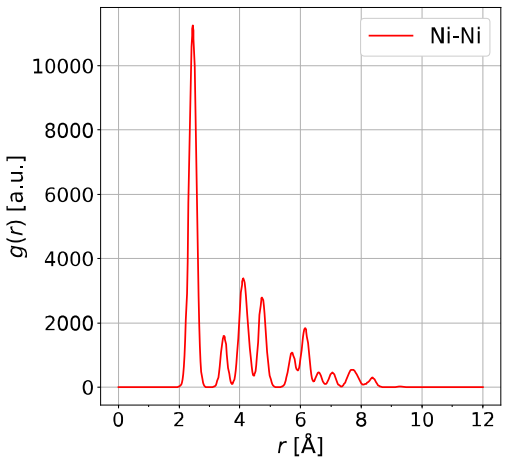

(b) The radial distribution function (arbitrary units) for the ground-state Ni_{55} cluster. Calculated with bin size $\Delta r = 0.01$ Å.

Figure 6.1 *The ground-state structure of Ni_{55} and the corresponding radial distribution function.*

The ground-state structure for bulk platinum is the face-centered cubic (fcc) structure with the lattice constant of 3.98 Å, the average weighted bond length of 2.81 Å, and zero total magnetic moment per atom [12, 118]. The most stable Pt_{55} cluster is not icosahedral, but the disordered reduced-core (DRC) structure [117, 123]. Similarly to Ni_{55} cluster, the ground-state Pt_{55} structure provided by Piotrowski *et al.* [117] was relaxed in the gas phase. The relaxed cluster is shown in Figure 6.2(a) and as in the case of Ni_{55}, the structure differs negligibly from the Pt_{55} structure by Piotrowski *et al.* [117]. The Pt_{55} DRC structure has 9 atoms located in the core and 46 atoms in the surface. In the present work, the DRC structure was found to be energetically 4.44 eV lower than the icosahedral Pt_{55}. The difference is less than the 5.64 eV reported in the literature [12, 117], nevertheless the DRC structure is more stable than the icosahedral structure. The total magnetic moment of DRC Pt_{55} is zero, in agreement with the results by Piotrowski *et al.* [117].

Similarly to Ni_{55}, the radial distribution function was calculated for Pt_{55} to analyze the bond lengths and the structure of the cluster. RDF calculated with $\Delta r = 0.01$ Å is shown in Figure 6.2(b). As in the case of Ni_{55}, the first peak at 2.67 Å is sharp and prevalent. This is in agreement with Piotrowski *et al.* [117], who reported an average bond length of 2.68 Å for Pt_{55} DRC structure. The second peak is broad and at 3.72 Å, whereas the third and fourth peaks are sharper at 4.55 Å and 5.21 Å, respectively. In contrast to Ni_{55}, the peaks in Pt_{55} RDF are not as sharp and

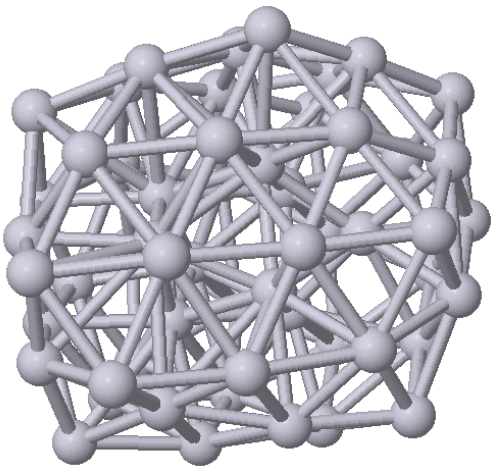

(a) The ground-state structure of Pt_{55} cluster is the disordered reduced-core (DRC) structure. DRC structure is 4.44 eV lower in energy compared to the icosahedral Pt_{55} structure.

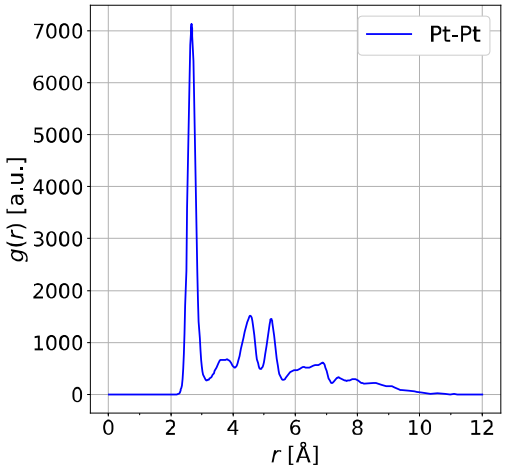

(b) The radial distribution function (arbitrary units) for the ground-state Pt_{55} cluster. Calculated with bin size $\Delta r = 0.01$ Å.

Figure 6.2 *The ground-state structure of Pt_{55} and the corresponding radial distribution function.*

recognizable as they are in Ni_{55} RDF, and Pt_{55} RDF is non-zero at all distances 3–10 Å. This indicates that Pt_{55} is not as ordered as Ni_{55}, which is a result of the disordered core of Pt_{55} cluster. Pt_{55} cluster is not spherical, but its maximum diameter is 11.2 Å, although the last bump in RDF is very small and difficult to see in Figure 6.2(b).

To study the electronic structures of Ni_{55} and Pt_{55} clusters, projected density of states (PDOS) for the s, p, and d orbitals are plotted in Figures 6.3 and Figures 6.4 for Ni_{55} and Pt_{55}, respectively. The Fermi level is set as zero in both figures and represented by the dashed line. The clusters are metallic, because there is no band gap at the Fermi energy. The Pt_{55} cluster has noticeably wider *d*-band compared to the Ni_{55} cluster.

6.2 Bimetallic Pt-Ni Nanoclusters

The 55-atom Pt-Ni nanoclusters have been previously studied in the gas phase by Guedes-Sobrinho *et al.* [12], who reported the electronic, structural and magnetic properties of Pt_nNi_{55-n} clusters for n = 6, 13, 20, 28, 35, 42, and 49. The most stable structures of all Pt_nNi_{55-n} systems were reported to be icosahedral and close to the ground-state Ni_{55} structure, except $Pt_{49}Ni_6$ was reported to have the ground-state configuration similar to Pt_{55}. Guedes-Sobrinho *et al.* used the excess energy,

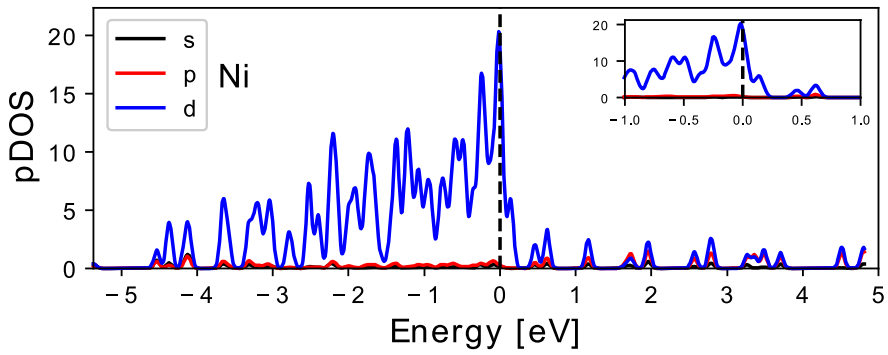

Figure 6.3 *The projected density of states (PDOS) of the ground-state Ni_{55} cluster in the gas phase, shown in Figure 6.1(a). The PDOS values were smoothed with Gaussian functions with $\sigma = 0.0367$ eV. The Fermi level is set as zero and represented by the dashed line.*

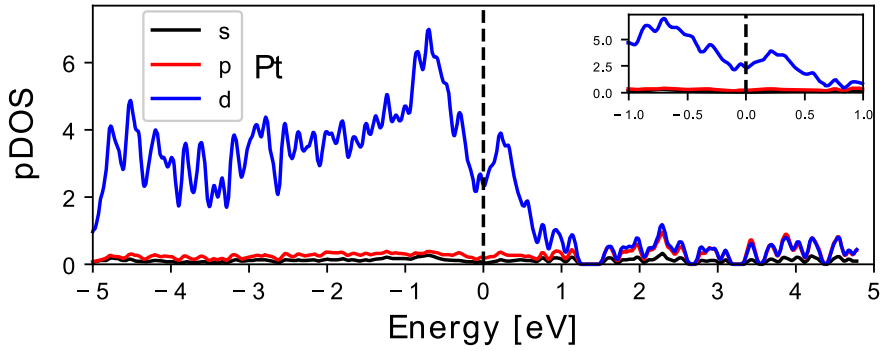

Figure 6.4 *The projected density of states (PDOS) of the ground-state Pt_{55} cluster in the gas phase, shown in Figure 6.2(a). The PDOS values were smoothed with Gaussian functions with $\sigma = 0.0367$ eV. The Fermi level is set as zero and represented by the dashed line.*

(5.35), to compare the stability of different Pt-Ni compositions. Their results are shown in Figure 6.5(a).

Here, the excess energies were calculated for the ground-state configurations of Pt_6Ni_{49}, $Pt_{13}Ni_{42}$, $Pt_{20}Ni_{35}$, $Pt_{28}Ni_{27}$, $Pt_{35}Ni_{20}$, and $Pt_{42}Ni_{13}$ reported by by Guedes-Sobrinho *et al.* [12]. In addition, a $Pt_{12}Ni_{43}$ cluster, based on $Pt_{13}Ni_{42}$, was created. The excess energies for Pt-Ni clusters in the present work, calculated using Eq. (5.35), are shown in Figure 6.5(b). They were calculated with respect to the icosahedral Ni_{55} and the DRC Pt_{55}. The focus in the present work was in the platinum-poor systems, because the aim is to reduce the use of platinum in HER catalysis. Therefore, the platinum-rich systems were not extensively studied and Figure 6.5(b) is not as comprehensive as Figure 6.5(a). The Figures show E_{exc} val-

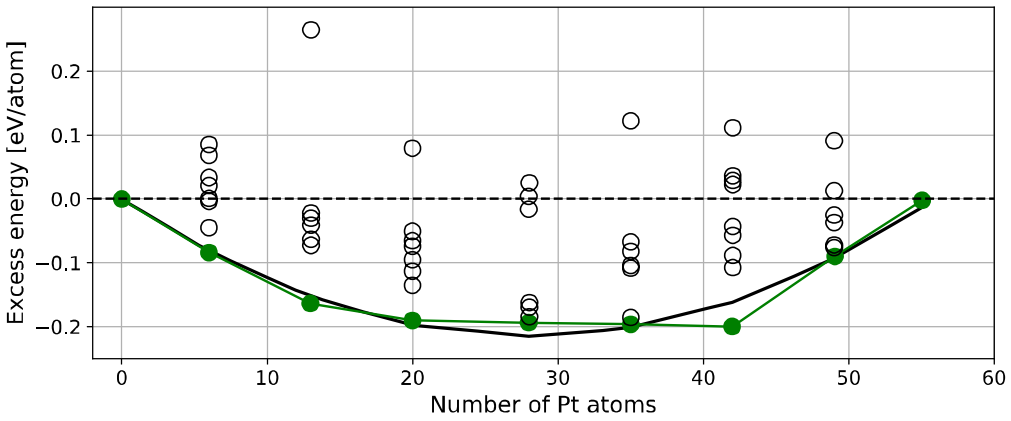

(a) Adapted from the study by Guedes-Sobrinho *et al.* [12].

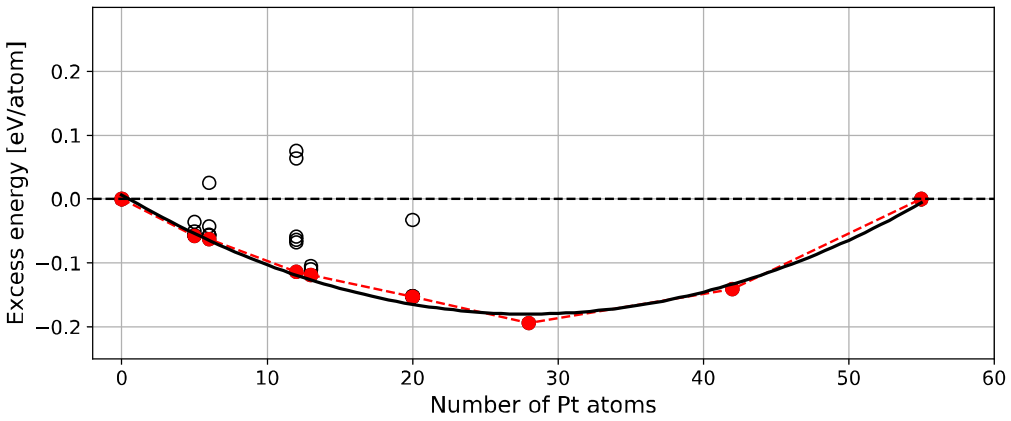

(b) The present work.

Figure 6.5 *The excess energies for the Pt_nNi_{55-n} systems as a function of the composition (number of Pt atoms). The filled red/green circles denote the lowest energy structures for each composition, whereas the unfilled black circles are the higher energy structures. The solid black curve is a parabolic fit to the lowest energy configurations.*

ues for the ground-state structures and various isomers. The isomers of $Pt_{12}Ni_{43}$ will be briefly discussed later in this chapter, but from now on the discussion will focus on the ground-state excess energies.

The excess energies calculated in Figures 6.5(a) and 6.5(b) follow parabolic behavior. The formation of Pt-Ni nanoclusters is energetically favorable for all studied compositions, because the excess energies of the ground-state configurations are negative. In Figure 6.5(a) the excess energy has a plateau for $n = 20$–42, which is not observed in Figure 6.5(b). Guedes-Sobrinho *et al.* [12] reported $Pt_{42}Ni_{13}$ (76 % of Pt) to be the most stable Pt-Ni composition. The structure of $Pt_{42}Ni_{13}$ is the icosahedral core-shell structure, where all 42 Pt atoms located in the surface and the 13-atom core consists of Ni atoms. $Pt_{42}Ni_{13}$ is not the most stable Pt-Ni composition in

Figure 6.5(b) and its E_{exc} is higher than in Figure 6.5(a). The reason for this might be the default (low) multiplicity used in the present work. It is also possible that the ground-state structure of $Pt_{42}Ni_{13}$ was not found, because in this work the Pt-rich systems were not studied extensively. The low multiplicity may also explain why the excess energies for $n = 6$–20 are slightly higher in Figure 6.5(b) compared to the corresponding values in Figure 6.5(a). It is unlikely that for $n = 6$–20 the structures were replicated incorrectly, because they are almost non-distorted Ni_{55} icosahedra.

According to Guedes-Sobrinho *et al.* [12], both $Pt_{12}Ni_{43}$ and $Pt_{20}Ni_{35}$ have the total magnetic moment per atom of $m_{\mathrm{T}} = 0.73\ \mu_{\mathrm{B}}$. For $n > 20$ compositions m_{T} decreases nearly parabolically until it reaches zero for Pt_{55}. In the present work, all magnetic moments were kept zero.

Platinum atoms prefer to replace nickel atoms located in the surface of icosahedral Ni_{55} structure [12], whereas the nickel atoms prefer the core region, which consist of nickel atoms only, except in the case of $Pt_{49}Ni_6$. This is explained by the larger atomic radius of Pt atoms compared to Ni atoms, and that the segregation energy of Ni in the 55-atom Pt particles is positive [12]. Guedes-Sobrinho *et al.* [12] found that for the surface atoms of the 55-atom Pt-Ni clusters, the center of gravity of the occupied *d*-states is a linear function of the number of Pt atoms (n). It shifts towards the HOMO level (the highest occupied molecular orbital) when the surface Pt atoms are replaced by Ni atoms, The shift is particularly important in the perspective of catalysis, because according to the *d*-band model, it enhances the adsorption of molecular species on the surface. Therefore, the magnitude of the adsorption energy of the 55-atom Pt-Ni nanoclusters can be tuned by altering the Pt concentration. Pt-Ni alloy particles have been experimentally studied as catalysts for oxygen reduction reactions (ORRs) [124] and the methanol electro-oxidation reaction [125], and the addition of Ni in Pt particles has been reported to enhance the reactivity.

6.3 Gas Phase Structures of $Pt_{12}Ni_{43}$ and $Pt_{20}Ni_{35}$ Clusters

Two Pt-poor compositions, $Pt_{12}Ni_{43}$ and $Pt_{20}Ni_{35}$, were chosen for further inspection. The ground-state structure for $Pt_{12}Ni_{43}$ was not found in the literature, therefore it was created from the ground-state structure of $Pt_{13}Ni_{42}$, reported by Guedes-Sobrinho *et al.* [12]. $Pt_{13}Ni_{42}$ has one Pt atom at each corner of the icosahedron and one extra Pt atom located in the surface. The ground-state structure for $Pt_{12}Ni_{43}$ was created by replacing the extra platinum atom with a nickel atom. The ground-state $Pt_{12}Ni_{43}$ structure is presented in Figure 6.6 inside the gas phase simulation box. All gas phase calculations were carried out in such box and in later figures the box is left out.

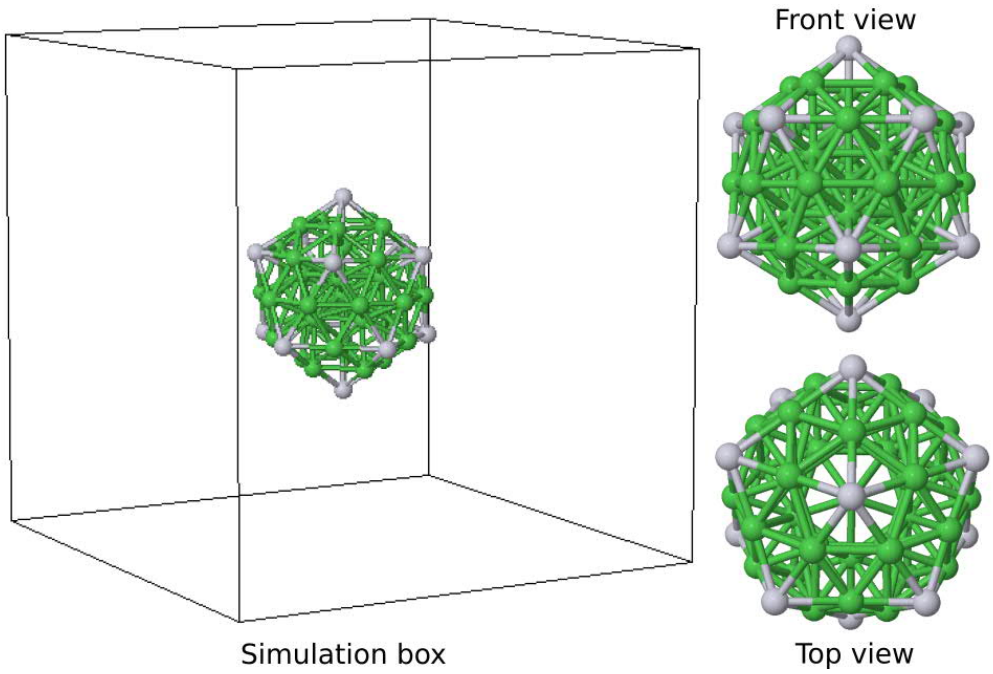

Figure 6.6 *The ground-state structure of $Pt_{12}Ni_{43}$ in the gas phase. The simulation box size is $25 \times 25 \times 25$ Å and the cluster is located at the center of the box.*

The ground-state $Pt_{12}Ni_{43}$ structure is icosahedral. All of its facets are identical and consist of 3 Ni atoms and 3 Pt atoms, which are at the corners. The structure is highly symmetrical, which is beneficial later when hydrogen coverage is investigated, because the symmetry reduces the number of possible site combinations. Several different isomers of $Pt_{12}Ni_{43}$ were also investigated to study the optimal distribution of Pt atoms in the cluster. Two examples of such isomers are shown in Figure 6.7. They are energetically 2.54 eV and 10.42 eV higher than the ground-state structure (Figure 6.6). The observations are in agreement with the results by Guedes-Sobrinho *et al.* [12], who reported that Pt prefers to be in the surface and to spread evenly. Therefore, the Pt atoms occupy the corners of the icosahedron and they are exposed to the vacuum region as much as possible.

The ground-state structure of $Pt_{20}Ni_{35}$ is icosahedral, as reported by Guedes-Sobrinho *et al.* [12]. Several different isomers of $Pt_{20}Ni_{35}$ were studied to find the ground-state structure and the lowest energy distribution of Pt atoms in the cluster surface. $Pt_{20}Ni_{35}$ is similar to the $Pt_{12}Ni_{43}$ ground-state structure, with 8 additional surface atoms changed from nickel to platinum. The ground-state $Pt_{20}Ni_{35}$ structure is presented in Figure 6.8 from various angles. It has 2 unique facets. All the corner atoms are Pt as in the $Pt_{12}Ni_{43}$ cluster, but the $Pt_{20}Ni_{35}$ structure is not symmetrical due to the additional 8 Pt atoms on the surface.

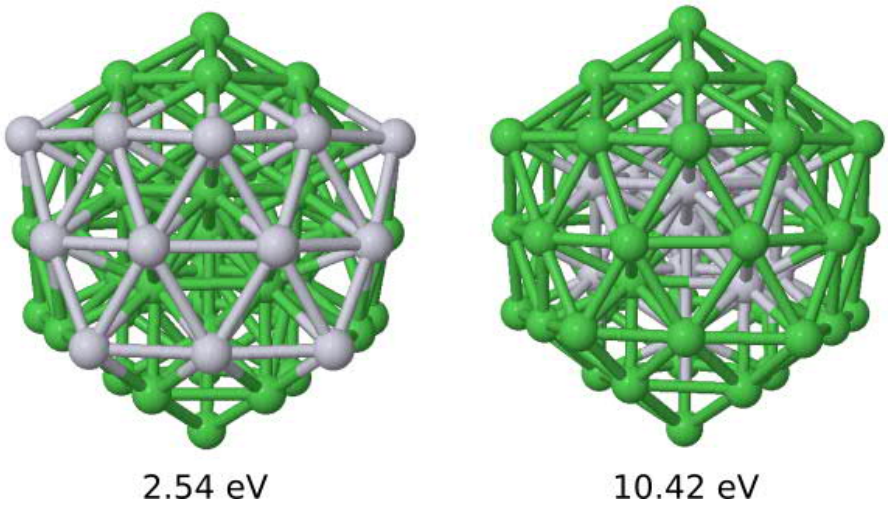

Figure 6.7 *Two relaxed $Pt_{12}Ni_{43}$ isomers which are energetically 2.54 eV and 10.42 eV higher compared to the ground-state structure (Figure 6.6). The core-shell structure (on the right) is very unfavorable, because platinum prefers to be in the surface. Platinum also prefers to spread evenly on the surface, which makes the structure on the left less favorable than the ground-state structure.*

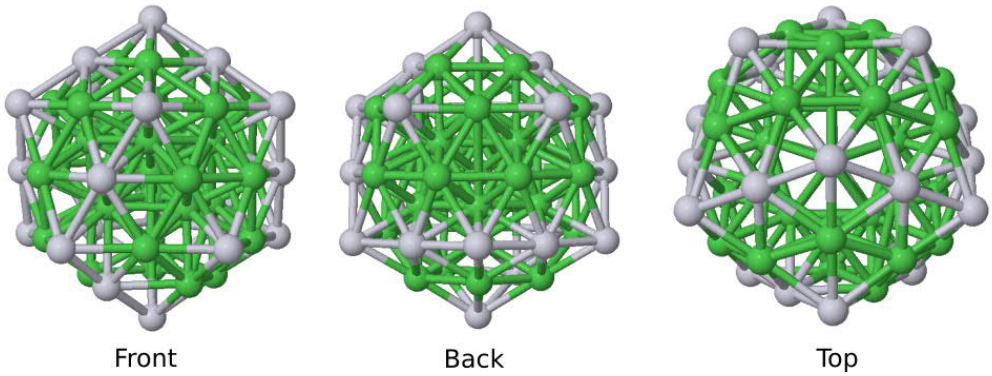

Figure 6.8 *The ground-state structure of $Pt_{20}Ni_{35}$ in the gas phase. The structure is shown from three different angles.*

The radial distribution functions for Pt-Pt, Ni-Ni, and Ni-Pt atom pairs were calculated with $\Delta r = 0.01$ Å for the $Pt_{12}Ni_{43}$ and $Pt_{20}Ni_{35}$ clusters. The results are shown in Figures 6.9(a) and 6.9(b). Both clusters are icosahedral and therefore their RDFs are very similar to RDF of Ni_{55} cluster. Some of the Ni-Ni RDF peaks have been replaced by either Pt-Pt or Ni-Pt RDF peaks, because Pt atoms have replace Ni atoms in the surface of the clusters. Pt has larger atomic radius than Ni, which distorts the Ni_{55} icosahedron slightly and causes minor shifts in the peaks. $Pt_{12}Ni_{43}$ has no nearest-neighbor Pt atoms, therefore the first Pt-Pt RDF peak is at 5.10 Å, which does not represent a Pt-Pt bond.

The cluster diameters and the average bond lengths, r_{ave}, between different atom

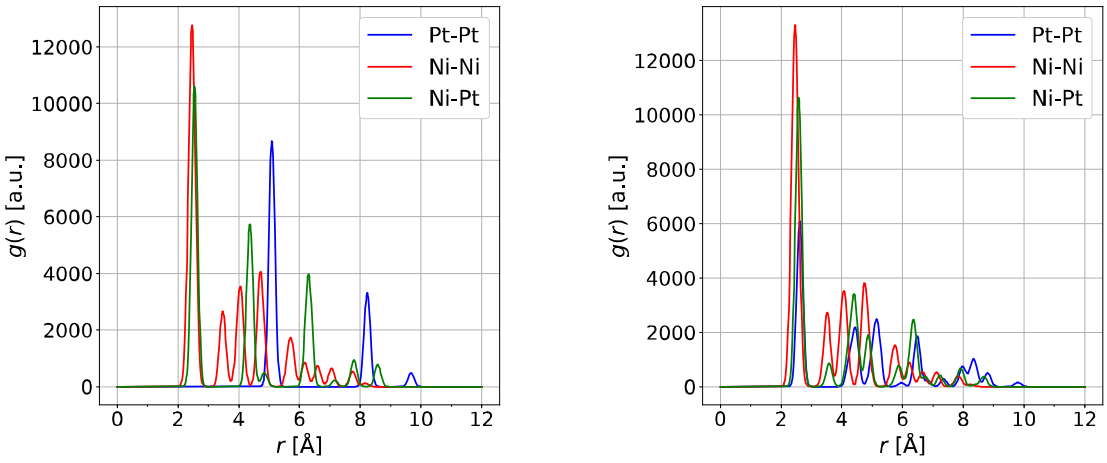

(a) $Pt_{12}Ni_{43}$ (b) $Pt_{20}Ni_{35}$

Figure 6.9 *The radial distribution functions (arbitrary units) for the most stable $Pt_{12}Ni_{43}$ and $Pt_{20}Ni_{35}$ configurations in the gas phase. Calculated with bin size $\Delta r = 0.01$ Å and smoothed with Gaussian functions ($\sigma = 0.1$). The corresponding geometries are shown in Figures 6.6 and 6.8, respectively.*

pairs were obtained from the RDF figures. These values are collected in Table 6.1 for the Ni_{55}, Pt_{55}, $Pt_{12}Ni_{43}$ and $Pt_{20}Ni_{35}$ clusters. In the $Pt_{20}Ni_{35}$ cluster, Pt-Pt atoms have the longest average bond length of 2.62 Å, which is slightly less than $r_{\text{ave}} = 2.67$ Å of the ground-state Pt_{55} cluster. The average Ni-Ni bond lengths are equal (2.46 Å) in the $Pt_{12}Ni_{43}$ and $Pt_{20}Ni_{35}$ clusters, and very close to $r_{\text{ave}} = 2.44$ Å of the ground-state Ni_{55}. The average Ni-Pt bond length is larger in $Pt_{20}Ni_{35}$ (2.58 Å) than in $Pt_{12}Ni_{43}$ (2.55 Å). The diameters of the $Pt_{12}Ni_{43}$ and $Pt_{20}Ni_{35}$ clusters are 9.68 Å and 9.80 Å, respectively. Therefore, both clusters are larger than Ni_{55} cluster (diameter of 9.26 Å) and $Pt_{20}Ni_{35}$ is larger than $Pt_{12}Ni_{43}$. These observations are in agreement with the results by Guedes-Sobrinho *et al.* [12], who reported the average bond length of Pt_nNi_{55-n} clusters to increase linearly as a function of n.

Table 6.1 *The average bond lengths r_{ave} between different atom pairs and cluster diameters for the Ni_{55}, Pt_{55}, $Pt_{12}Ni_{43}$ and $Pt_{20}Ni_{35}$ systems. The average bond length is defined as the location of the first RDF peak. $Pt_{12}Ni_{43}$ structure has no Pt atoms next to each other, therefore r_{ave} is undefined. Cluster diameter is equal to the location of the last RDF peak.*

	Ni_{55}	Pt_{55}	$Pt_{12}Ni_{43}$	$Pt_{20}Ni_{35}$
r_{ave} (Ni-Ni) [Å]	2.44	–	2.46	2.46
r_{ave} (Ni-Pt) [Å]	–	–	2.55	2.58
r_{ave} (Pt-Pt) [Å]	–	2.67	–	2.62
Cluster diameter [Å]	9.26	11.2	9.68	9.80

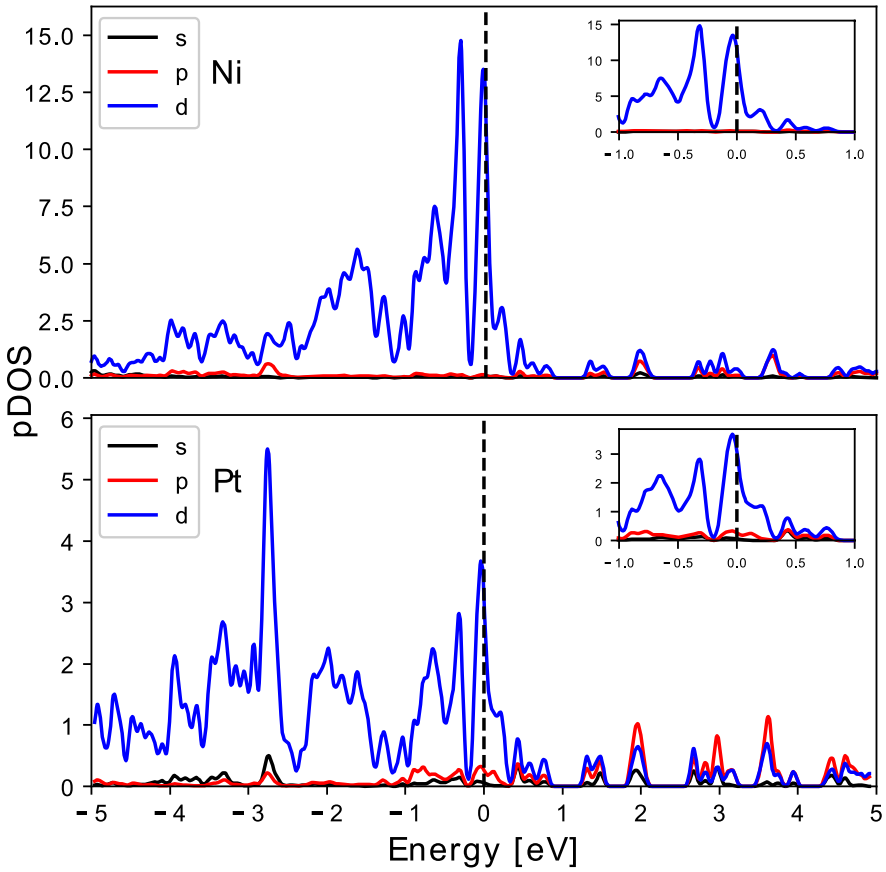

Figure 6.10 *The projected density of states (PDOS) of the ground-state $Pt_{20}Ni_{35}$ cluster in the gas phase, shown in Figure 6.8. The PDOS values were smoothed with Gaussian functions with $\sigma = 0.0367$ eV. The Fermi level is set as zero and represented by the dashed line.*

For the inspection of the electronic structure of the $Pt_{12}Ni_{43}$ and $Pt_{20}Ni_{35}$ ground-state structures in the gas phase, their projected density of states (PDOS) including s, p, and d orbitals were calculated. $Pt_{20}Ni_{35}$ PDOS is presented in Figure 6.10, whereas the figure of $Pt_{12}Ni_{43}$ PDOS can be found in Appendix A. The contribution of Ni is larger, because in both systems the number of Ni atoms is larger than that of Pt atoms. The $Pt_{12}Ni_{43}$ and $Pt_{20}Ni_{35}$ clusters are metallic, because there is no band gap at the Fermi energy. The *d*-states are prevalent, which is a promising indicator for the interaction with reactant molecules and catalytic activity [126].

6.4 $Pt_{12}Ni_{43}$ and $Pt_{20}Ni_{35}$ Clusters on Al_2O_3 Support

In real life catalysis applications, catalyst nanoparticles are usually deposited on a support, *e.g.* alumina Al_2O_3 or graphite. Therefore, the most stable structures of $Pt_{12}Ni_{43}$ and $Pt_{20}Ni_{35}$ were aligned on a γ-alumina slab. Different facets, several

different orientations and locations of both clusters were tested to find the most favorable adsorbed state of $Pt_{12}Ni_{43}$ and $Pt_{20}Ni_{35}$ on Al_2O_3 support. The facet is irrelevant for $Pt_{12}Ni_{43}$ cluster, because all of its facets are identical. $Pt_{20}Ni_{35}$ has two unique facets which were both tested.

The most favorable orientation of the adsorbed $Pt_{12}Ni_{43}$ cluster is shown in Figure 6.11, which includes simulation box and the view from different perspectives. The $Pt_{12}Ni_{43}$ cluster has one of its facets against the support, emphasized with the red triangle in Figure 6.11. The adsorbed cluster is slightly tilted and it retains its icosahedral shape without deforming.

The most favorable orientation of the adsorbed $Pt_{20}Ni_{35}$ cluster is shown in Figure 6.12. Interestingly, $Pt_{20}Ni_{35}$ behaves differently than $Pt_{12}Ni_{43}$ and prefers the more tilted orientation, where two of its facets are almost equally against the alumina support. Both of these facets are similar to the most favorable $Pt_{12}Ni_{43}$ facet and contain as few Pt atoms as possible. The platinum atoms prefer to be as far from the support as possible. $Pt_{20}Ni_{35}$ retains its icosahedral shape and does not deform when adsorbed.

The adsorption energies of the $Pt_{12}Ni_{43}$ and $Pt_{20}Ni_{35}$ clusters adsorbed on the Al_2O_3 surface are 7.18 eV and 7.47 eV, respectively. They were calculated using Eq. (5.36). The adsorption energies, the charge transfers and the range of bond lengths of the $Pt_{12}Ni_{43}$ and $Pt_{20}Ni_{35}$ clusters adsorbed on the Al_2O_3 surface are collected in Table 6.2.

$Pt_{12}Ni_{43}$ is adsorbed on the Al_2O_3 surface with 6 Pt-Al bonds, 3 Pt-O bonds, 8 Ni-Al bonds, and 3 Ni-O bonds. The average bond lengths are 2.90 Å, 2.22 Å, 2.90 Å, and 1.99 Å, respectively. For $Pt_{20}Ni_{35}$, the corresponding values are 4 Pt-Al bonds, 4 Pt-O bonds, 9 Ni-Al bonds, and 5 Ni-O bonds, with average bond lengths of 2.50 Å, 2.31 Å, 2.77 Å, and 2.17 Å, respectively.

The radial distribution functions for Pt-Pt, Ni-Ni, and Ni-Pt atom pairs of the adsorbed $Pt_{12}Ni_{43}$ and $Pt_{20}Ni_{35}$ clusters were calculated $\Delta r = 0.01$ Å. They do not differ noticeably from the RDFs calculated for the gas phase clusters (Figures 6.9(a) and 6.9(b)). Therefore, the clusters retain their gas phase shape when adsorbed on the support. The RDF figures can be found in Appendix B.

Bader charge analysis was performed for the adsorbed $Pt_{12}Ni_{43}$ and $Pt_{20}Ni_{35}$ clusters. The charges of Ni and Pt atoms in the $Pt_{12}Ni_{43}$ gas phase cluster are $-0.12e$/atom and $+0.44e$/atom, respectively. After the adsorption, the corresponding charges are $-0.13e$/atom and $+0.39e$/atom. Ni and Pt atoms accumulate $-0.14e$ and $-0.58e$

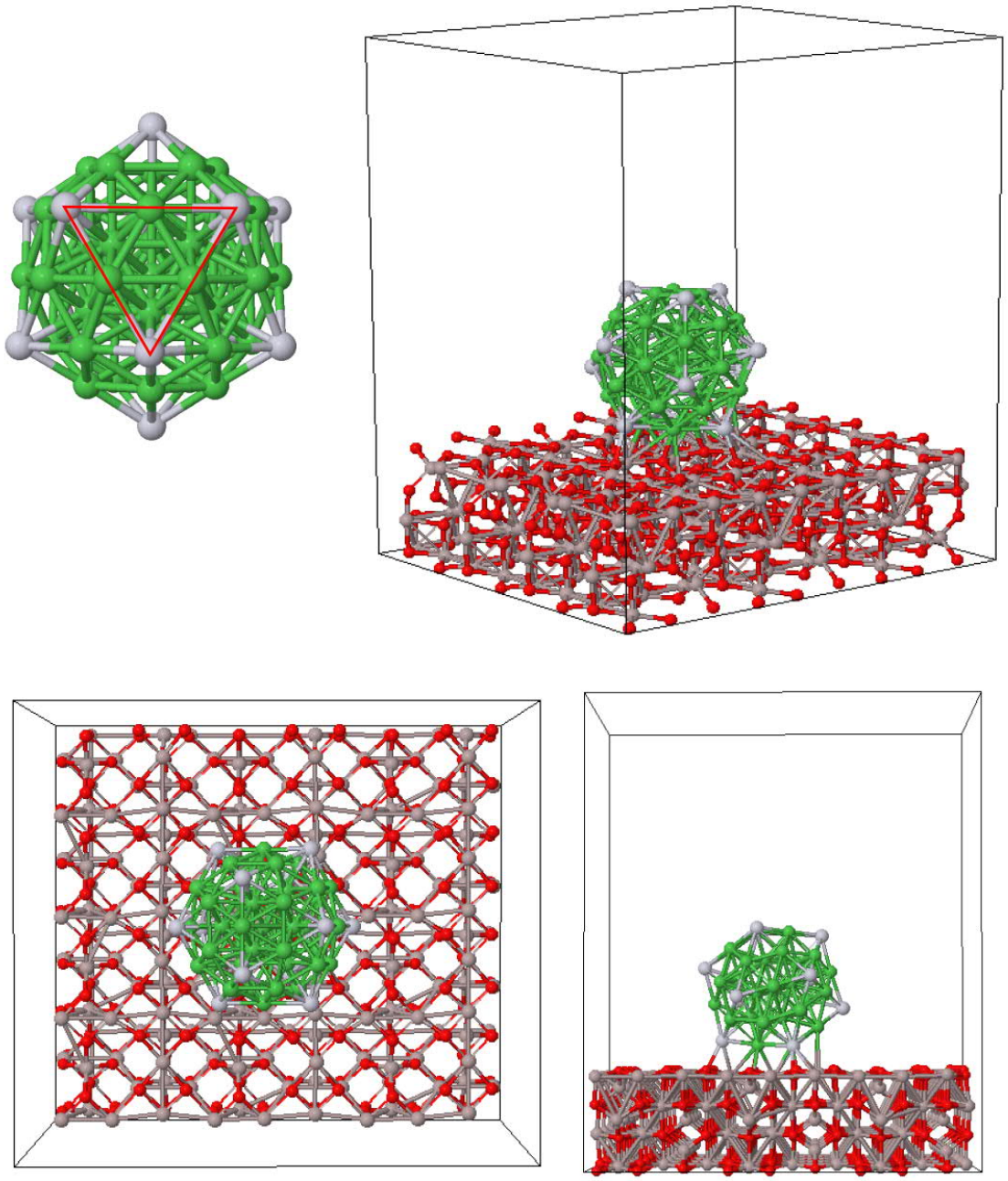

Figure 6.11 *$Pt_{12}Ni_{43}$ adsorbed on Al_2O_3 support. The most favorable adsorption facet is emphasized with the red triangle.*

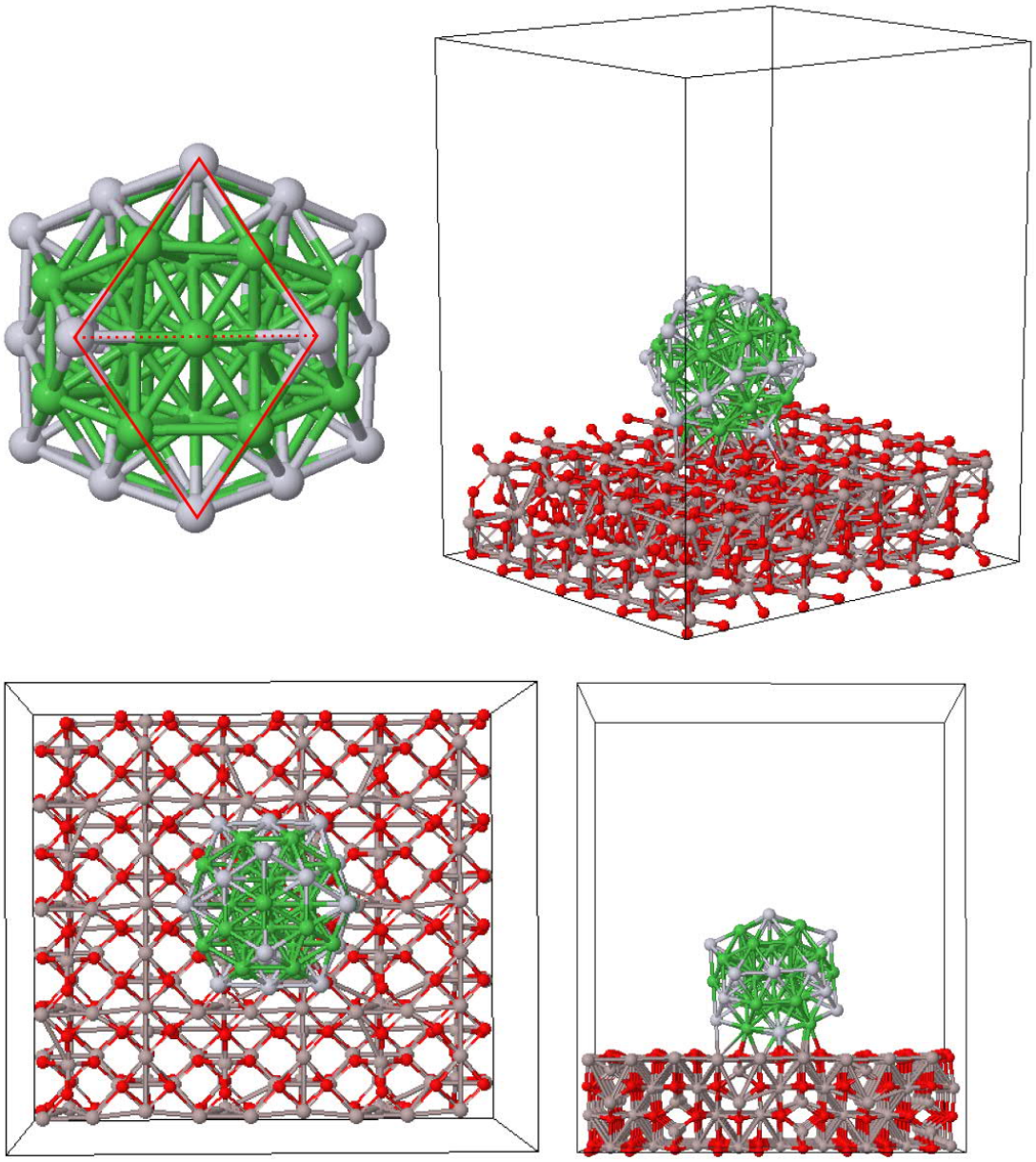

Figure 6.12 *$Pt_{20}Ni_{35}$ adsorbed on Al_2O_3 support. The cluster prefers to adsorb with two facets against the alumina slab. These facets are bordered with red color.*

Table 6.2 *The adsorption energies, the charge transfers and the range of bond lengths of the $Pt_{12}Ni_{43}$ and $Pt_{20}Ni_{35}$ clusters adsorbed on the Al_2O_3 surface. The charge transfer values (CT) were calculated using Eq.* (5.42) *and are equal to the net charge carried by the adsorbed clusters. The average bond lengths are in brackets. Because $Pt_{20}Ni_{35}$ cluster has two facets towards the alumina surface, both of them were taken into account. The values are calculated for atoms which are bordered by the red triangles in Figures 6.11 and 6.12.*

	$Pt_{12}Ni_{43}@Al_2O_3$	$Pt_{20}Ni_{35}@Al_2O_3$
E_{ads} [eV]	7.18	7.47
CT	$-0.72e$	$-1.01e$
R_{Pt-Al} [Å]	2.55–3.30 (2.90)	2.31–2.67 (2.50)
R_{Pt-O} [Å]	2.18–2.27 (2.22)	2.23–2.39 (2.31)
R_{Ni-Al} [Å]	2.50–3.29 (2.90)	2.46–3.17 (2.77)
R_{Ni-O} [Å]	1.97–2.04 (1.99)	1.96–2.48 (2.17)

of electron density from the Al_2O_3 support, respectively. In total the net charge carried by the adsorbed $Pt_{12}Ni_{43}$ cluster is $-0.72e$.

In the $Pt_{20}Ni_{35}$ cluster in the gas phase, Ni and Pt atoms carry the total charge of $-0.18e$/atom and $+0.32e$/atom, respectively. After the adsorption, the corresponding charges are $-0.19e$/atom and $+0.28e$/atom. The charge transfers of Ni and Pt atoms are $-0.27e$ and $-0.75e$, respectively. Ni and Pt atoms therefore accumulate charge from the support. The $Pt_{20}Ni_{35}$ cluster carries the net charge of $-1.01e$.

In conclusion, the support donates $0.72e$ and $1.01e$ of electron density to the $Pt_{12}Ni_{43}$ and $Pt_{20}Ni_{35}$ clusters, respectively. This is beneficial in catalysis perspective, because the negatively charged catalyst clusters are prone to interact with adsorbate molecules [126]. The charge density difference (CDD) for the $Pt_{12}Ni_{43}$ and $Pt_{20}Ni_{35}$ clusters on the Al_2O_3 support is visualized in Figure 6.13. A significant accumulation and depletion of charge is observed at the interface between each cluster and the support.

The projected density of states of s, p, and d orbitals of the Pt and Ni atoms of $Pt_{12}Ni_{43}$ and $Pt_{20}Ni_{35}$ clusters adsorbed on the alumina Al_2O_3 surface are presented in Figures 6.14 and 6.15. The Figures also include the PDOS of s and p orbitals of the Al and O atoms of the alumina slab. At the Fermi energy, PDOS has considerable weight on the catalyst clusters (Ni and Pt), whereas the Al_2O_3 support has a large band gap and it is an insulator. The significant contribution of the *d*-states to PDOS is a promising indicator for the interaction with reactant molecules and catalytic activity [126].

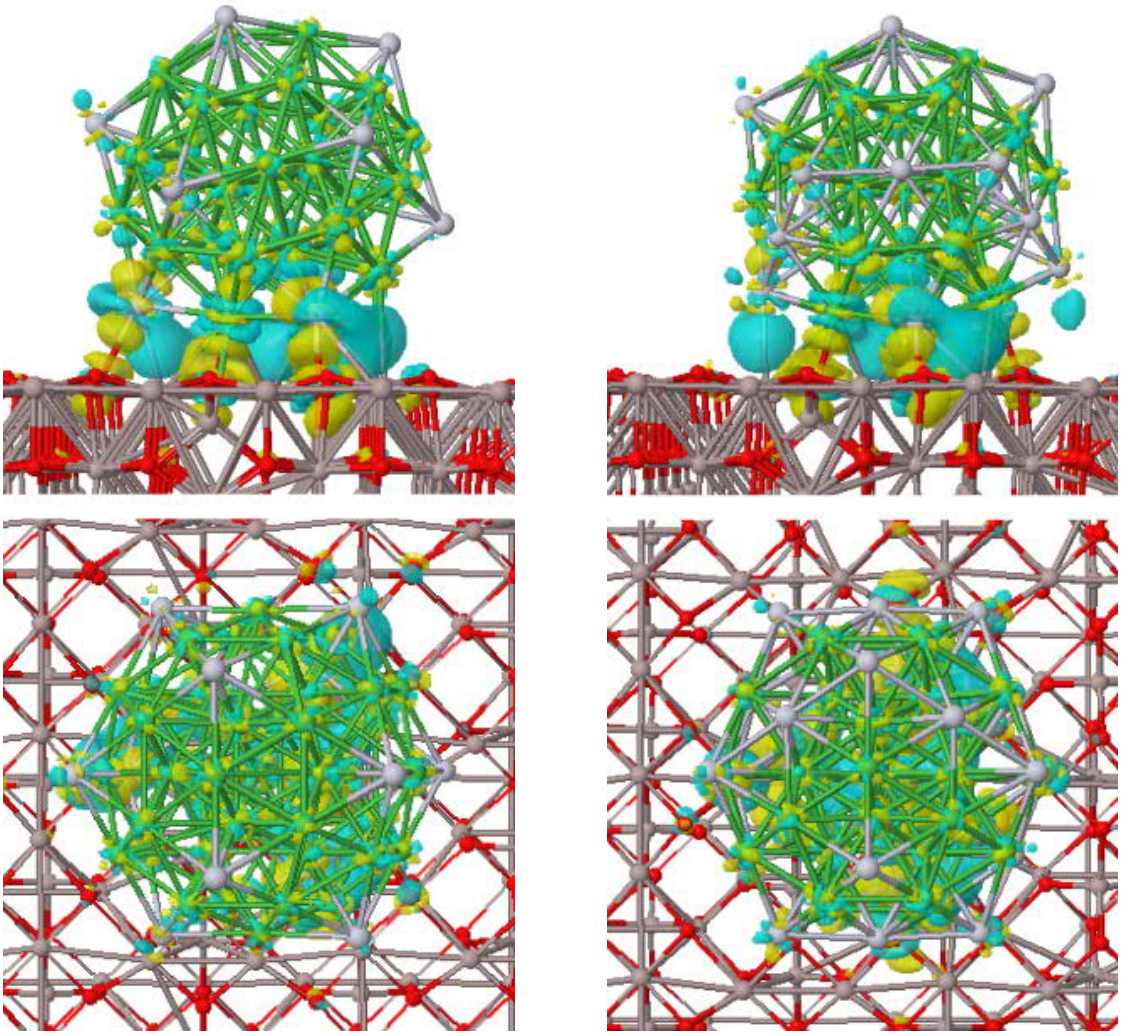

(a) $Pt_{12}Ni_{43}@Al_2O_3$: the net charge accumulation in the cluster is $0.72e$.

(b) $Pt_{20}Ni_{35}@Al_2O_3$: the net charge accumulation in the cluster is $1.01e$.

Figure 6.13 *Side and top views of the charge density difference (CDD) for the $Pt_{12}Ni_{43}$ and $Pt_{20}Ni_{35}$ clusters on the Al_2O_3 support. The yellow and cyan colors represent charge accumulation and depletion, respectively. The net accumulations are from Table 6.2. The isosurface values are* $0.003 \pm e/a_0^3$.

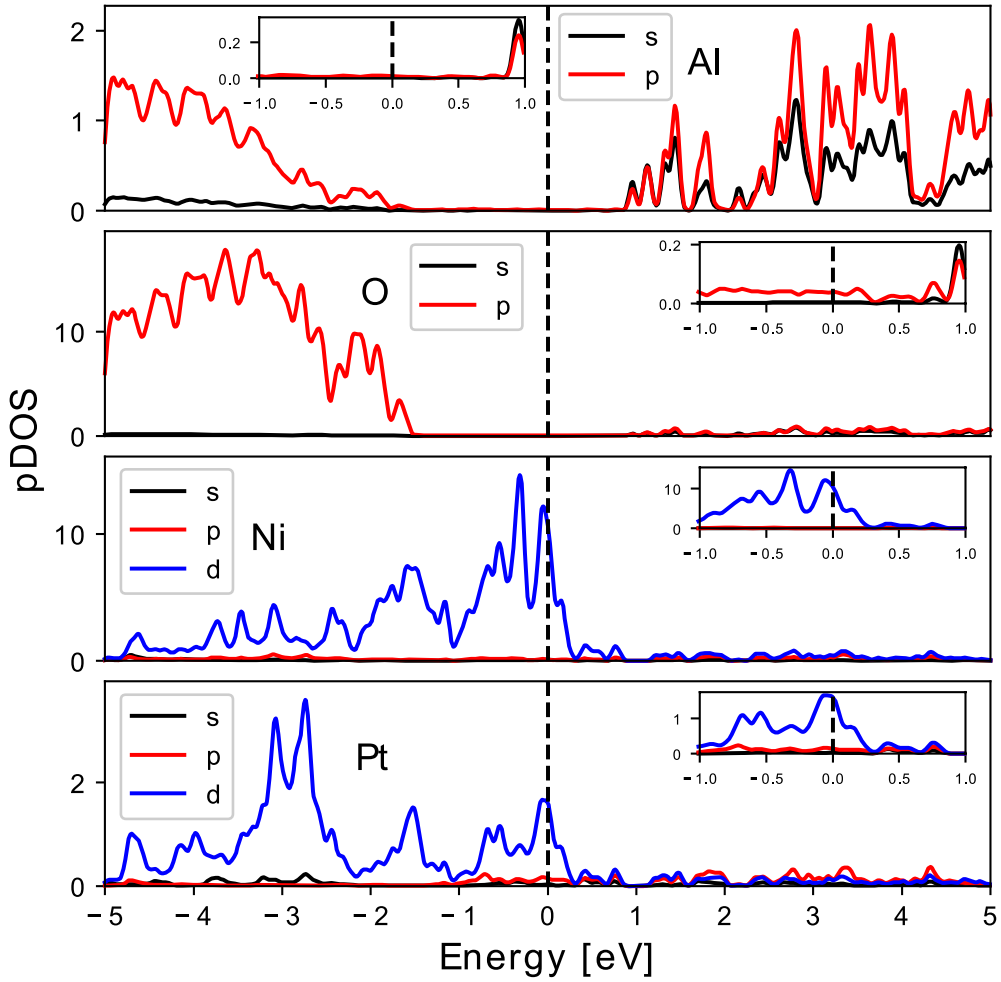

Figure 6.14 *The projected density of states (PDOS) of the $Pt_{12}Ni_{43}$ cluster adsorbed on Al_2O_3 surface. The system is shown in Figure 6.11. The Fermi level is set as zero and represented by the dashed line.*

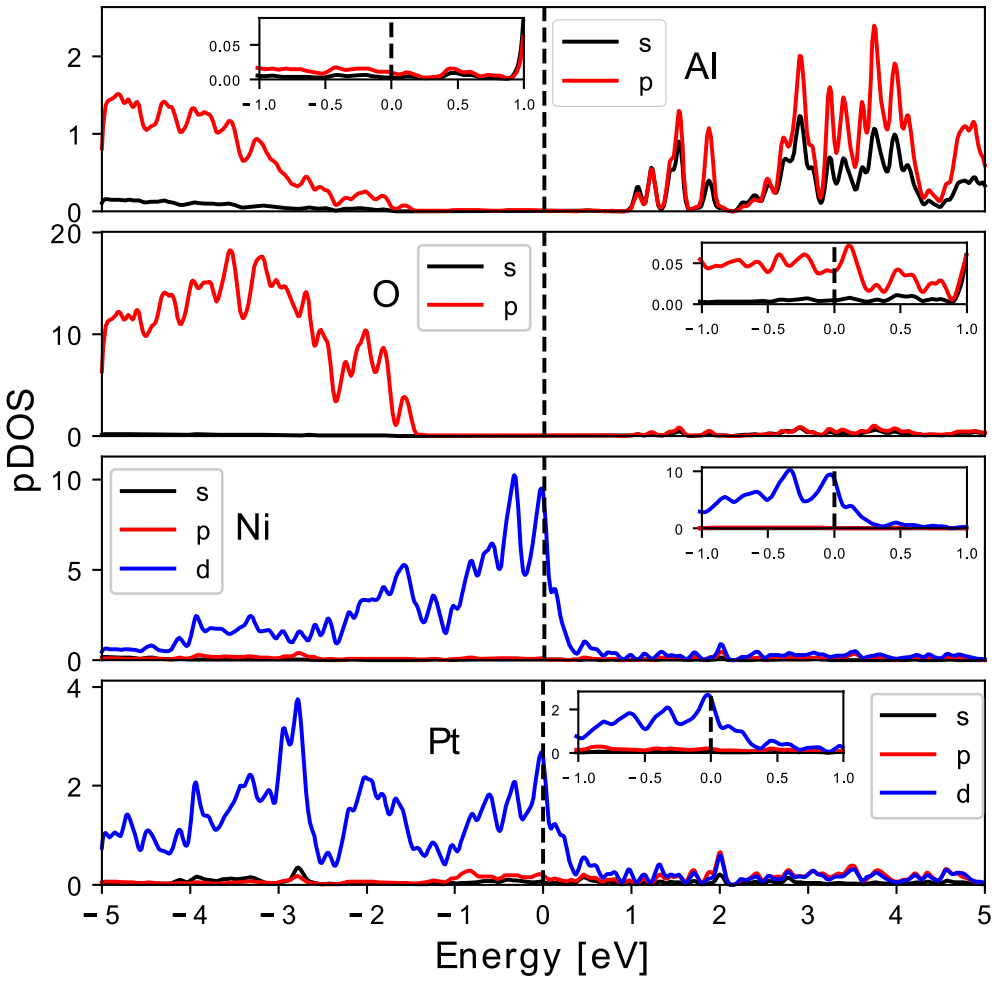

Figure 6.15 *The projected density of states (PDOS) of the $Pt_{20}Ni_{35}$ cluster adsorbed on Al_2O_3 surface. The system is shown in Figure 6.12. The Fermi level is set as zero and represented by the dashed line.*

7. HYDROGEN ADSORPTION ON 55-ATOM PT-NI NANOCLUSTERS IN THE GAS PHASE AND ON ALUMINA

The hydrogen adsorption on the $Pt_{12}Ni_{43}$ and $Pt_{20}Ni_{35}$ nanoclusters will be presented in this chapter. The aim is to find the critical hydrogen coverage using the method based on the differential free energy, presented at the end of Chapter 4. All values in this work are reported at the cathodic potential of $U = 0$ V. After the critical coverage has been found, the HER activity of the clusters is estimated using the ΔG_{H^*} descriptor.

This chapter is organized as follows. The hydrogen adsorption results for the $Pt_{12}Ni_{43}$ cluster in the gas phase and on the Al_2O_3 support are presented in detail in Sections 7.1 and 7.2, respectively. The results are summarized and the HER activity of the $Pt_{12}Ni_{43}$ and $Pt_{20}Ni_{35}$ clusters is estimated in Section 7.3, which also briefly discusses the hydrogen adsorption on the $Pt_{20}Ni_{35}$ cluster in the gas phase.

7.1 Hydrogen Adsorption on $Pt_{12}Ni_{43}$ in the Gas Phase

Studying the adsorption of hydrogen in the gas phase is beneficial, because the gas phase calculations are computationally cheaper compared to the slab calculations. The section is divided into three subsections. The two first subsections discuss hydrogen adsorption mechanisms at low hydrogen coverages (1–7 adsorbed H atoms) and high coverages (73–81 adsorbed H atoms), respectively. The charge transfer and the effect of a high hydrogen coverage on the properties of the cluster are analyzed in the third subsection.

7.1.1 Adsorption of 1–7 H Atoms

The facets of $Pt_{12}Ni_{43}$ are (111)-like, therefore it was assumed that the possible active sites are the top, bridge, and hollow sites, similarly to fcc(111) transition metal surfaces (Figure 4.3(a)) [79, 84]. Therefore, there are six different types of

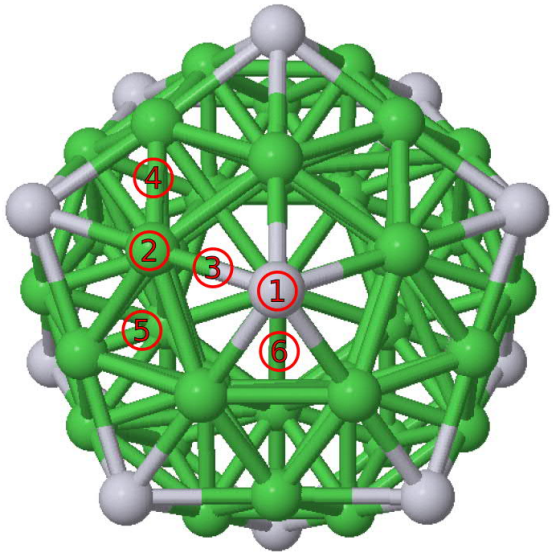

Figure 7.1 *The six different types of hydrogen adsorption sites considered in the present work for the $Pt_{12}Ni_{43}$ cluster in the gas phase: Pt top (1), Ni top (2), Pt-Ni bridge (3), Ni-Ni bridge (4), Ni_3 hollow (5), and Pt-Ni_2 hollow (6).*

sites on the surface of the $Pt_{12}Ni_{43}$ cluster, illustrated in Figure 7.1; Pt top, Ni top, Pt-Ni bridge, Ni-Ni bridge, Ni_3 hollow, and Pt-Ni_2 hollow sites. $Pt_{12}Ni_{43}$ has no Pt-Pt bridge sites or Pt_2-Ni hollow sites. Every Ni_3 hollow site has one core Ni atom near it, which is not the case for the Pt-Ni_2 hollow sites. Therefore, there is more free space below the Pt-Ni_2 hollow sites than the Ni_3 hollow sites.

To investigate, which adsorption site(s) a single hydrogen atom prefers, the adsorption of one H atom was sampled by using all sites presented in Figure 7.1 as initial positions of the H atom. The structure of the cluster and the position of the H atom were relaxed for each sample. The differential Gibbs free energies, ΔG_{diff}, were calculated using Eq. (4.10) and the results are presented in Table 7.1. Despite multiple attempts to relax the position of the H atom on Ni top and Pt top sites, the H atom always translated and relaxed into a Pt-Ni bridge site. Similar phenomenon occurred when the initial H position was on a Ni-Ni bridge site, which relaxed into a Pt-Ni_2 hollow. In conclusion, the hydrogen atom does not prefer top sites and Ni-Ni bridge sites, which are either very small local minima or saddle points in the potential energy surface.

The Ni_3 hollow site is the preferred H adsorption site with $\Delta G_{\text{diff}} = -0.41$ eV, whereas the Pt-Ni bridge and the Pt-Ni_2 hollow site are energetically 0.07 eV and 0.10 eV higher, respectively. In the Ni_3 hollow site the length of each Ni-H bond is 1.72 Å. Kristinsdóttir and Skúlason [89] reported the adsorption energy of an H atom on both Ni(111) and Pt(111) hollow sites to be -0.37 eV, whereas Wexler *et*

al. [24] reported that Ni_3 hollow sites on the Ni_3P_2 surface[1] are the strongly binding sites with $\Delta G_{\text{diff}} = -0.47$ eV. Both of these reported values are close to the value obtained in this work (-0.41 eV), despite the systems being different.

Table 7.1 *The differential Gibbs free energies of adsorption for a single H atom adsorbed on different types of sites of the $Pt_{12}Ni_{43}$ cluster. The corresponding sites are illustrated in Figure 7.1. The H atom on Pt top or Ni top relaxed into Pt-Ni bridge site, whereas the H atom on Ni-Ni bridge relaxed into a Pt-Ni_2 hollow site. The Ni_3 hollow is the most strongly binding site.*

Site	ΔG_{diff} [eV]
Pt top	Relaxed into Pt-Ni bridge
Ni top	Relaxed into Pt-Ni bridge
Pt-Ni Bridge	-0.34
Ni-Ni bridge	Relaxed into Pt-Ni_2 hollow
Ni_3 hollow	-0.41
Pt-Ni_2 hollow	-0.31

To find the critical hydrogen coverage, hydrogen atoms were added one by one on the surface of the cluster. In order to find the ground-state structure for each number of adsorbed hydrogen atoms, n_{H}, the adsorption sites were sampled by creating a set of approximately 30–50 initial positions. The following assumptions were made when creating the initial positions: (i) Pt top and Ni top sites are unfavorable and thus they can be ignored, (ii) a new H atom prefers sites, which are near any already adsorbed H atom (a nearest neighbor or a next-nearest neighbor site), and (iii) the adsorbed $n_{\text{H}} - 1$ H atoms are in their optimal positions. Together these assumptions mean that when a new H atom was added, its initial position was considered to be a bridge site or a hollow site near the adsorbed H atoms. Symmetry was taken into account whenever possible to reduce the number of initial positions. It will be seen later in this chapter, that the assumption (i) is in invalid when n_{H} is large (approximately $n_{\text{H}} > 65$). Assumption (iii) is certainly not valid in all situations, but without it the number of initial positions would increase drastically, even with only a few adsorbed hydrogen atoms.

Up to 7 adsorbed H atoms were added on the surface of the cluster. The ΔG_{diff} values for the discovered $n_{\text{H}} = 2$–7 ground-state structures, calculated using Eq. (4.9), are collected in Table 7.2. All energies are considerably below zero and close to the adsorption energy of one H atom (-0.41 eV). The adsorption energy does not change as a function of n_{H}. The $Pt_{12}Ni_{43}$ cluster with $n_{\text{H}} = 7$ is shown in Figure 7.2.

All H atoms prefer to adsorb on Ni_3 hollow sites, except the 4th and the 5th H

[1] Ni_2P has two bulk layers along the crystal's (0001) axis: Ni_3P and Ni_3P_2. Ni_3P_2 is the more stable bulk-like termination of Ni_2P. [24]

Table 7.2 *The differential Gibbs free energies of adsorption for n_H = 1–7 H atoms adsorbed on the $Pt_{12}Ni_{43}$ cluster in the gas phase according to Eq. (4.9). Adsorption site describes the site where the last H atom adsorbed. The cluster structure with n_H = 7 is presented in Figure 7.2.*

n_H	ΔG_{diff} [eV]	Adsorption site
1	−0.41	Ni_3 hollow
2	−0.43	Ni_3 hollow
3	−0.41	Ni_3 hollow
4	−0.43	Pt-Ni bridge
5	−0.53	Pt-Ni bridge
6	−0.44	Ni_3 hollow
7	−0.40	Ni_3 hollow

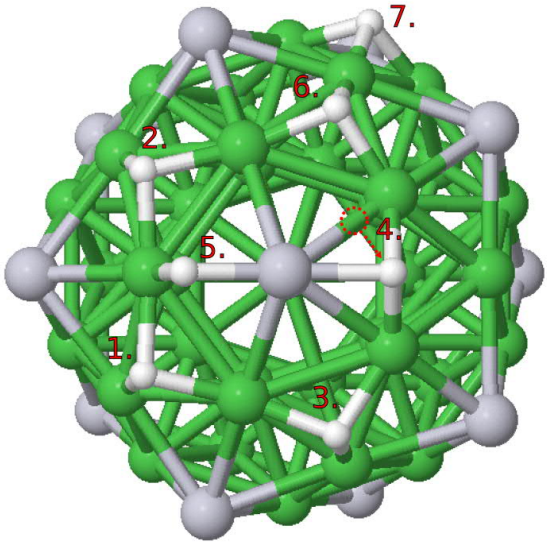

Figure 7.2 *The relaxed $Pt_{12}Ni_{43}$ cluster in the gas phase with the hydrogen coverage consisting of 7 H atoms. The numbers represent the order in which the H atoms are adsorbed. The 4th H atom initially adsorbs on the Pt-Ni bridge site, illustrated by the red dashed circle. When the 5th H atom is adsorbed, the 4th H atom moves to the Pt-Ni_2 hollow site. The corresponding differential Gibbs free energies of adsorption are listed in Table 7.2.*

atoms, which prefer Pt-Ni bridge sites. When the 5th H atom is added on the Pt-Ni bridge site, the 4th H atom moves to the neighboring Pt-Ni_2 hollow site. This is illustrated in Figure 7.2 by the red dashed circle and the arrow. The configuration, where one H atom is on the Pt-Ni bridge and the other H atom on the Pt-Ni_2 hollow site, has $\Delta G_{diff} = -0.53$ eV. This is approximately 0.1 eV lower compared to the other adsorption energies, which are between −0.40 eV and −0.44 eV. This suggests that it is energetically favorable for a hydrogen atom pair to adsorb as the 4th and 5th atoms in Figure 7.2.

7.1.2 Critical Hydrogen Coverage

Because the ΔG_{diff} values for the $n_{\text{H}} = 1$–7 coverages are considerably negative, a more robust approach was chosen to find the critical coverage ($\Delta G_{\text{diff}} \cong 0$). The cluster with high hydrogen coverages consisting of 73–81 H atoms were sampled with 30-50 initial hydrogen coverage configurations for each n_{H}. The ΔG_{diff} values for the discovered $n_{\text{H}} = 73$–81 ground-state structures are presented in Table 7.3. ΔG_{diff} changes its sign from negative to positive between $n_{\text{H}} = 79$ and 80, therefore the critical coverage is $n_{\text{H}} = 80$. The structures for $n_{\text{H}} = 73$–81 coverages will be discussed below.

Table 7.3 *The differential Gibbs free energies of adsorption for $n_{\text{H}} = 73$–81 H atoms adsorbed on the $Pt_{12}Ni_{43}$ cluster in the gas phase. Calculated with Eq. (4.9). Adsorption site describes the site where the last H atom is adsorbed.*

n_{H}	ΔG_{diff} [eV]	Adsorption site
73	−0.13	Ni_3 hollow
74	−0.24	Pt top
75	−0.11	Pt top
76	−0.13	Pt top
77	−0.10	Pt top
78	−0.13	Pt top
79	−0.10	Ni_3 hollow
80	0.12	Ni_3 hollow (critical coverage)
81	0.22	Pt-H_2 complex

The critical coverage configuration ($n_{\text{H}} = 80$) is shown in Figure 7.3. Interestingly, the number of adsorbed hydrogen atoms and the total number of hollow sites are equal, because the cluster has 20 facets, each of which has 4 hollow sites. At the critical coverage, H atoms occupy all Ni_3 hollow and Pt top sites, whereas only 4 out of 5 Pt-Ni bridge sites around each Pt atom are occupied, as illustrated in Figure 7.3(b). The hydrogen coverage exhibits high symmetry and all facets are nearly equal in terms of hydrogen coverage. The two H atoms on Pt-Ni bridge sites next to the empty Pt-Ni bridge site are not exactly on the Pt-Ni bridge sites, but slightly tilted towards the empty Pt-Ni bridge site. All Pt atoms bond with 5 H atoms, whereas Ni atoms bond with 3 or 4 H atoms.

Pt top sites are considerably more favorable for the adsorption of the 80th H atom than empty Pt-Ni bridge sites. A reasonable explanation for this is that the occupation of the Pt top sites prevents the H coverage becoming too close-packed. If an H atom occupies a Pt-Ni bridge site instead of a Pt top site, the total energy increases by 0.60 eV. These configurations are illustrated in Figures 7.4(b) and 7.4(a),

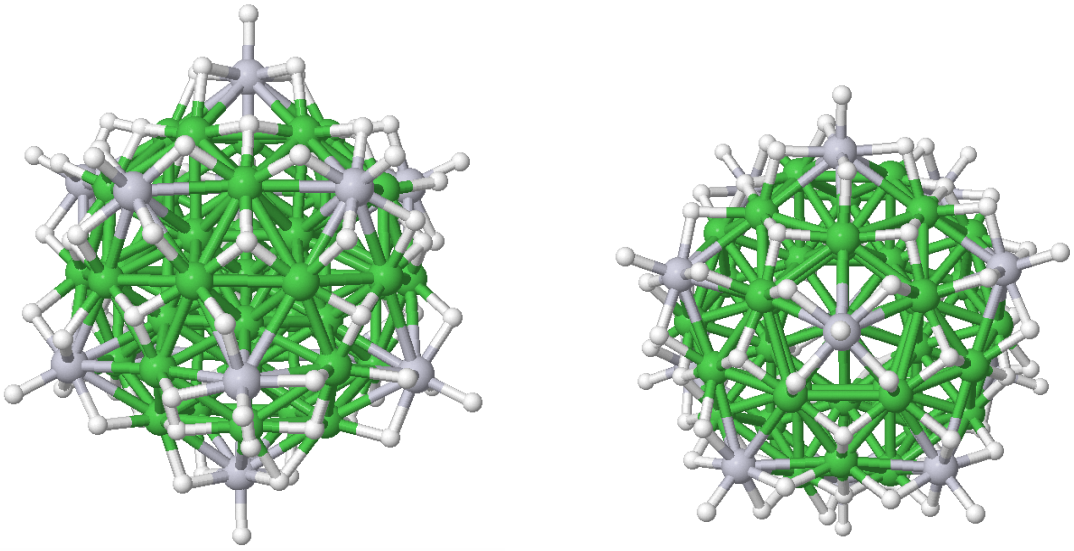

(a) Front view (b) Top view

Figure 7.3 *The $Pt_{12}Ni_{43}$ gas phase cluster with the critical hydrogen coverage, which consists of 80 H atoms. H atoms occupy all Ni_3 hollow and Pt top sites, whereas 4 out of 5 Pt-Ni bridge sites around each Pt atom are occupied.*

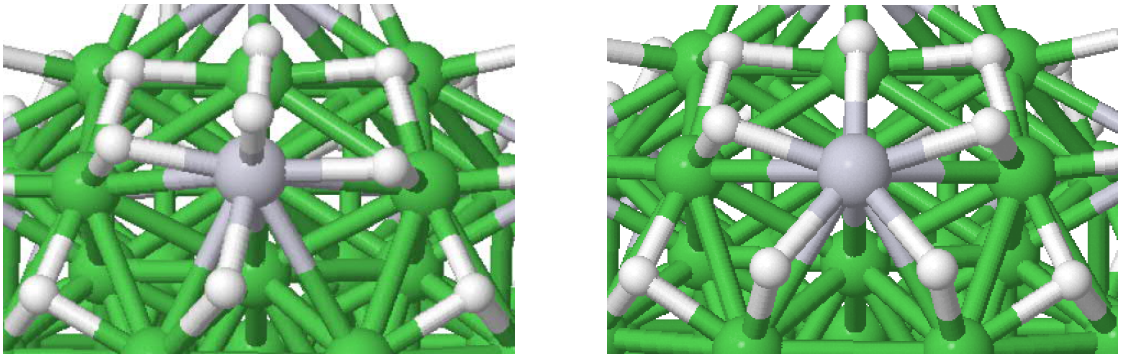

(a) 4 H atoms adsorbed on Pt-Ni bridge sites around a Pt atom and 1 H atom on the Pt top site. The ground-state configuration.

(b) 5 H atoms adsorbed on the Pt-Ni bridge sites around a Pt atom and the Pt top site is empty. 0.60 eV higher in energy than the ground-state.

Figure 7.4 *An example of H site sampling: a comparison of hydrogen adsorption on a Pt-Ni bridge and a Pt top site in the $Pt_{12}Ni_{43}$ gas phase cluster at the critical hydrogen coverage, $n_H = 80$.*

respectively.

The differential Gibbs free energy of H adsorption (ΔG_{diff}) is presented as a function of the number of hydrogen atoms (n_H) in Figure 7.5 for the values presented in Tables 7.2 and 7.3 (n_H = 1–7 and 73–81). The dotted horizontal line at $\Delta G_{diff} = 0$ corresponds to the thermoneutral H adsorption, whereas the most optimal region

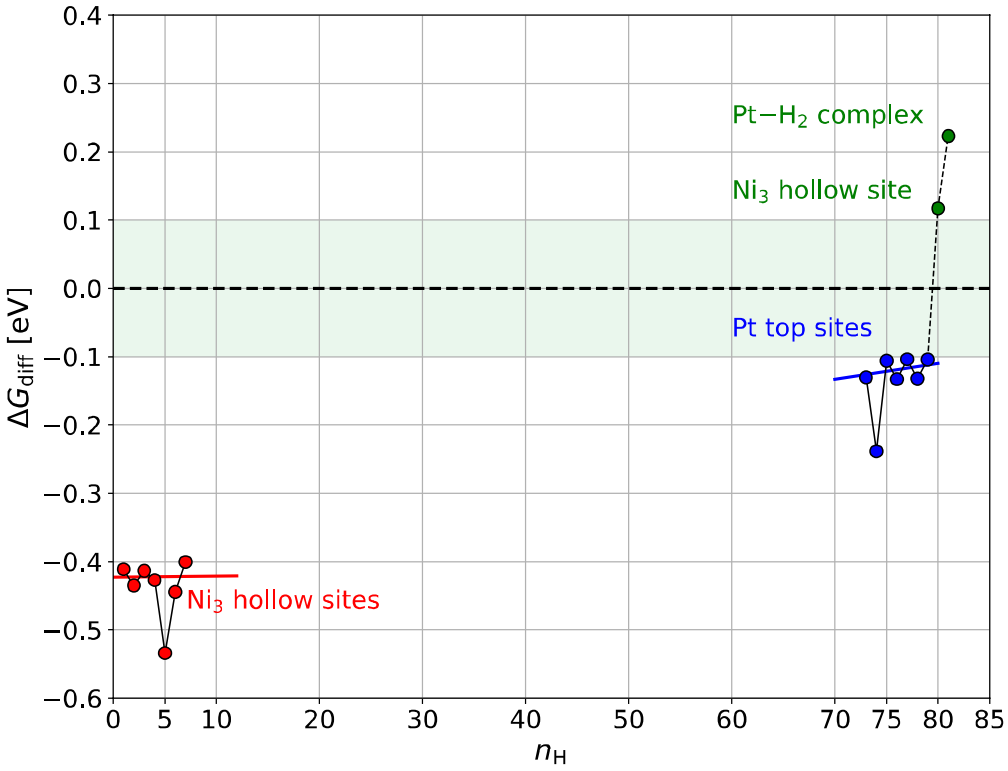

Figure 7.5 *The differential Gibbs free energy of hydrogen adsorption (ΔG_{diff}) as a function of the number of H atoms (n_{H}) adsorbed on the $Pt_{12}Ni_{43}$ cluster in the gas phase. The corresponding values are presented in Tables 7.2 and 7.3. The dotted horizontal line at $\Delta G_{\text{diff}} = 0$ corresponds to the thermoneutral H adsorption. The most optimal region in terms of catalytic activity, $|\Delta G_{\text{diff}}| < 0.1$ eV, is highlighted with the light green color. The data points are connected with the solid (dashed) lines, when the hydrogen adsorption is exergonic (endergonic). The three distinguishable regions of H adsorption are emphasized with different colors. At low coverages (red region), Ni_3 hollow sites are favorable for H adsorption. Near the critical coverage (blue region), H atoms mostly prefer Pt top sites, but also Ni_3 hollow sites in the case of $n_{\text{H}} = 73$ and 79. Green color represents H coverages, where ΔG_{diff} is positive. Simple linear models were fitted to the data points at low (red) and high (blue) coverage regions. Values for $n_{\text{H}} = 5$ and $n_{\text{H}} = 74$ were ignored, because they are clearly different from the rest of the data points.*

in terms of catalytic activity, $|\Delta G_{\text{diff}}| < 0.1$ eV, is highlighted with the light green color. Figure 7.5 has three distinguishable regions; the low coverage region ($n_{\text{H}} = 1$–7), the high coverage region ($n_{\text{H}} = 73$–79), and the endergonic ($\Delta G_{\text{diff}} > 0$) region ($n_{\text{H}} = 80$–81), which are emphasized with red, blue, and green color, respectively. The low coverage region (red) was already discussed in the previous section. The regions near the critical coverage (blue and green) will be discussed below. The H coverages $n_{\text{H}} = 8$–72 were not studied in this work.

The most stable configuration for the hydrogen coverage $n_{\text{H}} = 79$ was discovered, when an H atom was removed from a Ni_3 hollow site in the ground-state $n_{\text{H}} = 80$

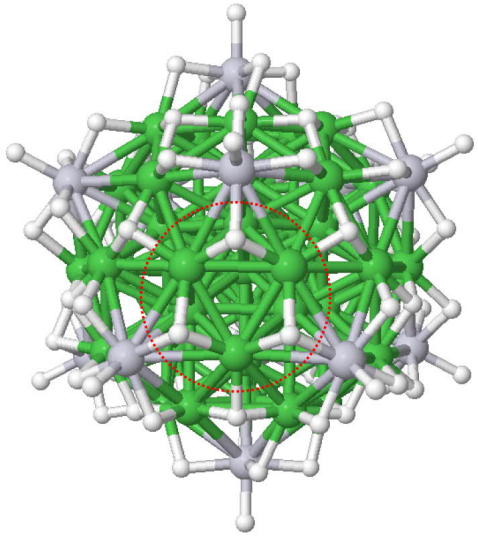

(a) 79 H atoms: an empty Ni_3 hollow site, neighbored by three occupied Pt-Ni_2 hollow sites.

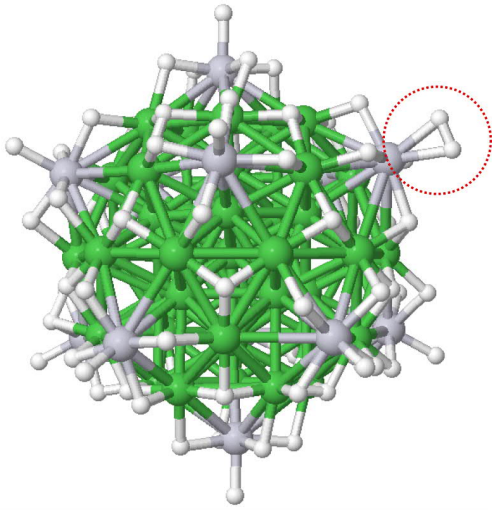

(b) 81 H atoms: Pt-H_2 complex.

Figure 7.6 *The ground-state configurations of $Pt_{12}Ni_{43}$ gas phase cluster with hydrogen coverage consisting of 79 H and 81 H atoms.*

structure, which is shown in Figure 7.3. Therefore, the 80th H atom preferentially adsorbs on an empty Ni_3 hollow site, shown in Figure 7.6(a), which represents the ground-state $n_H = 79$ structure. The 79th and 73rd H atoms also prefer to adsorb on empty Ni_3 hollow sites. For $n_H = 73$, 79, and 80, the Ni_3 hollow sites are 0.11–0.32 eV lower in energy than Pt top sites. When a Ni_3 hollow site is empty, the three nearby H atoms occupy the Pt-Ni_2 hollow sites instead of Pt-Ni bridge sites, as seen in Figure 7.6(a). When the Ni_3 hollow site is occupied, the H atoms have translated from the Pt-Ni_2 hollow sites to the Pt-Ni bridge sites, as in Figures 7.3(a) and 7.6(b). Although the Ni_3 hollow sites are occupied at low coverages ($n_H = 1$–7), it seems that at an unknown coverage between $n_H = 8$ and 72, the Ni_3 hollow sites become unfavorable and empty until a high enough coverage is reached, and H atoms start to occupy them again.

While 73rd, 79th, and 80th H atoms prefer empty Ni_3 hollow sites, for $n_H = 74$–78 coverages the H atoms prefer to occupy empty Pt top sites, as listed in Table 7.3. For example for the 78th adsorbed H atom, the ground-state energy on a Pt top site is 0.06 eV lower than on a Ni_3 hollow site. When an H atom adsorbs on a Pt top site, the rest of the system remains structurally intact.

The hydrogen adsorption is endergonic ($\Delta G_{diff} > 0$) for the adsorption of the 80th and 81st H atoms. The adsorption of the 80th H atom on the empty Ni_3 hollow site

in Figure 7.6(a) causes a considerable jump, 0.22 eV, in the adsorption energy, as seen in Figure 7.5. The $Pt_{12}Ni_{43}$ cluster with the coverage of 80 H atoms (Figure 7.3) has various sites free for the adsorption of the 81st H atom; Pt-Ni bridge sites (one per Pt atom), Ni top sites, and Pt-Ni_2 hollow sites. The adsorption of two H atoms on a single Pt top site was also considered. The initial and relaxed adsorption sites of the 81st H atom, the adsorption energies, and the energy differences to the most stable $n_H = 81$ configuration are collected in Table 7.4.

Table 7.4 *$Pt_{12}Ni_{43}$ in the gas phase with 81 H atoms: sites of the 81st adsorbed H atom before and after geometry relaxation. Pt-H_2 or Ni-H_2 complex refers to a hydrogen molecule, H_2, that is adsorbed on a Pt or Ni top site, respectively. The ΔG_{diff} values were calculated using Eq. (4.9) and ΔE is the energy difference to the ground-state configuration. Pt-H_2 complex has the lowest energy and is thus the most favorable adsorption site for the 81st H atom. Its adsorption energy is positive, $\Delta G_{diff} = 0.22$ eV, meaning that the critical coverage has been surpassed and the adsorption is endergonic.*

Initial site	Relaxed site	ΔG_{diff} [eV]	ΔE [eV]
Pt top (H_2)	Pt-H_2 complex	0.22	0.00 (the ground-state)
Ni top	Ni-H_2 complex	0.36	0.14
Pt-Ni bridge	Pt-Ni bridge	0.49	0.27
Pt-Ni_2 hollow	Pt-Ni bridge	0.49	0.27

The 81st H atom prefers to adsorb on a Pt top site. Because all Pt top sites are already occupied by one H atom each, one Pt top site becomes occupied with two H atoms, which form a hydrogen molecule (H_2). The molecule on a Pt top site is referred to as a Pt-H_2 complex. The ground-state $n_H = 81$ structure is presented in 7.6(b). Besides the Pt-H_2 complex, the ground-state structures with 80 and 81 H atoms (Figures 7.3 and 7.6(b), respectively) are identical. In the Pt-H_2 complex, the H-H bond length is 0.87 Å and both Pt-H bonds have equal length of 1.77 Å.

The hydrogen adsorbed on a Ni top site forms a Ni-H_2 complex, which is 0.14 eV higher in energy compared to the Pt-H_2 complex. The bonds in the Ni-H_2 complex are shorter than in the Pt-H_2 complex; the H-H and Pt-H bond lengths are 0.82 Å and 1.72 Å in the Ni-H_2 complex, respectively. Both complexes represent the Heyrovsky step in HER: an H atom binds to an already adsorbed hydrogen atom to form an adsorbed H_2 molecule. Similar endergonic formation of an H_2 molecule on a top site was observed by Wexler *et al.* [24], who reported a Ni-H_2 complex to form, when the critical coverage was reached on the Ni_5P_4 surface (see Figure 4.5). They also reported the critical coverage to cause a large jump in ΔG_{diff}, which was observed in this work as well, although the studied systems are different.

7.1.3 Analysis of Structural Properties and Charge Transfer

To analyze how the hydrogen coverage affects the icosahedral structure and bond lengths of $Pt_{12}Ni_{43}$, the radial distribution functions were calculated at the critical coverage The RDF figures can be found in Appendix B. RDFs for Pt-Pt, Ni-Ni, and Ni-Pt have the same shape with and without the hydrogen coverage (Figure 6.9(a)), however, all peaks shift to larger distances with the coverage. Therefore, the hydrogen coverage causes the cluster to expand, but it retains its icosahedral shape.

The cluster diameter and the average bond lengths between different atom pairs are presented in Table 7.5 with and without the hydrogen coverage of 80 H atoms. The coverage lengthens Ni-Ni and Ni-Pt bonds; 2.46 Å → 2.52 Å and 2.55 Å → 2.66 Å, respectively. The diameter of the cluster also increases by 0.42 Å, from 9.68 Å to 10.10 Å. The maximum diameter of the hydrogen coverage is 13.25 Å, which is the distance between two H atoms on Pt top sites, which are in the opposite sides of the cluster. The average bond lengths of Pt-H and Ni-H are 1.68 Å and 1.72, respectively. The H atoms on Pt-Ni bridge sites have Pt-H bond length of 1.69–1.70 Å and Ni-H bond length of 1.72–1.81 Å. The H atoms on Pt top sites have Pt-H bond length of 1.58 Å. For Ni_3 hollow sites the Ni-H bond lengths are 1.65–1.69 Å. The first H-H RDF peak (2.24 Å) does not represent a bond, because H atoms do not form bonds with each other and the system contains no H_2 at the critical coverage.

Table 7.5 *The cluster diameter and the average bond lengths r_{ave} between different atom pairs for the $Pt_{12}Ni_{43}$ cluster in the gas phase with and without hydrogen coverage of 80 H atoms (the critical coverage). The corresponding structures are shown in Figures 6.6 and 7.3, respectively. The values for the uncovered cluster are from Table 6.1. The average bond length is defined as the location of the first RDF peak. The systems have no Pt-Pt bonds nor H-H bonds. Cluster diameter is equal to the location of the last RDF peak.*

	$Pt_{12}Ni_{43}$	$Pt_{12}Ni_{43}$ + 80 H
r_{ave} (Ni-Ni) [Å]	2.46	2.52
r_{ave} (Ni-Pt) [Å]	2.55	2.66
r_{ave} (Pt-Pt) [Å]	–	–
r_{ave} (Pt-H) [Å]	–	1.68
r_{ave} (Ni-H) [Å]	–	1.72
r_{ave} (H-H) [Å]	–	–
Cluster diameter [Å]	9.68	10.10 (with H: 13.25)

Bader analysis was performed for the $Pt_{12}Ni_{43}$ cluster with the critical hydrogen coverage ($n_H = 80$). The hydrogen atoms carry a charge of $+0.10e$/atom. At high coverages, the Coulomb repulsion between the positively charged hydrogen atoms

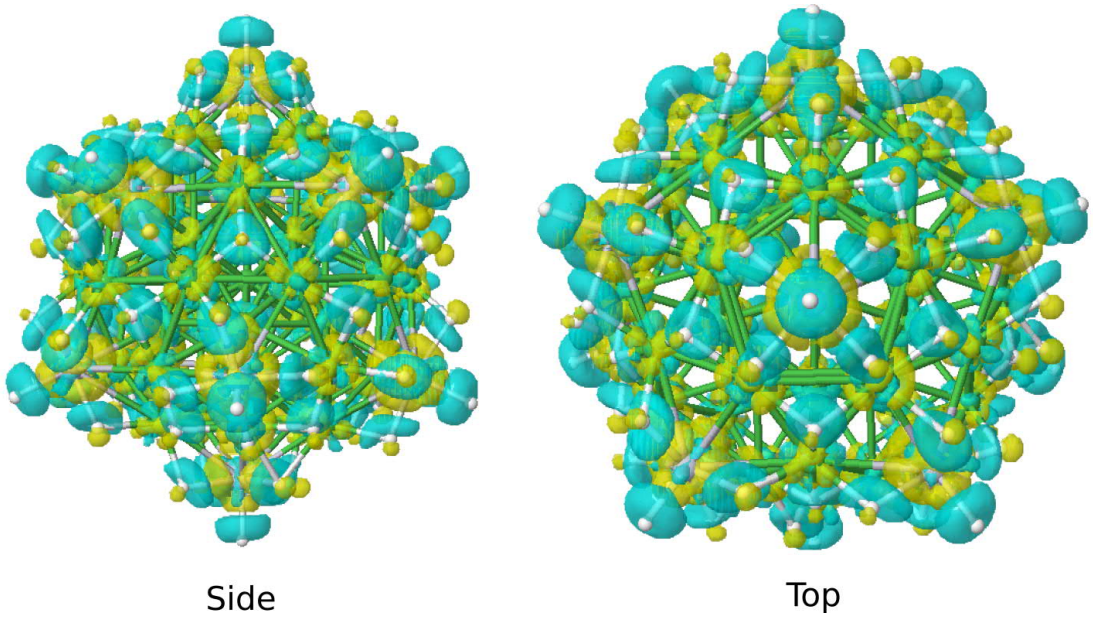

Figure 7.7 *Side and top views of the charge density difference (CDD) for the $Pt_{12}Ni_{43}$ cluster with the hydrogen coverage consisting of 80 H atoms. The corresponding structure is shown in Figure 7.3. The yellow and cyan colors represent charge accumulation and depletion, respectively. The cluster (Ni and Pt atoms) accumulates a net charge of $-7.67e$ from the hydrogen coverage. Each H atoms carries a charge of $+0.10e$/atom. The isosurface values are* $0.007\ \pm e/\mathrm{a}_0^3$.

affects to the structure of the hydrogen coverage. The charge transfers, calculated with Eq. (5.43), are $-0.08e$, $-0.37e$, and $+0.10e$ per atom for Ni, Pt, and H atoms, respectively. Therefore, both Ni and Pt atoms accumulate charge from the hydrogen atoms. This is illustrated in Figure 7.7, which shows the charge density difference for the system. The charge depletion (cyan) occurs around hydrogen atoms, whereas Ni and Pt atoms on the surface accumulate charge (yellow).

7.2 Hydrogen Adsorption on $Pt_{12}Ni_{43}$ on the Al_2O_3 Support

This section is divided into two subsections. The first subsection discusses the hydrogen adsorption mechanisms at different coverages, whereas the charge transfer and the effect of a high hydrogen coverage on the properties of the cluster are analyzed in the second subsection.

7.2.1 Hydrogen Adsorption at Different Coverages

The hydrogen adsorption for the $Pt_{12}Ni_{43}$ cluster on the alumina support was studied in the same manner as previously. The six types of adsorption sites illustrated

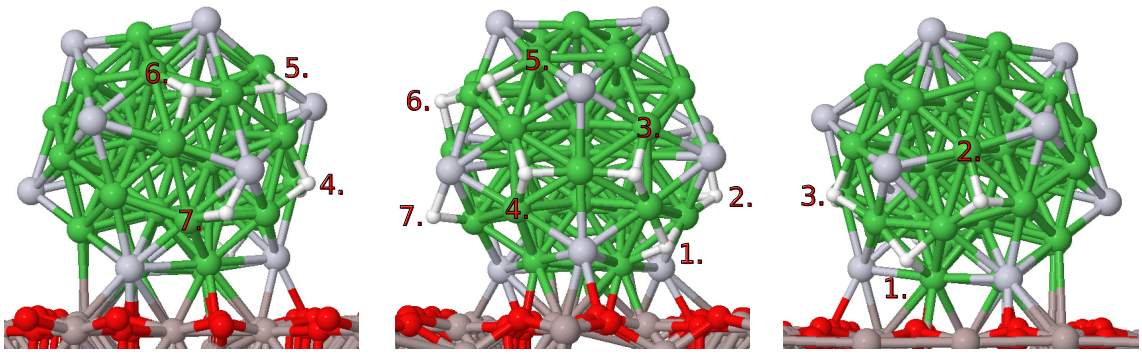

Figure 7.8 *The relaxed $Pt_{12}Ni_{43}$ cluster on the Al_2O_3 support with the hydrogen coverage consisting of 7 H atoms, shown from three different angles. The numbers represent the order in which the H atoms are adsorbed. The first 6 H atoms adsorb on Ni_3 hollow sites, whereas the 7th H atom adsorbs on a Pt-Ni bridge site.*

in Figure 7.1 were considered; Pt top, Ni top, Pt-Ni bridge, Ni-Ni bridge, Ni_3 hollow, and Pt-Ni_2 hollow sites. Pt top and Ni top sited were ignored at low H coverages, because the gas phase calculations indicated that they are unfavorable for H adsorption. For each n_H, the adsorption sites were sampled using approximately 30–40 initial H atom positions, including the gas phase ground-state configurations. The differential Gibbs free energies, ΔG_{diff}, were calculated using Equations (4.9) and (4.10).

The adsorption of one hydrogen atom is similar on the support and in the gas phase. A Ni_3 hollow site is the preferred adsorption site with $\Delta G_{diff} = -0.43$ eV on the support and -0.41 eV in the gas phase. A Pt-Ni_2 hollow site is only 0.03 eV (0.07 eV) higher in energy than the Ni_3 hollow site on the support (in the gas phase). Different Ni_3 hollow sites around the cluster were tested, and a hollow site next to the support was found to be the most stable.

The hydrogen atoms 1–6 prefer to adsorb on Ni_3 hollow sites, whereas the 7th H atom is an exception and prefers a Pt-Ni bridge site. The adsorption energies at coverages $n_H = 1$–7 on the support are between -0.41 eV and -0.46 eV, thus they differ negligibly from the corresponding gas phase values, which are between -0.40 eV and -0.44 eV. The ground-state of $Pt_{12}Ni_{43}$ with 7 adsorbed H atoms is presented in Figure 7.8. The ground-state configurations for $n_H = 4$–7 are not exactly the same as in the gas phase (Figure 7.2). Nevertheless, the adsorption behavior at low H coverages is similar on the support.

Because the adsorbed $Pt_{12}Ni_{43}$ cluster has one facet towards the support, the coverages consisting of 66–73 H atoms were sampled instead of $n_H = 73$–81, which were considered in the gas phase. Each n_H was sampled with 30-40 initial hydrogen cov-

erage configurations. The ΔG_{diff} values for the discovered $n_{\text{H}} = 66$–73 ground-state structures are presented in Table 7.6. On the support, the differential adsorption energy changes its sign from negative to positive between $n_{\text{H}} = 70$ and 71. Therefore, the critical coverage, $n_{\text{H}} = 71$, is lower compared to the gas phase, where it is $n_{\text{H}} = 80$. The reason for the lower critical coverage on the support is that the cluster has less adsorption sites available in the first place.

Table 7.6 *The differential Gibbs free energies of adsorption for* 66–73 *H atoms adsorbed on the $Pt_{12}Ni_{43}$ cluster on the Al_2O_3 support. Calculated with Eq.* (4.9)*. Adsorption site describes the site where the last H atom is adsorbed.*

n_{H}	ΔG_{diff} [eV]	Adsorption site
66	−0.15	Pt top
67	−0.13	Ni_3 hollow
68	−0.10	Pt top
69	−0.08	Ni_3 hollow
70	−0.15	Ni_3 hollow
71	0.00	Ni_3 hollow (critical coverage)
72	0.01	Ni_3 hollow
73	0.21	Ni_3 hollow

In the same manner as for the gas phase cluster, the ΔG_{diff} values on the support are presented as a function of n_{H} in Figure 7.9 for $n_{\text{H}} = 1$–7 and 66–73. The three distinguishable regions are observed, similar to the gas phase results: the low coverage region ($n_{\text{H}} = 1$–7), the high coverage region ($n_{\text{H}} = 66$–70), and the endergonic ($\Delta G_{\text{diff}} > 0$) region ($n_{\text{H}} = 71$–73), which are emphasized with red, blue, and green color, respectively. The low coverage region (red) is coherent and the Ni_3 hollow sites are the strongly binding sites, as mentioned above. The regions near the critical coverage (blue and green) will be discussed below.

The same two mechanisms are observed at high coverages as in the gas phase; hydrogen atoms adsorb either on empty Ni_3 hollow sites or Pt top sites. The adsorption on Pt top sites does not affect the other H atoms in the coverage, but the adsorption on a Ni_3 hollow site changes the configuration of other nearby H atoms. Before the adsorption of an H atom on a Ni_3 hollow site, the three nearby H atoms are on the Pt-Ni_2 hollow sites (see Figure 7.6(a)), but after the adsorption the three H atoms move to the Pt-Ni bridge sites.

In the gas phase, the Pt top sites were more often the favorable sites than Ni_3 hollow sites at the studied high hydrogen coverages. However, on the support the opposite behavior is observed. Ni_3 hollow sites are preferable for the adsorption at $n_{\text{H}} = 67$ and 69–73 coverages, while only the 66th and 68th H atoms prefer Pt top sites, as

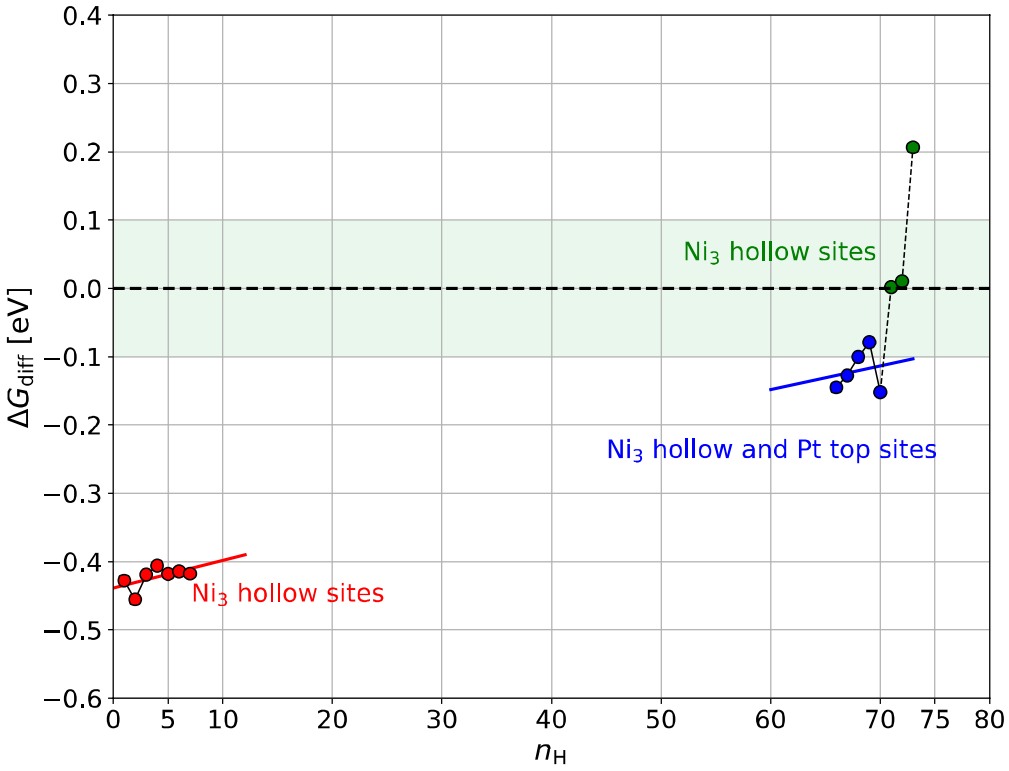

Figure 7.9 *The differential Gibbs free energy of hydrogen adsorption (ΔG_{diff}) as a function of the number of H atoms (n_H) adsorbed on the $Pt_{12}Ni_{43}$ cluster on the Al_2O_3 support. The corresponding values are values for n_H = 66–73 presented in Table 7.6. The dotted horizontal line at $\Delta G_{diff} = 0$ corresponds to the thermoneutral H adsorption. The most optimal region in terms of catalytic activity, $|\Delta G_{diff}| < 0.1$ eV, is highlighted with the light green color. The data points are connected with the solid (dashed) lines, when the hydrogen adsorption is exergonic (endergonic). The three distinguishable regions of H adsorption are emphasized with different colors. At low coverages (red region), Ni_3 hollow sites are favorable for H adsorption. Near the critical coverage (blue region), H atoms prefer either Ni_3 hollow sites (n_H = 67, 69, and 70) or Pt top sites (n_H = 66 and 68). Green color represents H coverages, where ΔG_{diff} is positive (n_H = 71–73) and Ni_3 hollow sites are favorable for H adsorption. Simple linear models were fitted to the data points at low (red) and high (blue) coverage regions.*

listed in Table 7.6.

The ground-state structure with $n_H = 73$ is shown in Figure 7.10. Besides the unavailable facet, the hydrogen coverage is similar to the critical coverage structure in the gas phase ($n_H = 80$), shown in Figure 7.3. All Ni_3 hollow and Pt top sites are occupied by H atoms, and 4 out of 5 Pt-Ni bridge sites around each Pt atom are occupied. However, on the support the hydrogen adsorption for this coverage is endergonic ($\Delta G_{diff} = 0.21$ eV). The H adsorption is endergonic also for the 71st and 72nd H atom. At the endergonic coverages, n_H = 71–73, Ni_3 hollow sites are favorable adsorption sites. The formation of a Pt-H_2 complex, which was observed in

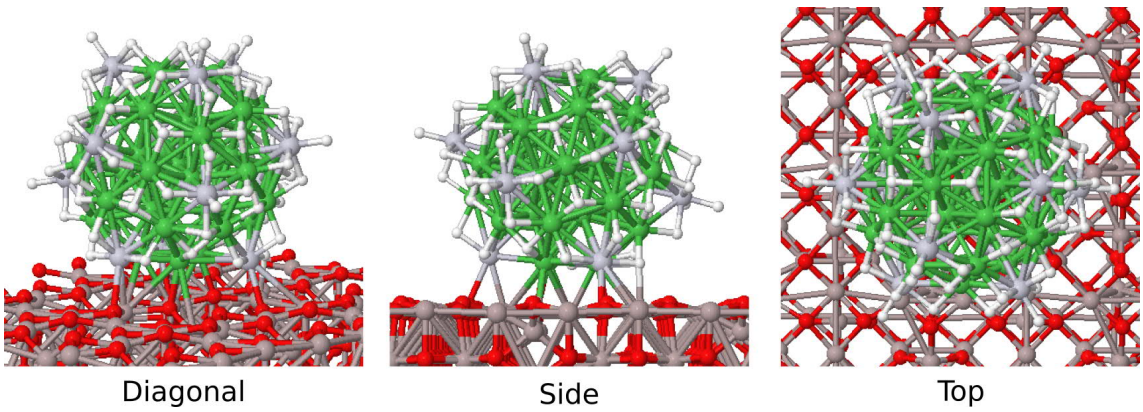

Figure 7.10 *The $Pt_{12}Ni_{43}$ cluster on the Al_2O_3 support with the hydrogen coverage, which consists of 73 H atoms, shown from three different angles. H atoms occupy all Ni_3 hollow and Pt top sites, whereas 4 out of 5 Pt-Ni bridge sites around each Pt atom are occupied. The hydrogen coverage is similar to the $n_H = 80$ coverage in the gas phase, shown in Figure 7.3.*

the gas phase at $n_H = 81$, is not favorable at any sampled coverage on the alumina support, because there are empty Ni_3 hollow sites available until the last one is occupied at $n_H = 73$.

The behavior when the critical coverage is reached is similar in the gas phase and on the support. The critical coverage in both cases is caused by the adsorption of an H atom on a Ni_3 hollow site. This causes a considerable jump in ΔG_{diff}, as can be seen in Figures 7.5 and 7.9. The jump is larger in the gas phase (0.22 eV) than on the support (0.15 eV). On the support, ΔG_{diff} at $n_H = 71$ is positive but very small and rounds to 0.00 eV, which corresponds to thermoneutral hydrogen adsorption. While the adsorption of the 72nd H atom on the support changes ΔG_{diff} negligibly, the adsorption of the 73rd H atom causes a second large jump of 0.20 eV in ΔG_{diff}. The jumps caused by the adsorption of the 80th H atom in the gas phase (0.22 eV) and the 73rd H atom on the support (0.20 eV) are nearly equal. The structures of the hydrogen coverage in the two cases are very similar, as all available Ni_3 hollow sites and Pt top sites have been occupied.

7.2.2 Analysis of Structural Properties and Charge Transfer

Similarly to the gas phase cluster, the radial distribution functions were calculated for all atoms pairs in the adsorbed cluster with the hydrogen coverage of 73 H atoms, because this coverage on the support is similar to the $n_H = 80$ coverage in the gas phase. They do not noticeably differ from RDFs calculated in the gas phase (see Appendix B). Therefore, the high hydrogen coverage has the same effect on

the $Pt_{12}Ni_{43}$ cluster, regardless of the alumina support; the cluster expands but it retains its icosahedral shape.

The high hydrogen coverage ($n_H = 73$) causes the cluster to shift a small distance away from the surface. The center Ni atom of the cluster is 0.07 Å further away from the alumina surface compared to the uncovered cluster. The range of bond lengths for the adsorption facet of the supported $Pt_{12}Ni_{43}$ cluster are shown in Table 7.7 with and without the hydrogen coverage. With the coverage, the cluster is adsorbed on the alumina with 6 Pt-Al bonds, 3 Pt-O bonds, 8 Ni-Al bonds, and 3 Ni-O bonds. The corresponding average bond lengths are 3.00 Å, 2.35 Å, 3.01 Å, and 2.09 Å, respectively. The presence of the hydrogen coverage causes all average bond lengths to increase by 0.10–0.13 Å. One Pt-Al bond (3.30 Å) and one Ni-Al bond (3.22 Å) become rather long, 3.42 Å and 3.37 Å, respectively, and are interpreted as broken bonds.

Table 7.7 *The range of bond lengths of the $Pt_{12}Ni_{43}$ cluster adsorbed on the Al_2O_3 support uncovered and with the hydrogen coverage consisting of 73 H atoms. The corresponding structures without and with the coverage are shown in Figures 6.11 and 7.10, respectively. The range of bond lengths without the H coverage are from Table 6.2. The average bond lengths are in brackets.*

	Uncovered cluster	The coverage of 73 H atoms
R_{Pt-Al} [Å]	2.55–3.30 (2.90)	2.63–3.42 (3.00)
R_{Pt-O} [Å]	2.18–2.27 (2.22)	2.31–2.42 (2.35)
R_{Ni-Al} [Å]	2.50–3.29 (2.90)	2.62–3.37 (3.01)
R_{Ni-O} [Å]	1.97–2.04 (1.99)	2.06–2.11 (2.09)

Bader charge analysis was performed for $Pt_{12}Ni_{43}$ on Al_2O_3 with 73 adsorbed H atoms. The 73 H atoms carry a net charge of $+0.10e$/atom, which is equal to the value obtained in the gas phase. The effective charges, calculated with Eq. (5.43), for Ni, Pt, and H atoms are $-0.07e$, $-0.36e$, and $+0.10e$ per atom, respectively. Ni and Pt atoms accumulated charge from the hydrogen atoms, but slightly less than in the gas phase, where Ni and Pt atoms accumulated $-0.08e$ and $-0.37e$ per atom, respectively.

7.3 Pt-Ni Nanoclusters as HER Catalysts: Summary

The calculated ΔG_{diff} values for $Pt_{12}Ni_{43}$ (in the gas phase/on Al_2O_3) and $Pt_{20}Ni_{35}$ (in the gas phase) are presented together in Figure 7.11 as a function of the number of H atoms. The hydrogen coverages were sampled for the $Pt_{20}Ni_{35}$ cluster in the gas phase in the same manner as for the $Pt_{12}Ni_{43}$ cluster. Appendix C contains the ΔG_{diff} values and the ΔG_{diff} plot separately for $Pt_{20}Ni_{35}$.

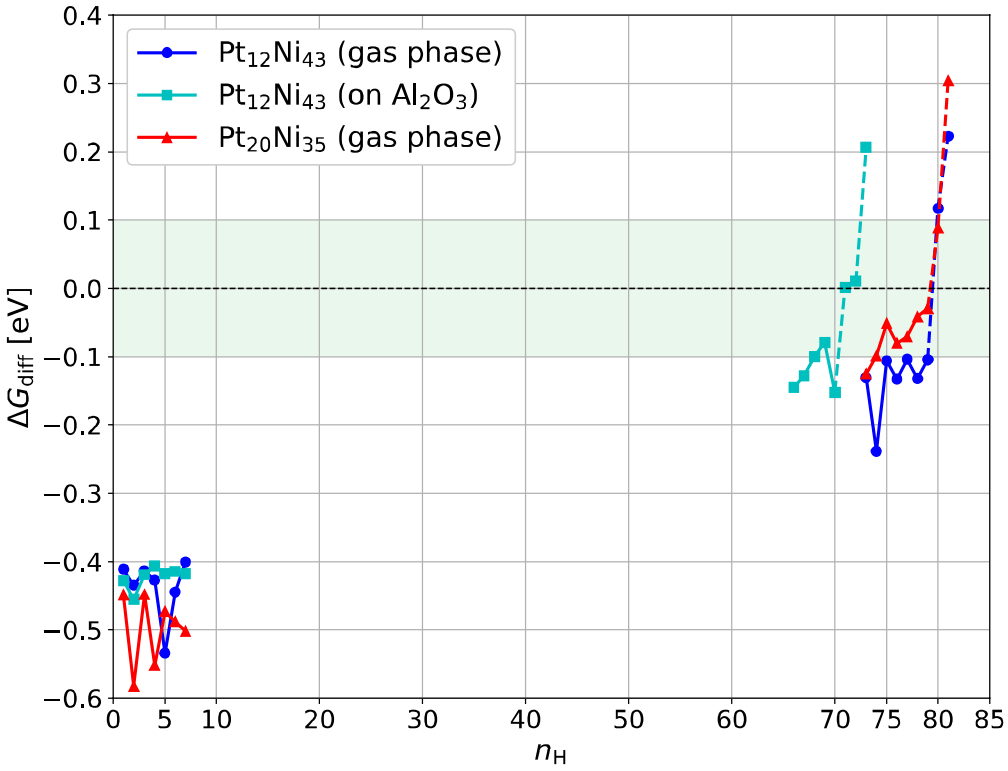

Figure 7.11 *The differential Gibbs free energy of hydrogen adsorption (ΔG_{diff}) as a function of the number of H atoms (n_{H}) adsorbed on the $Pt_{12}Ni_{43}$ and $Pt_{20}Ni_{35}$ clusters in the gas phase, and $Pt_{12}Ni_{43}$ on the Al_2O_3 support. The respective plots are presented individually for $Pt_{12}Ni_{43}$ in the gas phase in Figures 7.5, $Pt_{12}Ni_{43}$ on Al_2O_3 in Figure 7.9, and $Pt_{20}Ni_{35}$ in the gas phase in Appendix C. The dotted horizontal line at $\Delta G_{\text{diff}} = 0$ corresponds to the thermoneutral H adsorption. The most optimal region in terms of catalytic activity, $|\Delta G_{\text{diff}}| < 0.1$ eV, is highlighted with the light green color. The data points are connected with the solid (dashed) lines, when the hydrogen adsorption is exergonic (endergonic). On the support, the critical coverage is lower compared to the gas phase. For $Pt_{12}Ni_{43}$ in the gas phase, the adsorption energy jumps over the catalytically optimal region, while it is approximately thermoneutral on the support.*

At low H coverages on $Pt_{20}Ni_{35}$, an odd-even variation is observed in the ΔG_{diff} values, which are between −0.45 eV and −0.58 eV for $n_{\text{H}} = 1$–7. Odd H atoms prefer to occupy Ni_3 hollow sites. At even n_{H}, H atoms form pairs, which occupy bridge and Pt-Ni_2 hollow sites, similarly to the 4th and 5th H atoms in Figure 7.2, and there are no H atoms on Ni_3 hollow sites. The critical coverage is $n_{\text{H}} = 80$, which is equal to the critical coverage of $Pt_{12}Ni_{43}$ in the gas phase. At $n_{\text{H}} = 73$–76, H atoms occupy Pt top sites. $Pt_{20}Ni_{35}$ has only 4 Ni_3 hollow sites, which are occupied at $n_{\text{H}} = 77$–80. The 81st H atom adsorbs on an occupied Pt top site and forms a Pt-H_2 complex, similarly to $Pt_{12}Ni_{43}$ in the gas phase. A jump of 0.12 eV is observed in ΔG_{diff} when the critical coverage is reached, and another larger jump of 0.21 eV occurs when the 81st H atom adsorbs and forms the Pt-H_2 complex.

Both $Pt_{12}Ni_{43}$ and $Pt_{20}Ni_{35}$ clusters adsorb a considerable number of hydrogen atoms; the critical coverages are $n_H = 80$ in the gas phase for both clusters, and $n_H = 71$ for $Pt_{12}Ni_{43}$ on the Al_2O_3 support. In the gas phase and on the support, the number of H atoms adsorbed per facet are $80/20 = 4$ and $71/19 \approx 3.74$, respectively. For $Pt_{12}Ni_{43}$, the hydrogen adsorption mechanisms are similar in the gas phase and on the alumina support; Ni_3 hollow sites are favorable at low coverages, whereas both Ni_3 hollow and Pt top sites are occupied at high coverages. Therefore, the support does not significantly change the preferred adsorption sites. The lower critical coverage for the adsorbed cluster is explained by smaller number of available adsorption sites due to one cluster facet being against the support.

Table 7.8 *The hydrogen adsorption free energies, ΔG_{H^*}, for the $Pt_{12}Ni_{43}$ and $Pt_{20}Ni_{35}$ nanoclusters in the gas phase, and for $Pt_{12}Ni_{43}$ on the Al_2O_3 support. The adsorption free energy for $Pt_{20}Ni_{35}$ on Al_2O_3 was not calculated.*

	Gas phase	On Al_2O_3
$Pt_{12}Ni_{43}$	−0.10 eV	0.00 eV
$Pt_{20}Ni_{35}$	−0.03 eV	Not calculated

The free energies of hydrogen adsorption, ΔG_{H^*}, for the $Pt_{12}Ni_{43}$ and $Pt_{20}Ni_{35}$ clusters are presented in Table 7.8. The obtained ΔG_{H^*} descriptor values are close to zero, which indicates that both clusters, $Pt_{12}Ni_{43}$ and $Pt_{20}Ni_{35}$, are active towards the hydrogen evolution reaction. This is based on the assumption that the closer ΔG_{H^*} is to zero, the better the HER activity. The support has a considerable effect on ΔG_{H^*}, since ΔG_{H^*} for $Pt_{12}Ni_{43}$ is approximately thermoneutral on the support, while in the gas phase it is −0.10 eV. Therefore, the alumina support improves the HER activity of $Pt_{12}Ni_{43}$, which is beneficial, because in experiments and practical applications NPs are deposited on a support.

8. CONCLUSIONS

The development of affordable and earth-abundant electrocatalysts for the hydrogen evolution reaction is essential, because the effective production of molecular hydrogen could provide a practical solution to the energy storage problem of renewable energy. Reducing the amount of Pt required in HER catalysts is one approach to this issue. In the present work, density functional theory calculations were performed on small 55-atom Pt-Ni nanoclusters to study their activity towards HER. All DFT calculations were carried out using the CP2K software package [18]. The free energy of hydrogen adsorption, ΔG_{H^*}, was used as a descriptor to estimate the HER activity of the clusters. This descriptor-based approach has previously been successful in predicting the activity of different materials, such as MoS_2 [28], transition metal phosphides [47], and bimetallic surfaces [42].

Before studying the hydrogen adsorption on the Pt-Ni clusters, the structures reported in the literature for Ni_{55}, Pt_{55}, and different Pt_nNi_{55-n} compositions were reproduced. The most stable Ni_{55} and Pt_{55} structures were icosahedral and disordered reduced-core structure, respectively. This is consistent with the ground-state structures reported in the literature [12, 117, 119, 120, 123]. The default multiplicity value was used, which resulted in both clusters having a zero magnetic moment. In the literature, the total magnetic moment of Pt_{55} is reported to be zero [117], whereas Ni_{55} is known to be highly magnetic with the total magnetic moment of 40 μ_{B} (0.73 μ_{B} per atom) [117, 120]. The calculated projected density of states revealed that the Ni_{55} and Pt_{55} clusters have no band gap and the d-band of Pt_{55} is noticeably wider compared to the Ni_{55} cluster.

Bimetallic Pt_nNi_{55-n} clusters of various compositions were studied based on the ground-state structures of the pure Ni_{55} and Pt_{55}, and the Pt-Ni cluster structures reported by Guedes-Sobrinho *et al.* [12]. Based on the calculated excess energies, the formation of the bimetallic clusters was found to be energetically favorable for all compositions, which was also reported by Guedes-Sobrinho *et al.* [12]. The $Pt_{12}Ni_{43}$ and $Pt_{20}Ni_{35}$ clusters were chosen for the hydrogen adsorption study. They are icosahedral clusters, similarly to Ni_{55}. The diameters of the Pt-Ni clusters are close to one nanometer; $Pt_{12}Ni_{43}$ and $Pt_{20}Ni_{35}$ have diameters of 9.68 Å and 9.80 Å,

respectively.

$Pt_{12}Ni_{43}$ and $Pt_{20}Ni_{35}$ were aligned on a γ-Al_2O_3 support, where they retained their icosahedral structure. The adsorption energies of $Pt_{12}Ni_{43}$ and $Pt_{20}Ni_{35}$ adsorbed on the support were 7.18 eV and 7.47 eV, respectively. The preferred adsorption orientation for $Pt_{12}Ni_{43}$ was to have one of its facets against the support, whereas $Pt_{20}Ni_{35}$ behaved differently and preferred a more tilted orientation. The charge density difference indicated that a significant accumulation and depletion of charge occurred at the interface between each cluster and the support. Bader charge analysis suggested that the support donates $0.72e$ and $1.01e$ of electron density to the adsorbed $Pt_{12}Ni_{43}$ and $Pt_{20}Ni_{35}$ clusters, respectively. The *d*-states were observed to contribute significantly to the density of states of the Pt and Ni atoms of the adsorbed clusters, which along with the negatively charged clusters is a promising indicator of the interaction with reactant molecules and catalytic activity [126].

In order to determine the ΔG_{H^*} descriptor values, the critical hydrogen coverages were searched by sampling different hydrogen coverages for $Pt_{12}Ni_{43}$ and $Pt_{20}Ni_{35}$ in the gas phase, and for $Pt_{12}Ni_{43}$ on the Al_2O_3 support. Ni_3 hollow sites were discovered to be the strongly binding sites for hydrogen adsorption in all studied systems. The differential free energies of hydrogen adsorption, ΔG_{diff}, for the adsorption of a single H atom were -0.41 eV, -0.43 eV, and -0.45 eV for $Pt_{12}Ni_{43}$ in the gas phase, $Pt_{12}Ni_{43}$ on the support, and $Pt_{20}Ni_{35}$ in the gas phase, respectively. Kristinsdóttir and Skúlason [89] reported the adsorption energy of an H atom on both Ni(111) and Pt(111) hollow sites to be -0.37 eV, whereas Wexler *et al.* [24] reported that Ni_3 hollow sites on the Ni_3P_2 surface are the strongly binding sites with $\Delta G_{\text{diff}} = -0.47$ eV. These reported values are close to the ΔG_{diff} values obtained in this work, despite the systems being different.

At low hydrogen coverages with 1–7 adsorbed H atoms, the calculated ΔG_{diff} values were considerably negative and they varied between -0.41 eV and -0.58 eV for all three studied systems. For $Pt_{12}Ni_{43}$ in the gas phase and on the support, Ni_3 hollow sites and Pt-Ni bridge sites were favorable for hydrogen adsorption at the low coverages. For $Pt_{20}Ni_{35}$ in the gas phase, an odd-even variation was discovered in the ΔG_{diff} values and the favorable adsorption sites. Odd H atoms preferred to occupy Ni_3 hollow sites. When the number of H atoms was even, the H atoms formed pairs, which occupied neighboring bridge and Pt-Ni_2 hollow sites.

For both $Pt_{12}Ni_{43}$ and $Pt_{20}Ni_{35}$ in the gas phase, the critical coverage was discovered when the 80th H atom adsorbed on the last available empty Ni_3 hollow site, which caused ΔG_{diff} to become positive. The structure of the critical hydrogen coverage

exhibited high symmetry and four hydrogen atoms were adsorbed on each facet. Hydrogen atoms occupied all Ni_3 hollow and Pt top sites, whereas only 4 out of 5 Pt-Ni bridge sites around each Pt atom were occupied. For $Pt_{12}Ni_{43}$ on the support, the critical coverage was discovered to be 71 H atoms. This corresponds to 3.74 H atoms per facet, which is slightly less compared to the gas phase, because one cluster facet was unavailable for hydrogen adsorption. The support was observed to have no significant effect on the preferred adsorption sites or the structure of the hydrogen coverage.

Below the critical coverages, the hydrogen adsorption results for all studied systems were coherent. Sampling was done for $n_H = 73$–79 adsorbed H atoms in the gas phase and for $n_H = 66$–70 on the support. Empty Pt top sites and Ni_3 hollow sites were favorable for hydrogen adsorption. The adsorption on Pt top sites did not affect the positions of the other H atoms, whereas the adsorption on a Ni_3 hollow site slightly changed the configuration of nearby H atoms.

Above the critical coverage, the endergonic adsorption of an additional H atom on the $Pt_{12}Ni_{43}$ and $Pt_{20}Ni_{35}$ gas phase clusters was observed to form an H_2 molecule, which preferred to adsorb on a Pt top site (Pt-H_2 complex). Similar formation of an H_2 molecule on a top site was observed by Wexler *et al.* [24], who reported a Ni-H_2 complex to form, when the critical coverage was reached on the Ni_5P_4 surface. In the present work, the reaching of critical coverage and the formation of a Pt-H_2 complex caused considerable jumps (0.12–0.22 eV) in ΔG_{diff} for all systems.

The high hydrogen coverages caused the clusters to expand, but they retained their icosahedral shape. For example, the diameter of the $Pt_{12}Ni_{43}$ cluster increased by 0.42 Å, from 9.68 Å (without H) to 10.10 Å (with 80 H), while the maximum diameter of the hydrogen coverage was 13.25 Å. On the alumina support, the high hydrogen coverage caused the $Pt_{12}Ni_{43}$ cluster to shift approximately 0.07 Å away from the surface. According to Bader charge analysis, the 80 H atoms adsorbed on $Pt_{12}Ni_{43}$ carried a charge of $+0.10e$ per atom, whereas both Ni and Pt atoms accumulated charge from the hydrogen coverage. The Coulomb repulsion between the positively charged H atoms had a effect on the structure of the coverage.

The free energies of hydrogen adsorption, ΔG_{H^*}, obtained for the $Pt_{12}Ni_{43}$ and $Pt_{20}Ni_{35}$ clusters in the gas phase are -0.10 eV and -0.03 eV, respectively. ΔG_{H^*} for $Pt_{12}Ni_{43}$ on the alumina support was approximately thermoneutral, 0.00 eV. All obtained ΔG_{H^*} descriptor values are close to zero, which indicates that both clusters exhibit activity towards HER. This is based on the assumption that the closer ΔG_{H^*} is to zero, the better the HER activity. Likewise for Pt(111), ΔG_{H^*}

has been reported to be between zero and −0.1 eV [43, 44]. The obtained values suggest that the support has a considerable effect on ΔG_{H^*} for $Pt_{12}Ni_{43}$, because it improves from −0.10 eV in the gas phase to being approximately thermoneutral on the support. This is beneficial, because in experiments and practical applications nanoparticles are deposited on a support. However, the errors due to approximations are of the same order and therefore the obtained ΔG_{H^*} are debatable. It is difficult to say if $Pt_{20}Ni_{35}$ is more promising HER catalyst than $Pt_{12}Ni_{43}$, even though its ΔG_{H^*} is smaller.

In conclusion, the critical hydrogen coverages were successfully found for two Pt-Ni compositions, $Pt_{12}Ni_{43}$ and $Pt_{20}Ni_{35}$, in the gas phase and for $Pt_{12}Ni_{43}$ on the alumina support. The values of the ΔG_{H^*} descriptor were evaluated and the results suggest that the small Pt-Ni nanoclusters exhibit activity towards HER. The icosahedral 55-atom clusters were rather difficult to model due to their high surface area, which resulted in a large number of different possible hydrogen adsorption sites. Several assumptions had to be made when the hydrogen coverages were sampled to reduce the degrees of freedom, which contains a possibility for error. Density functional theory also introduces some error to the calculated adsorption energies. Another error source may be the 0.24 eV correction to the entropy and zero point energy terms, which was not calculated explicitly for the clusters, but taken from the literature.

The present study suggests that small Pt-Ni alloy nanoclusters could be efficient HER catalysts. Their advantage is that they would require less platinum than pure Pt NPs, which would result in cheaper catalysts. In the future, it would be interesting to obtain experimental insight on small Pt-Ni nanoclusters as HER catalysts to see if they are active towards HER as indicated by the computational results. In the computational perspective, it would be interesting to study the hydrogen adsorption on the $Pt_{20}Ni_{35}$ cluster on the alumina support and to repeat the study for different Pt-TM systems. Because the critical coverages are high, the computational cost could be reduced by sampling only high coverages near the estimated critical coverage. If different Pt-TM systems were discovered to follow similar adsorption trends regardless of composition, the search for critical coverages and descriptor values could be highly automated. The ultimate goal would be to remove platinum completely and to find hydrogen evolving nanoclusters consisting only of non-critical transition metals.

BIBLIOGRAPHY

[1] United Nations, Department of Economic and Social Affairs, Population Division, "World population 2017," 2017. Available online: `https://esa.un.org/unpd/wpp/Publications/Files/WPP2017_Wallchart.pdf`. Accessed February 1, 2018.

[2] International Energy Agency, "Key world energy statistics (2017)," 2017. Available online: `https://www.iea.org/publications/freepublications/publication/key-world-energy-statistics.html`. Accessed February 1, 2018.

[3] Z. W. Seh, J. Kibsgaard, C. F. Dickens, I. Chorkendorff, J. K. Nørskov, and T. F. Jaramillo, "Combining theory and experiment in electrocatalysis: Insights into materials design," *Science*, vol. 355, no. 6321, p. eaad4998, 2017.

[4] P. C. Vesborg, B. Seger, and I. Chorkendorff, "Recent development in hydrogen evolution reaction catalysts and their practical implementation," *The Journal of Physical Chemistry Letters*, vol. 6, no. 6, pp. 951–957, 2015.

[5] I. E. Stephens and I. Chorkendorff, "Minimizing the use of platinum in hydrogen-evolving electrodes," *Angewandte Chemie International Edition*, vol. 50, no. 7, pp. 1476–1477, 2011.

[6] I. E. L. Stephens, J. Rossmeisl, and I. Chorkendorff, "Toward sustainable fuel cells," *Science*, vol. 354, no. 6318, pp. 1378–1379, 2016.

[7] J. D. Benck, T. R. Hellstern, J. Kibsgaard, P. Chakthranont, and T. F. Jaramillo, "Catalyzing the hydrogen evolution reaction (HER) with molybdenum sulfide nanomaterials," *ACS Catalysis*, vol. 4, no. 11, pp. 3957–3971, 2014.

[8] N. Danilovic, R. Subbaraman, D. Strmcnik, V. R. Stamenkovic, and N. M. Markovic, "Electrocatalysis of the HER in acid and alkaline media.," *Journal of the Serbian Chemical Society*, vol. 78, no. 12, 2013.

[9] M. E. Björketun, A. S. Bondarenko, B. L. Abrams, I. Chorkendorff, and J. Rossmeisl, "Screening of electrocatalytic materials for hydrogen evolution," *Physical Chemistry Chemical Physics*, vol. 12, no. 35, pp. 10536–10541, 2010.

[10] U.S. Geological Survey, Platinum-Group Metals Statistics and Information, "Platinum-group metals (2014)," 2014. Available online: `https://minerals.`

usgs.gov/minerals/pubs/commodity/platinum/mcs-2015-plati.pdf. Accessed February 3, 2018.

[11] European Commission, Ad-hoc Working Group of Raw Materials Supply Group, "Critical raw materials for the EU," 2010. Available online: http://www.catalysiscluster.eu/wp/wp-content/uploads/2015/05/2014_Critical-raw-materials-for-the-EU-2014.pdf. Accessed February 23, 2018.

[12] D. Guedes-Sobrinho, R. K. Nomiyama, A. S. Chaves, M. J. Piotrowski, and J. L. Da Silva, "Structure, electronic, and magnetic properties of binary Pt_nTM_{55-n} (TM = Fe, Co, Ni, Cu, Zn) nanoclusters: A density functional theory investigation," *The Journal of Physical Chemistry C*, vol. 119, no. 27, pp. 15669–15679, 2015.

[13] V. R. Stamenkovic, B. S. Mun, K. J. Mayrhofer, P. N. Ross, and N. M. Markovic, "Effect of surface composition on electronic structure, stability, and electrocatalytic properties of Pt-transition metal alloys: Pt-skin versus Pt-skeleton surfaces," *Journal of the American Chemical Society*, vol. 128, no. 27, pp. 8813–8819, 2006.

[14] V. R. Stamenkovic, B. Fowler, B. S. Mun, G. Wang, P. N. Ross, C. A. Lucas, and N. M. Marković, "Improved oxygen reduction activity on $Pt_3Ni(111)$ via increased surface site availability," *Science*, vol. 315, no. 5811, pp. 493–497, 2007.

[15] B. Hammer and J. K. Nørskov, "Theoretical surface science and catalysis–calculations and concepts," in *Advances in Catalysis*, vol. 45, pp. 71–129, Elsevier, 2000.

[16] J. Kitchin, J. K. Nørskov, M. Barteau, and J. Chen, "Modification of the surface electronic and chemical properties of Pt(111) by subsurface 3d transition metals," *The Journal of Chemical Physics*, vol. 120, no. 21, pp. 10240–10246, 2004.

[17] F. Yang, D. Deng, X. Pan, Q. Fu, and X. Bao, "Understanding nano effects in catalysis," *National Science Review*, vol. 2, no. 2, pp. 183–201, 2015.

[18] CP2K: Open Source Molecular Dynamics, https://www.cp2k.org. Accessed February 8, 2018.

[19] A. J. Bard and L. R. Faulkner, *Electrochemical Methods: Fundamentals and Applications*, John Wiley & Sons: New York, 2nd Ed., 2001, 864 p.

[20] J. L. Bonde, *New Materials for Hydrogen Evolution*, PhD Thesis, Technical University of Denmark, 2008.

[21] I. Chorkendorff and J. W. Niemantsverdriet, *Concepts of Modern Catalysis and Kinetics*, John Wiley & Sons, 2nd Ed., 2007, 477 p.

[22] B. R. Goldsmith, "Introduction to first-principles modeling of catalysis at surfaces," lecture slides, Fritz-Haber-Institut der Max-Planck-Gesellschaft, Theory Department. Available online: `http://cheresearch.engin.umich.edu/goldsmith/images/IMPRS_introduction_to_modeling_of_catalysis_at_surfaces.pdf`. Accessed February 4, 2018.

[23] J. K. Nørskov, T. Bligaard, J. Rossmeisl, and C. H. Christensen, "Towards the computational design of solid catalysts," *Nature Chemistry*, vol. 1, no. 1, p. 37, 2009.

[24] R. B. Wexler, J. M. P. Martirez, and A. M. Rappe, "Active role of phosphorus in the hydrogen evolving activity of nickel phosphide (0001) surfaces," *ACS Catalysis*, vol. 7, no. 11, pp. 7718–7725, 2017.

[25] Reference Hydrogen Electrodes, `https://www.referenceelectrode.info`. Accessed February 10, 2018.

[26] J. Tafel, "Über die Polarisation bei kathodischer Wasserstoffentwicklung," *Zeitschrift für Physikalische Chemie*, vol. 50, no. 1, pp. 641–712, 1905.

[27] D. Strmcnik, P. P. Lopes, B. Genorio, V. R. Stamenkovic, and N. M. Markovic, "Design principles for hydrogen evolution reaction catalyst materials," *Nano Energy*, vol. 29, pp. 29–36, 2016.

[28] B. Hinnemann, P. G. Moses, J. Bonde, K. P. Jørgensen, J. H. Nielsen, S. Horch, I. Chorkendorff, and J. K. Nørskov, "Biomimetic hydrogen evolution: MoS_2 nanoparticles as catalyst for hydrogen evolution," *Journal of the American Chemical Society*, vol. 127, no. 15, pp. 5308–5309, 2005.

[29] J. K. Nørskov, T. Bligaard, A. Logadottir, J. Kitchin, J. G. Chen, S. Pandelov, and U. Stimming, "Trends in the exchange current for hydrogen evolution," *Journal of the Electrochemical Society*, vol. 152, no. 3, pp. J23–J26, 2005.

[30] Y. Li, H. Wang, L. Xie, Y. Liang, G. Hong, and H. Dai, "MoS_2 nanoparticles grown on graphene: an advanced catalyst for the hydrogen evolution reaction," *Journal of the American Chemical Society*, vol. 133, no. 19, pp. 7296–7299, 2011.

[31] B. Conway and B. Tilak, "Interfacial processes involving electrocatalytic evolution and oxidation of H_2, and the role of chemisorbed H," *Electrochimica Acta*, vol. 47, no. 22-23, pp. 3571–3594, 2002.

[32] W.-F. Chen, C.-H. Wang, K. Sasaki, N. Marinkovic, W. Xu, J. T. Muckerman, Y. Zhu, and R. R. Adzic, "Highly active and durable nanostructured molybdenum carbide electrocatalysts for hydrogen production," *Energy & Environmental Science*, vol. 6, no. 3, pp. 943–951, 2013.

[33] E. J. Popczun, C. G. Read, C. W. Roske, N. S. Lewis, and R. E. Schaak, "Highly active electrocatalysis of the hydrogen evolution reaction by cobalt phosphide nanoparticles," *Angewandte Chemie*, vol. 126, no. 21, pp. 5531–5534, 2014.

[34] E. J. Popczun, J. R. McKone, C. G. Read, A. J. Biacchi, A. M. Wiltrout, N. S. Lewis, and R. E. Schaak, "Nanostructured nickel phosphide as an electrocatalyst for the hydrogen evolution reaction," *Journal of the American Chemical Society*, vol. 135, no. 25, pp. 9267–9270, 2013.

[35] A. Laursen, K. Patraju, M. Whitaker, M. Retuerto, T. Sarkar, N. Yao, K. Ramanujachary, M. Greenblatt, and G. Dismukes, "Nanocrystalline Ni_5P_4: a hydrogen evolution electrocatalyst of exceptional efficiency in both alkaline and acidic media," *Energy & Environmental Science*, vol. 8, no. 3, pp. 1027–1034, 2015.

[36] D. Kong, H. Wang, Z. Lu, and Y. Cui, "$CoSe_2$ nanoparticles grown on carbon fiber paper: an efficient and stable electrocatalyst for hydrogen evolution reaction," *Journal of the American Chemical Society*, vol. 136, no. 13, pp. 4897–4900, 2014.

[37] W.-F. Chen, K. Sasaki, C. Ma, A. I. Frenkel, N. Marinkovic, J. T. Muckerman, Y. Zhu, and R. R. Adzic, "Hydrogen-evolution catalysts based on non-noble metal nickel–molybdenum nitride nanosheets," *Angewandte Chemie International Edition*, vol. 51, no. 25, pp. 6131–6135, 2012.

[38] A. S. Bandarenka, E. Ventosa, A. Maljusch, J. Masa, and W. Schuhmann, "Techniques and methodologies in modern electrocatalysis: evaluation of activity, selectivity and stability of catalytic materials," *Analyst*, vol. 139, no. 6, pp. 1274–1291, 2014.

[39] M. Boudart, "Turnover rates in heterogeneous catalysis," *Chemical Reviews*, vol. 95, no. 3, pp. 661–666, 1995.

[40] Z. Chen, D. Cummins, B. N. Reinecke, E. Clark, M. K. Sunkara, and T. F. Jaramillo, "Core–shell MoO_3–MoS_2 nanowires for hydrogen evolution: a functional design for electrocatalytic materials," *Nano Letters*, vol. 11, no. 10, pp. 4168–4175, 2011.

[41] R. Parsons, "The rate of electrolytic hydrogen evolution and the heat of adsorption of hydrogen," *Transactions of the Faraday Society*, vol. 54, pp. 1053–1063, 1958.

[42] J. Greeley, T. F. Jaramillo, J. Bonde, I. Chorkendorff, and J. K. Nørskov, "Computational high-throughput screening of electrocatalytic materials for hydrogen evolution," *Nature Materials*, vol. 5, no. 11, p. 909, 2006.

[43] T. F. Jaramillo, K. P. Jørgensen, J. Bonde, J. H. Nielsen, S. Horch, and I. Chorkendorff, "Identification of active edge sites for electrochemical H_2 evolution from MoS_2 nanocatalysts," *Science*, vol. 317, no. 5834, pp. 100–102, 2007.

[44] E. Skúlason, V. Tripkovic, M. E. Björketun, S. Gudmundsdóttir, G. Karlberg, J. Rossmeisl, T. Bligaard, H. Jónsson, and J. K. Nørskov, "Modeling the electrochemical hydrogen oxidation and evolution reactions on the basis of density functional theory calculations," *The Journal of Physical Chemistry C*, vol. 114, no. 42, pp. 18182–18197, 2010.

[45] T. R. Hellstern, J. D. Benck, J. Kibsgaard, C. Hahn, and T. F. Jaramillo, "Engineering cobalt phosphide (CoP) thin film catalysts for enhanced hydrogen evolution activity on silicon photocathodes," *Advanced Energy Materials*, vol. 6, no. 4, p. 1501758, 2016.

[46] J. Kibsgaard and T. F. Jaramillo, "Molybdenum phosphosulfide: An active, acid-stable, earth-abundant catalyst for the hydrogen evolution reaction," *Angewandte Chemie International Edition*, vol. 53, no. 52, pp. 14433–14437, 2014.

[47] J. Kibsgaard, C. Tsai, K. Chan, J. D. Benck, J. K. Nørskov, F. Abild-Pedersen, and T. F. Jaramillo, "Designing an improved transition metal phosphide catalyst for hydrogen evolution using experimental and theoretical trends," *Energy & Environmental Science*, vol. 8, no. 10, pp. 3022–3029, 2015.

[48] W. A. Hoffert, J. A. S. Roberts, R. M. Bullock, and M. L. Helm, "Production of H_2 at fast rates using a nickel electrocatalyst in water–acetonitrile solutions," *Chemical Communications*, vol. 49, no. 71, pp. 7767–7769, 2013.

[49] J. Hou, M. Fang, A. J. P. Cardenas, W. J. Shaw, M. L. Helm, R. M. Bullock, J. A. S. Roberts, and M. O'Hagan, "Electrocatalytic H_2 production with a turnover frequency $>10^7$ s^{-1}: the medium provides an increase in rate but not overpotential," *Energy & Environmental Science*, vol. 7, no. 12, pp. 4013–4017, 2014.

[50] H. J. S. Brown, S. Wiese, J. A. S. Roberts, R. M. Bullock, and M. L. Helm, "Electrocatalytic hydrogen production by $[Ni(7P^{Ph}{}_2N^H)_2]^{2+}$: Removing the distinction between endo- and exo-protonation sites," *ACS Catalysis*, vol. 5, no. 4, pp. 2116–2123, 2015.

[51] J. Tian, Q. Liu, A. M. Asiri, and X. Sun, "Self-supported nanoporous cobalt phosphide nanowire arrays: an efficient 3D hydrogen-evolving cathode over the wide range of pH 0–14," *Journal of the American Chemical Society*, vol. 136, no. 21, pp. 7587–7590, 2014.

[52] Q. Liu, J. Tian, W. Cui, P. Jiang, N. Cheng, A. M. Asiri, and X. Sun, "Carbon nanotubes decorated with CoP nanocrystals: A highly active non-noble-metal nanohybrid electrocatalyst for hydrogen evolution," *Angewandte Chemie*, vol. 126, no. 26, pp. 6828–6832, 2014.

[53] J. Hao, W. Yang, Z. Zhang, and J. Tang, "Metal–organic frameworks derived $Co_xFe_{1-x}P$ nanocubes for electrochemical hydrogen evolution," *Nanoscale*, vol. 7, no. 25, pp. 11055–11062, 2015.

[54] J. M. McEnaney, J. C. Crompton, J. F. Callejas, E. J. Popczun, A. J. Biacchi, N. S. Lewis, and R. E. Schaak, "Amorphous molybdenum phosphide nanoparticles for electrocatalytic hydrogen evolution," *Chemistry of Materials*, vol. 26, no. 16, pp. 4826–4831, 2014.

[55] J. F. Callejas, J. M. McEnaney, C. G. Read, J. C. Crompton, A. J. Biacchi, E. J. Popczun, T. R. Gordon, N. S. Lewis, and R. E. Schaak, "Electrocatalytic and photocatalytic hydrogen production from acidic and neutral-pH aqueous solutions using iron phosphide nanoparticles," *ACS Nano*, vol. 8, no. 11, pp. 11101–11107, 2014.

[56] H. Vrubel and X. Hu, "Molybdenum boride and carbide catalyze hydrogen evolution in both acidic and basic solutions," *Angewandte Chemie*, vol. 124, no. 51, pp. 12875–12878, 2012.

[57] C. Tsai, K. Chan, J. K. Nørskov, and F. Abild-Pedersen, "Theoretical insights into the hydrogen evolution activity of layered transition metal dichalcogenides," *Surface Science*, vol. 640, pp. 133–140, 2015.

[58] J. Kibsgaard, Z. Chen, B. N. Reinecke, and T. F. Jaramillo, "Engineering the surface structure of MoS_2 to preferentially expose active edge sites for electrocatalysis," *Nature Materials*, vol. 11, no. 11, p. 963, 2012.

[59] D. Kong, H. Wang, J. J. Cha, M. Pasta, K. J. Koski, J. Yao, and Y. Cui, "Synthesis of MoS_2 and $MoSe_2$ films with vertically aligned layers," *Nano Letters*, vol. 13, no. 3, pp. 1341–1347, 2013.

[60] R. Kronberg, M. Hakala, N. Holmberg, and K. Laasonen, "Hydrogen adsorption on MoS_2-surfaces: a DFT study on preferential sites and the effect of sulfur and hydrogen coverage," *Physical Chemistry Chemical Physics*, vol. 19, no. 24, pp. 16231–16241, 2017.

[61] J. Bonde, P. G. Moses, T. F. Jaramillo, J. K. Nørskov, and I. Chorkendorff, "Hydrogen evolution on nano-particulate transition metal sulfides," *Faraday Discussions*, vol. 140, pp. 219–231, 2009.

[62] D. Merki, H. Vrubel, L. Rovelli, S. Fierro, and X. Hu, "Fe, Co, and Ni ions promote the catalytic activity of amorphous molybdenum sulfide films for hydrogen evolution," *Chemical Science*, vol. 3, no. 8, pp. 2515–2525, 2012.

[63] H. Wang, D. Kong, P. Johanes, J. J. Cha, G. Zheng, K. Yan, N. Liu, and Y. Cui, "$MoSe_2$ and WSe_2 nanofilms with vertically aligned molecular layers on curved and rough surfaces," *Nano Letters*, vol. 13, no. 7, pp. 3426–3433, 2013.

[64] D. Wang, X. Zhang, Y. Shen, and Z. Wu, "Ni-doped MoS_2 nanoparticles as highly active hydrogen evolution electrocatalysts," *RSC Advances*, vol. 6, no. 20, pp. 16656–16661, 2016.

[65] Y. Ouyang, C. Ling, Q. Chen, Z. Wang, L. Shi, and J. Wang, "Activating inert basal planes of MoS_2 for hydrogen evolution reaction through the formation of different intrinsic defects," *Chemistry of Materials*, vol. 28, no. 12, pp. 4390–4396, 2016.

[66] H. Li, C. Tsai, A. L. Koh, L. Cai, A. W. Contryman, A. H. Fragapane, J. Zhao, H. S. Han, H. C. Manoharan, F. Abild-Pedersen, *et al.*, "Activating and optimizing MoS_2 basal planes for hydrogen evolution through the formation of strained sulphur vacancies," *Nature Materials*, vol. 15, no. 1, p. 48, 2016.

[67] P. Liu and J. A. Rodriguez, "Catalysts for hydrogen evolution from the [NiFe] hydrogenase to the $Ni_2P(001)$ surface: the importance of ensemble effect," *Journal of the American Chemical Society*, vol. 127, no. 42, pp. 14871–14878, 2005.

[68] L. Feng, H. Vrubel, M. Bensimon, and X. Hu, "Easily-prepared dinickel phosphide (Ni_2P) nanoparticles as an efficient and robust electrocatalyst for hydrogen evolution," *Physical Chemistry Chemical Physics*, vol. 16, no. 13, pp. 5917–5921, 2014.

[69] J. M. McEnaney, J. C. Crompton, J. F. Callejas, E. J. Popczun, C. G. Read, N. S. Lewis, and R. E. Schaak, "Electrocatalytic hydrogen evolution using amorphous tungsten phosphide nanoparticles," *Chemical Communications*, vol. 50, no. 75, pp. 11026–11028, 2014.

[70] P. Xiao, M. A. Sk, L. Thia, X. Ge, R. J. Lim, J.-Y. Wang, K. H. Lim, and X. Wang, "Molybdenum phosphide as an efficient electrocatalyst for the hydrogen evolution reaction," *Energy & Environmental Science*, vol. 7, no. 8, pp. 2624–2629, 2014.

[71] Z. Xing, Q. Liu, A. M. Asiri, and X. Sun, "Closely interconnected network of molybdenum phosphide nanoparticles: a highly efficient electrocatalyst for generating hydrogen from water," *Advanced Materials*, vol. 26, no. 32, pp. 5702–5707, 2014.

[72] Z. W. Seh, K. D. Fredrickson, B. Anasori, J. Kibsgaard, A. L. Strickler, M. R. Lukatskaya, Y. Gogotsi, T. F. Jaramillo, and A. Vojvodic, "Two-dimensional molybdenum carbide (MXene) as an efficient electrocatalyst for hydrogen evolution," *ACS Energy Letters*, vol. 1, no. 3, pp. 589–594, 2016.

[73] F. H. Saadi, A. I. Carim, J. M. Velazquez, J. H. Baricuatro, C. C. McCrory, M. P. Soriaga, and N. S. Lewis, "Operando synthesis of macroporous molybdenum diselenide films for electrocatalysis of the hydrogen-evolution reaction," *ACS Catalysis*, vol. 4, no. 9, pp. 2866–2873, 2014.

[74] M. S. Faber, R. Dziedzic, M. A. Lukowski, N. S. Kaiser, Q. Ding, and S. Jin, "High-performance electrocatalysis using metallic cobalt pyrite (CoS_2) micro- and nanostructures," *Journal of the American Chemical Society*, vol. 136, no. 28, pp. 10053–10061, 2014.

[75] Y. Chen, G. Yu, W. Chen, Y. Liu, G.-D. Li, P. Zhu, Q. Tao, Q. Li, J. Liu, X. Shen, *et al.*, "Highly active, nonprecious electrocatalyst comprising borophene subunits for the hydrogen evolution reaction," *Journal of the American Chemical Society*, vol. 139, no. 36, pp. 12370–12373, 2017.

[76] J. R. McKone, B. F. Sadtler, C. A. Werlang, N. S. Lewis, and H. B. Gray, "Ni–Mo nanopowders for efficient electrochemical hydrogen evolution," *ACS Catalysis*, vol. 3, no. 2, pp. 166–169, 2013.

[77] C. C. McCrory, S. Jung, I. M. Ferrer, S. M. Chatman, J. C. Peters, and T. F. Jaramillo, "Benchmarking hydrogen evolving reaction and oxygen evolving reaction electrocatalysts for solar water splitting devices," *Journal of the American Chemical Society*, vol. 137, no. 13, pp. 4347–4357, 2015.

[78] I. A. Raj and K. Vasu, "Transition metal-based hydrogen electrodes in alkaline solution–electrocatalysis on nickel based binary alloy coatings," *Journal of Applied Electrochemistry*, vol. 20, no. 1, pp. 32–38, 1990.

[79] K. Reuter, C. P. Plaisance, H. Oberhofer, and M. Andersen, "Perspective: On the active site model in computational catalyst screening," *The Journal of Chemical Physics*, vol. 146, no. 4, p. 040901, 2017.

[80] C. H. Christensen and J. K. Nørskov, "A molecular view of heterogeneous catalysis," *The Journal of Chemical Physics*, vol. 128, no. 18, p. 182503, 2008.

[81] J. Greeley, "Theoretical heterogeneous catalysis: scaling relationships and computational catalyst design," *Annual Review of Chemical and Biomolecular Engineering*, vol. 7, pp. 605–635, 2016.

[82] E. A. Pidko, "Toward the balance between the reductionist and systems approaches in computational catalysis: Model versus method accuracy for the description of catalytic systems," *ACS Catalysis*, vol. 7, pp. 4230–4234, 2017.

[83] A. J. Medford, A. Vojvodic, J. S. Hummelshøj, J. Voss, F. Abild-Pedersen, F. Studt, T. Bligaard, A. Nilsson, and J. K. Nørskov, "From the sabatier principle to a predictive theory of transition-metal heterogeneous catalysis," *Journal of Catalysis*, vol. 328, pp. 36–42, 2015.

[84] E. Skúlason, G. S. Karlberg, J. Rossmeisl, T. Bligaard, J. Greeley, H. Jónsson, and J. K. Nørskov, "Density functional theory calculations for the hydrogen evolution reaction in an electrochemical double layer on the Pt(111) electrode," *Physical Chemistry Chemical Physics*, vol. 9, no. 25, pp. 3241–3250, 2007.

[85] Q. Tang and De-en Jiang, "Mechanism of hydrogen evolution reaction on 1T-MoS_2 from first principles," *ACS Catalysis*, vol. 6, no. 8, pp. 4953–4961, 2016.

[86] M. H. Hansen, L.-A. Stern, L. Feng, J. Rossmeisl, and X. Hu, "Widely available active sites on Ni_2P for electrochemical hydrogen evolution–insights from first principles calculations," *Physical Chemistry Chemical Physics*, vol. 17, no. 16, pp. 10823–10829, 2015.

[87] Z. Wang and P. Hu, "Towards rational catalyst design: a general optimization framework," *Philosophical Transactions of the Royal Society A*, vol. 374, no. 2061, p. 20150078, 2016.

[88] K. Reuter, "Ab initio thermodynamics and first-principles microkinetics for surface catalysis," *Catalysis Letters*, vol. 146, no. 3, pp. 541–563, 2016.

[89] L. Kristinsdóttir and E. Skúlason, "A systematic DFT study of hydrogen diffusion on transition metal surfaces," *Surface Science*, vol. 606, no. 17-18, pp. 1400–1404, 2012.

[90] E. Schrödinger, "An undulatory theory of the mechanics of atoms and molecules," *Physical Review*, vol. 28, no. 6, p. 1049, 1926.

[91] J. Kohanoff, *Electronic Structure Calculations for Solids and Molecules: Theory and Computational Methods*, Cambridge University Press, 2006, 372 p.

[92] J. Q. Goh, *Density Functional Studies of Superatomic Ligand-Protected Nanoclusters*, PhD Thesis, Tampere University of Technology, 2016.

[93] M. Born and R. Oppenheimer, "On the quantum theory of molecules," *Annalen der Physik*, vol. 84, no. 4, pp. 457–484, 1927.

[94] P. W. Atkins and R. S. Friedman, *Molecular Quantum Mechanics*, Oxford University Press, 5th Ed., 2011, 592 p.

[95] R. P. Feynman, "Forces in molecules," *Physical Review*, vol. 56, no. 4, p. 340, 1939.

[96] A. R. Leach, *Molecular Modelling: Principles and Applications*, Pearson Education, 2nd Ed., 2001, 784 p.

[97] J. C. Slater, "The theory of complex spectra," *Physical Review*, vol. 34, no. 10, p. 1293, 1929.

[98] P. Hohenberg and W. Kohn, "Inhomogeneous electron gas," *Physical Review*, vol. 136, no. 3B, p. B864, 1964.

[99] W. Kohn and L. J. Sham, "Self-consistent equations including exchange and correlation effects," *Physical Review*, vol. 140, no. 4A, p. A1133, 1965.

[100] J. P. Perdew and K. Schmidt, "Jacob's ladder of density functional approximations for the exchange-correlation energy," in *AIP Conference Proceedings*, vol. 577, pp. 1–20, AIP, 2001.

[101] J. P. Perdew, "Climbing the ladder of density functional approximations," *MRS Bulletin*, vol. 38, no. 9, pp. 743–750, 2013.

[102] A. D. Becke, "Density-functional thermochemistry. I. The effect of the exchange-only gradient correction," *The Journal of Chemical Physics*, vol. 96, no. 3, pp. 2155–2160, 1992.

[103] J. P. Perdew, K. Burke, and M. Ernzerhof, "Generalized gradient approximation made simple," *Physical Review Letters*, vol. 77, no. 18, p. 3865, 1996.

[104] J. VandeVondele, M. Krack, F. Mohamed, M. Parrinello, T. Chassaing, and J. Hutter, "Quickstep: Fast and accurate density functional calculations using a mixed Gaussian and plane waves approach," *Computer Physics Communications*, vol. 167, no. 2, pp. 103–128, 2005.

[105] S. Goedecker, M. Teter, and J. Hutter, "Separable dual-space Gaussian pseudopotentials," *Physical Review B*, vol. 54, no. 3, p. 1703, 1996.

[106] J. VandeVondele and J. Hutter, "Gaussian basis sets for accurate calculations on molecular systems in gas and condensed phases," *The Journal of Chemical Physics*, vol. 127, no. 11, p. 114105, 2007.

[107] S. Grimme, "Semiempirical GGA-type density functional constructed with a long-range dispersion correction," *Journal of Computational Chemistry*, vol. 27, no. 15, pp. 1787–1799, 2006.

[108] S. Grimme, J. Antony, S. Ehrlich, and H. Krieg, "A consistent and accurate ab initio parametrization of density functional dispersion correction (DFT-D) for the 94 elements H-Pu," *The Journal of Chemical Physics*, vol. 132, no. 15, p. 154104, 2010.

[109] S. Grimme, S. Ehrlich, and L. Goerigk, "Effect of the damping function in dispersion corrected density functional theory," *Journal of Computational Chemistry*, vol. 32, no. 7, pp. 1456–1465, 2011.

[110] CSC – It Center for Science, `https://research.csc.fi/home`. Accessed February 20, 2018.

[111] Sisu Supercomputer, `https://research.csc.fi/csc-s-servers#sisu`. Accessed February 20, 2018.

[112] H. Kari, *Kalkogenidinanopartikkelien elektronirakennelaskut ja molekyylidynamiikka*, Master's Thesis, Tampere University of Technology, 2011.

[113] M. E. Tuckerman, *Statistical Mechanics: Theory and Molecular Simulation*, Oxford University Press, 2010, 720 p.

[114] G. Henkelman, A. Arnaldsson, and H. Jónsson, "A fast and robust algorithm for Bader decomposition of charge density," *Computational Materials Science*, vol. 36, no. 3, pp. 354–360, 2006.

[115] M. Yu and D. R. Trinkle, "Accurate and efficient algorithm for Bader charge integration," *The Journal of Chemical Physics*, vol. 134, no. 6, p. 064111, 2011.

[116] Bader Charge Analysis (version 1.03), a program written by Andri Arnaldsson, Wenjie Tang, Sam Chill, Wenrui Chai, and Graeme Henkelman, The University of Texas at Austin. Available online: `http://theory.cm.utexas.edu/henkelman/code/bader/`. Accessed February 25, 2018.

[117] M. J. Piotrowski, C. G. Ungureanu, P. Tereshchuk, K. E. Batista, A. S. Chaves, D. Guedes-Sobrinho, and J. L. Da Silva, "Theoretical study of the structural, energetic, and electronic properties of 55-atom metal nanoclusters: A DFT investigation within van der Waals corrections, spin–orbit coupling, and PBE+U of 42 metal systems," *The Journal of Physical Chemistry C*, vol. 120, no. 50, pp. 28844–28856, 2016.

[118] C. Kittel, *Introduction to Solid State Physics*, John Wiley & Sons: New York, 7th Ed., 1996, 688 p.

[119] T. Rapps, R. Ahlrichs, E. Waldt, M. M. Kappes, and D. Schooss, "On the structures of 55-atom transition-metal clusters and their relationship to the crystalline bulk," *Angewandte Chemie International Edition*, vol. 52, no. 23, pp. 6102–6105, 2013.

[120] Y. H. Yao, X. Gu, M. Ji, X. G. Gong, and Ding-sheng Wang, "Structures and magnetic moments of Ni_n ($n = 10 \sim 60$) clusters," *Physics Letters A*, vol. 360, no. 4-5, pp. 629–631, 2007.

[121] W. Song, W.-C. Lu, C. Wang, and K. Ho, "Magnetic and electronic properties of the nickel clusters Ni_n ($n \leq 30$)," *Computational and Theoretical Chemistry*, vol. 978, no. 1-3, pp. 41–46, 2011.

[122] A. S. Chaves, M. J. Piotrowski, and J. L. Da Silva, "Evolution of the structural, energetic, and electronic properties of the 3d, 4d, and 5d transition-metal clusters (30 TM_n systems for $n = 2$–15): a density functional theory investigation," *Physical Chemistry Chemical Physics*, vol. 19, no. 23, pp. 15484–15502, 2017.

[123] J. L. Da Silva, H. G. Kim, M. J. Piotrowski, M. J. Prieto, and G. Tremiliosi-Filho, "Reconstruction of core and surface nanoparticles: The example of Pt_{55} and Au_{55}," *Physical Review B*, vol. 82, no. 20, p. 205424, 2010.

[124] C. Cui, L. Gan, H.-H. Li, S.-H. Yu, M. Heggen, and P. Strasser, "Octahedral PtNi nanoparticle catalysts: exceptional oxygen reduction activity by tuning the alloy particle surface composition," *Nano Letters*, vol. 12, no. 11, pp. 5885–5889, 2012.

[125] C. Xu, J. Hou, X. Pang, X. Li, M. Zhu, and B. Tang, "Nanoporous PtCo and PtNi alloy ribbons for methanol electrooxidation," *International Journal of Hydrogen Energy*, vol. 37, no. 14, pp. 10489–10498, 2012.

[126] M. Honkanen, J. Wang, M. Kärkkäinen, M. Huuhtanen, H. Jiang, K. Kallinen, R. L. Keiski, J. Akola, and M. Vippola, "Regeneration of sulfur-poisoned Pd-based catalyst for natural gas oxidation," *Journal of Catalysis*, vol. 358, pp. 253–265, 2018.

APPENDIX A. PROJECTED DENSITY OF STATES

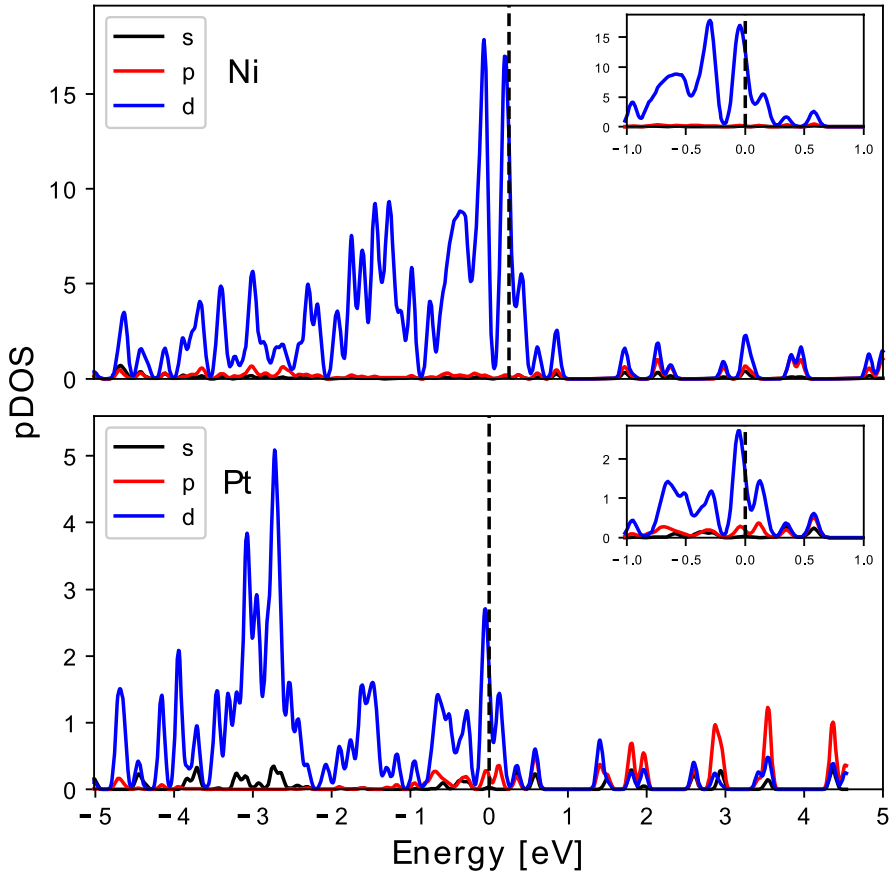

Figure A.1 *The projected density of states (PDOS) of the ground-state* $Pt_{12}Ni_{43}$ *cluster in the gas phase, shown in Figure 6.6. The PDOS values were smoothed with Gaussian functions with* $\sigma = 0.0367$ *eV. The Fermi level is set as zero and represented by the dashed line.*

APPENDIX B. RADIAL DISTRIBUTION FUNCTIONS

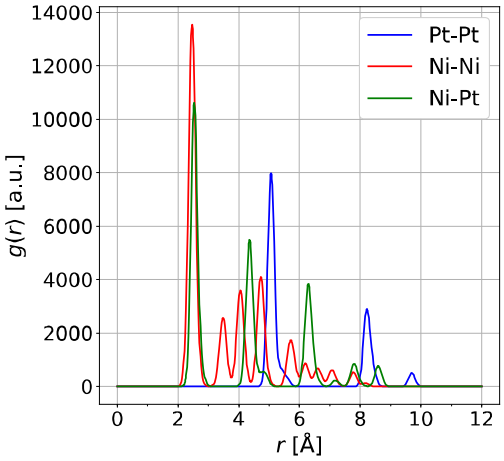

(a) $Pt_{12}Ni_{43}@Al_2O_3$

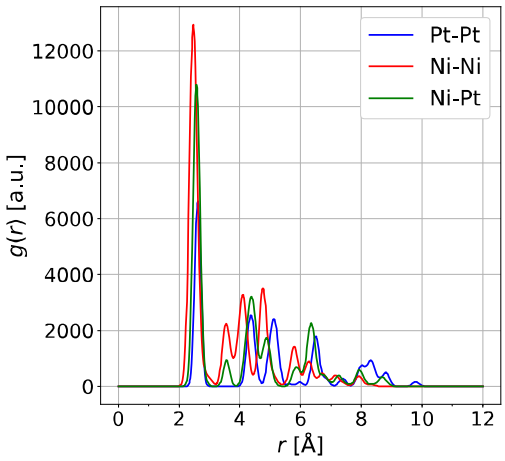

(b) $Pt_{20}Ni_{35}@Al_2O_3$

Figure B.1 *The radial distribution functions (arbitrary units) for the $Pt_{12}Ni_{43}$ and $Pt_{20}Ni_{35}$ clusters on the Al_2O_3 support. Calculated with bin size $\Delta r = 0.01$ Å and smoothed with Gaussian functions ($\sigma = 0.1$). The corresponding geometries are shown in Figures 6.11 and 6.12, respectively.*

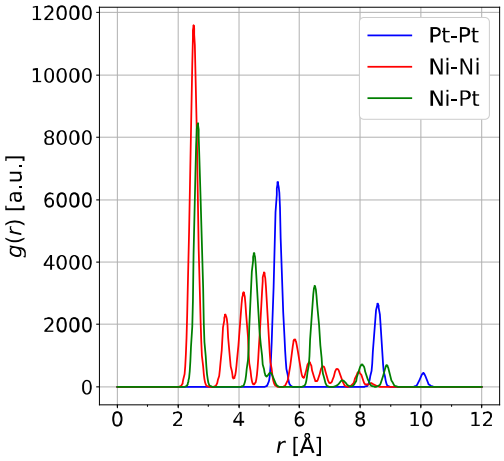

(a) Pt-Pt, Ni-Pt, and Ni-Ni atom pairs.

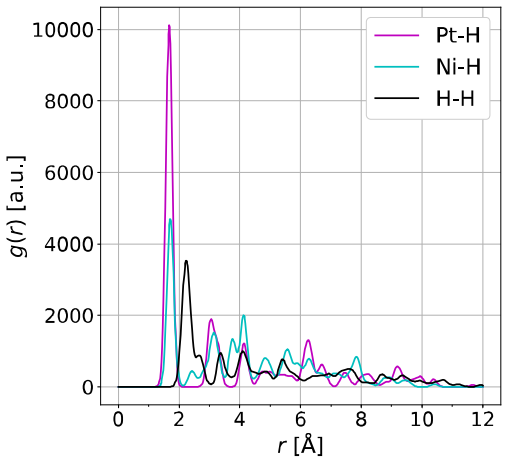

(b) Pt-H, Ni-H, and H-H atom pairs.

Figure B.2 *The radial distribution functions (arbitrary units) for the $Pt_{12}Ni_{43}$ cluster in the gas phase with the hydrogen coverage consisting of 80 H atoms (the critical coverage). Calculated with bin size $\Delta r = 0.01$ Å and smoothed with Gaussian functions ($\sigma = 0.1$). Atom pairs involving H are plotted separately. The corresponding cluster geometry is presented in Figure 7.3.*

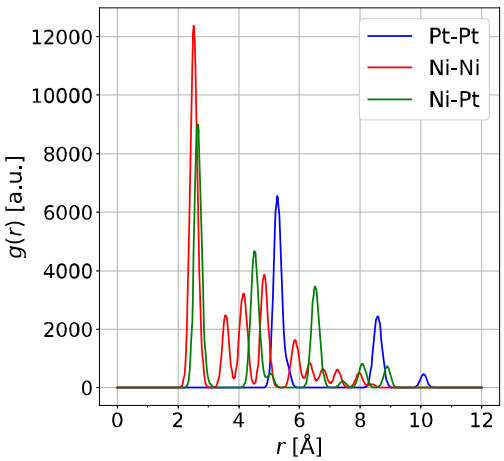

(a) Pt-Pt, Ni-Pt, and Ni-Ni atom pairs.

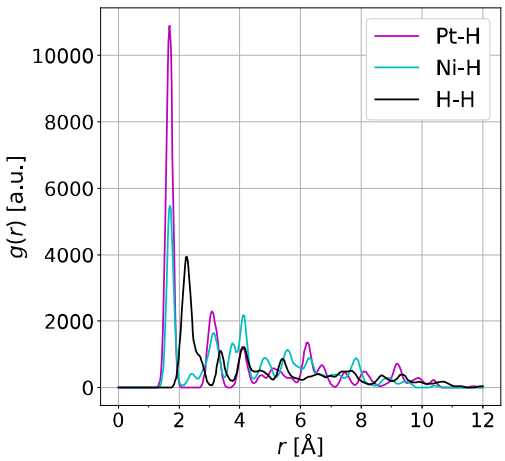

(b) Pt-H, Ni-H, and H-H atom pairs.

Figure B.3 *The radial distribution functions (arbitrary units) for the $Pt_{12}Ni_{43}$ cluster on the Al_2O_3 support with the hydrogen coverage consisting of 73 H atoms. Atom pairs involving H are plotted separately. The corresponding cluster geometry is presented in Figure 7.10.*

APPENDIX C. HYDROGEN ADSORPTION ON $PT_{20}NI_{35}$ IN THE GAS PHASE

Table C.1 *The differential Gibbs free energies of adsorption for* $n_H = 1$–7 *and* 73–81 *H atoms adsorbed on the* $Pt_{20}Ni_{35}$ *cluster in the gas phase. Calculated with Eq.* (4.9)*. Adsorption site describes the site where the last H atom is adsorbed. Odd hydrogen atoms prefer* Ni_3 *hollow sites. At even* n_H*, hydrogen atoms form pairs, which occupy bridge and Pt-*Ni_2 *hollow sites, and no H atoms are on* Ni_3 *hollow sites.*

n_H	ΔG_{diff} [eV]	Adsorption site
1	−0.45	Ni_3 hollow
2	−0.58	Pt-Pt bridge (Pt-Ni_2 hollow)
3	−0.45	Ni_3 hollow
4	−0.55	Pt-Ni bridge (Pt-Ni_2 hollow)
5	−0.47	Ni_3 hollow
6	−0.49	Pt-Ni bridge (Pt-Ni_2 hollow)
7	−0.50	Ni_3 hollow
73	−0.13	Pt top
74	−0.10	Pt top
75	−0.05	Pt top
76	−0.08	Pt top
77	−0.07	Ni_3 hollow
78	−0.04	Ni_3 hollow
79	−0.03	Ni_3 hollow
80	0.09	Ni_3 hollow (critical coverage)
81	0.30	Pt-H_2 complex

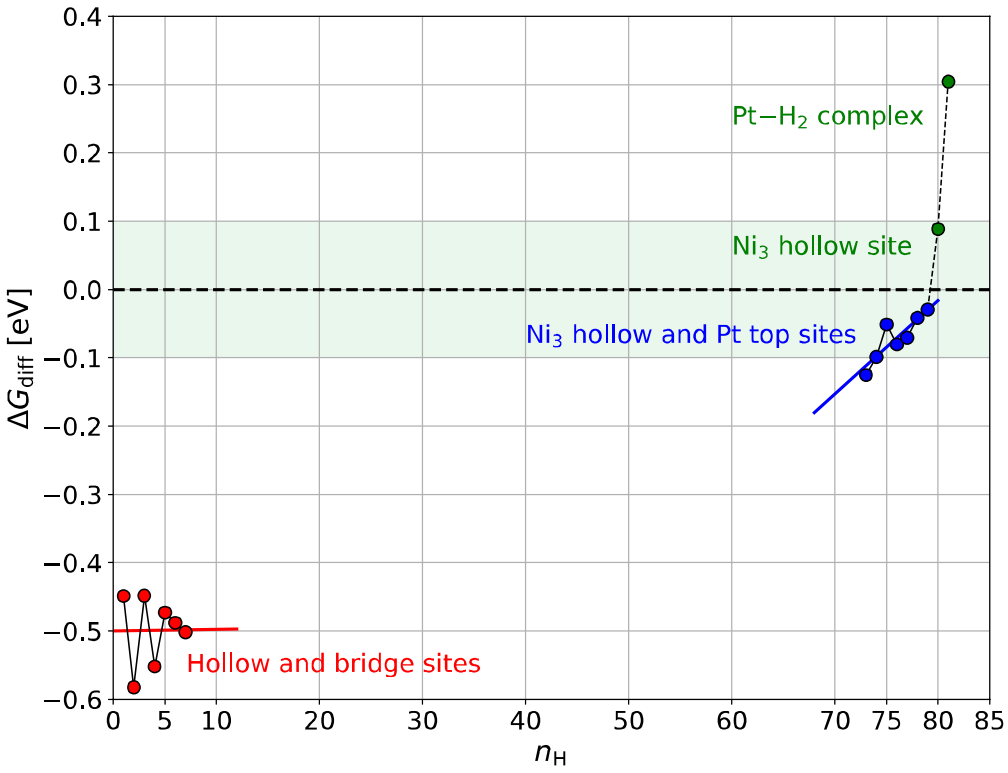

Figure C.1 *The differential Gibbs free energy of hydrogen adsorption (ΔG_{diff}) as a function of the number of H atoms (n_{H}) adsorbed on the $Pt_{20}Ni_{35}$ cluster in the gas phase. The corresponding values are values presented in C.1 for $n_{\text{H}} = 73$–81. The dotted horizontal line at $\Delta G_{\text{diff}} = 0$ corresponds to the thermoneutral H adsorption. The most optimal region in terms of catalytic activity, $|\Delta G_{\text{diff}}| < 0.1$ eV, is highlighted with the light green color. The data points are connected with the solid (dashed) lines, when the hydrogen adsorption is exergonic (endergonic). At low coverages (red region), hollow and bridge sites are favorable for H adsorption. The H atoms occupy Pt top sites at $n_{\text{H}} = 73$–76 and Ni_3 hollow sites at $n_{\text{H}} = 77$–80 (blue region). Green color represents H coverages, where ΔG_{diff} is positive. At $n_{\text{H}} = 81$, an H atom adsorbs on a Pt top site, which is already occupied by one H atom. Simple linear models were fitted to the data points at low (red) and high (blue) coverage regions.*